

**Discontinuity Preserving Image Registration
for
Breathing Induced Sliding Organ Motion**

Inauguraldissertation

zur
Erlangung der Würde eines Doktors der Philosophie
vorgelegt der
Medizinischen Fakultät
der Universität Basel

von

Silja Kiriyanthan
aus Basel

Basel, 2013

Genehmigt von der Medizinischen Fakultät
auf Antrag von

Prof. Dr. Philippe C. Cattin, Universität Basel, Fakultätsverantwortlicher
Prof. Dr. med. Elmar M. Merkle, Universität Basel, Korreferent
Prof. Dr. Anders Heyden, Lunds Universitet, externer Experte

Basel, den 29. Januar 2013

Prof. Dr. med. Christoph Beglinger
Dekan

Abstract

Image registration is a powerful tool in medical image analysis and facilitates the clinical routine in several aspects. It became an indispensable device for many medical applications including image-guided therapy systems. The basic goal of image registration is to spatially align two images that show a similar region of interest. More specifically, a displacement field respectively a transformation is estimated, that relates the positions of the pixels or feature points in one image to the corresponding positions in the other one. The so gained alignment of the images assists the doctor in comparing and diagnosing them. There exist different kinds of image registration methods, those which are capable to estimate a rigid transformation or more generally an affine transformation between the images and those which are able to capture a more complex motion by estimating a non-rigid transformation. There are many well established non-rigid registration methods, but those which are able to preserve discontinuities in the displacement field are rather rare. These discontinuities appear in particular at organ boundaries during the breathing induced organ motion.

In this thesis, we make use of the idea to combine motion segmentation with registration to tackle the problem of preserving the discontinuities in the resulting displacement field. We introduce a binary function to represent the motion segmentation and the proposed discontinuity preserving non-rigid registration method is then formulated in a variational framework. Thus, an energy functional is defined and its minimisation with respect to the displacement field and the motion segmentation will lead to the desired result. In theory, one can prove that for the motion segmentation a global minimiser of the energy functional can be found, if the displacement field is given. The overall minimisation problem, however, is non-convex and a suitable optimisation strategy has to be considered. Furthermore, depending on whether we use the pure L^1 -norm or an approximation of it in the formulation of the energy functional, we use different numerical methods to solve the minimisation problem. More specifically, when using an approximation of the L^1 -norm, the minimisation of the energy functional with respect to

the displacement field is performed through Brox *et al.*'s fixed point iteration scheme, and the minimisation with respect to the motion segmentation with the dual algorithm of Chambolle. On the other hand, when we make use of the pure L^1 -norm in the energy functional, the primal-dual algorithm of Chambolle and Pock is used for both, the minimisation with respect to the displacement field and the motion segmentation. This approach is clearly faster compared to the one using the approximation of the L^1 -norm and also theoretically more appealing. Finally, to support the registration method during the minimisation process, we incorporate additionally in a later approach the information of certain landmark positions into the formulation of the energy functional, that makes use of the pure L^1 -norm. Similarly as before, the primal-dual algorithm of Chambolle and Pock is then used for both, the minimisation with respect to the displacement field and the motion segmentation. All the proposed non-rigid discontinuity preserving registration methods delivered promising results for experiments with synthetic images and real MR images of breathing induced liver motion.

*To my beloved parents
Sunny & Marykuttu Kiriyanthan*

Acknowledgements

This thesis was written at the Medical Image Analysis Center, in the Medical Faculty of the University of Basel, Switzerland. It has been funded by a donation of Dr. Hansjörg Wyss.

First of all, I would like to thank Prof. Philippe C. Cattin for guiding and supervising me during my doctoral studies. He provided me a comfortable working atmosphere and gave me the possibility to attend several interesting scientific occasions. I would also like to thank him for his helpful suggestions and input during my doctoral studies and finally for his friendliness.

Furthermore, I would like to thank Dr. Ketut Fundana for sharing his broad scientific knowledge with me. Like this I gained a lot of interesting insight and deeper knowledge in related and relevant research topics. I also thank Dr. Ketut Fundana for his helpful advise during the last years and for providing me the unique chance to participate in the Symposium on Variational Image Analysis that took place in Heidelberg in July 2011. For this, I also thank the organisers of the symposium for accepting my registration request. This symposium was definitely one of the memorable highlights during my doctoral studies.

My thanks goes also to Prof. Elmar M. Merkle for his agreement to be the co-referee in this dissertation and for reading the thesis. In the same way, I would like to thank Prof. Anders Heyden for being the external expert in this dissertation and for reviewing the manuscript.

I would like to thank all the members of the Medical Image Analysis Center, amongst others Prof. Philippe C. Cattin, Dr. Ketut Fundana, Dr. Beat Fasel, Corinne Eymann-Baier, Dr. Patrik Arnold, Tahir Majeed, Frank Preiswerk, Simon Pezold and Adrian Schneider, for interesting discussions and memorable moments. It was a pleasure for me to work with them.

During my doctoral studies I met a lot of people who were working in related research areas. Especially with Dr. Sabrina Lang, who became a good friend to me, I could share my thoughts during the work breaks and talk about the life of a PhD student. I would like to thank her for all the

funny, encouraging and memorable moments.

Moreover, I would like to thank all my teachers without whose input I wouldn't have had the knowledge I have today and wouldn't have had the ability to accomplish this work.

Finally, I would like to thank my family and friends for their strong support and their patience. Often, I had to neglect them during my doctoral studies and I thank them all for their understanding. I would like to thank my parents for their encouragement and for always being there for me. My thanks goes also to my parents-in-law, Elbinchetta, Chechy, my sister-in-law, Jasu, my brother-in-law and my sweet little nieces Elisa and Elina for cheering me up and supporting me. Last but not least, I would like to thank my husband for his love, for his belief in me and for being there for me.

In the end and above all, I would like to thank God. Without HIM I wouldn't be at the stage in life I am right now.

Contents

1	Introduction	1
1.1	Image Registration	3
1.1.1	The Principle of Image Registration	3
1.1.2	The Right Choice of an Image Registration Method	5
1.1.3	The Validation of Image Registration Methods	7
1.2	Optical Flow	10
1.2.1	The Optical Flow Method of Brox	11
1.3	Motion Segmentation	12
1.3.1	The Mumford and Shah Segmentation Problem	13
1.3.2	The Level Set Approach of Vese and Chan	13
1.3.3	The Approach of Amiaz and Kiryati	16
1.4	Continuous Cuts Framework	17
1.4.1	Some Mathematical Definitions and Theorems	18
1.4.2	Global Minimiser	21
1.5	Optimisation	25
1.6	Landmarks	27
1.7	Outline and Contribution	28
2	Discontinuity Preserving Registration through Motion Segmentation with Continuous Cuts	31
2.1	Introduction	32
2.2	Method	33
2.2.1	Registration and Motion Segmentation Framework	33
2.2.2	Minimisation	35
2.2.3	Implementation	37
2.3	Results	38
2.4	Conclusion	40

3	A Primal-Dual Approach for Discontinuity Preserving Registration through Motion Segmentation with Continuous Cuts	43
3.1	Introduction	44
3.2	Registration and Motion Segmentation Framework	45
3.2.1	Registration	45
3.2.2	Motion Segmentation	46
3.3	Minimisation	48
3.3.1	Iterative Scheme	48
3.3.2	Basic Framework for the Primal-Dual Approach of Chambolle and Pock	49
3.4	Derivation of the Resolvent Operators	50
3.4.1	Resolvent Operators for Problem Eq. (3.10)	50
3.4.2	Resolvent Operators for Problem Eq. (3.11)	51
3.4.3	Resolvent Operators for Problem Eq. (3.12)	75
3.5	Implementation	75
3.6	Results	76
3.7	Conclusion	79
4	A Landmark-Based Primal-Dual Approach for Discontinuity Preserving Registration through Motion Segmentation with Continuous Cuts	85
4.1	Introduction	86
4.2	Method	87
4.2.1	Registration and Motion Segmentation Framework	87
4.2.2	Incorporation of the Landmarks	88
4.3	Minimisation	89
4.3.1	Iterative Scheme	89
4.3.2	The Primal-Dual Approach of Chambolle and Pock	90
4.3.3	Resolvent Operators for Problem Eq. (4.9)	91
4.3.4	Resolvent Operators for Problem Eq. (4.10)	91
4.3.5	Resolvent Operators for Problem Eq. (4.11)	93
4.4	Results	93
4.5	Conclusion	94
5	Conclusion	97

List of Figures

1.1	The movement during respiration.	2
1.2	An illustration of the principle of image registration.	4
1.3	The level set function.	14
1.4	A piecewise constant approximation.	24
1.5	A piecewise smooth approximation.	25
1.6	An illustration of the coarse-to-fine strategy.	26
1.7	A comparison of the found landmark correspondences.	30
2.1	A synthetic example.	36
2.2	A qualitative comparison.	39
2.3	A quantitative comparison.	41
3.1	The geometric interpretation.	56
3.2	The spanned space.	62
3.3	The numbering of the faces of the cube.	62
3.4	The net of the cube.	64
3.5	The labelling of the boundary values.	65
3.6	The clockwise and anti-clockwise division method.	65
3.7	The division method for situation S1.	66
3.8	The division method for situation S9.7.	68
3.9	A synthetic example.	77
3.10	The evolution of the motion segmentation function.	78
3.11	The usage of different initialisations for the motion segmentation function.	80
3.12	The effect of the weighting parameter for the TV of the motion segmentation function.	81
3.13	A qualitative comparison.	82
3.14	A quantitative comparison.	83
4.1	A qualitative comparison.	95
4.2	A quantitative comparison.	96

List of Tables

3.1	The numbering of the 27 cases.	54
3.2	The different situations for the boundary values.	67
3.3	The splitting of situation S9.	68
3.4	A comparison of the running times.	84

Chapter 1

Introduction

Image registration is an important medical image analysis tool and facilitates the clinical routine in several ways. It supports the doctors in comparing medical images of their patients and diagnosing them. Moreover, it is nowadays an indispensable part in many medical applications, as for example in image-guided therapy systems [85, 6, 68]. The task of image registration methods is to spatially align two images that show a similar region of interest by estimating a displacement field respectively a transformation that relates the positions of the pixels or feature points in one image to the corresponding positions in the other one. Once the spatial transformation has been found, one can draw conclusions about significant differences between the images and detect in a better way anomalies and pathologies.

Different classes of image registration methods exist, the ones which are able to estimate rigid or affine transformations and the more powerful ones, which are able to estimate non-rigid transformations. Whereas rigid image registration methods are satisfyingly applied to images of bones and brains, non-rigid image registration methods are crucial to estimate soft-tissue deformations between images.

There are many well established non-rigid registration methods, but those which are able to preserve discontinuities in the displacement field are very rare. Some examples of discontinuity preserving registration methods can be found for example in [73, 70]. Common non-rigid registration methods normally produce most of the registration errors at these discontinuities. Especially in the medical field the need for accurate image registration methods is obvious, since inaccurate alignments of the images can lead to crucial misinterpretations.

In the human body, discontinuities in the displacement field appear for example at organ boundaries during breathing induced organ motion. Let us consider for example the movement of the liver during respiration. A

schematic illustration is shown in Fig. 1.1. During inspiration the lung is filled with air and the diaphragm moves downwards, thus pushing the liver down. Then, during expiration the lung shrinks, the diaphragm moves upwards and the liver slides back to its initial position. Furthermore, the thoracic and abdominal wall are moving outwards and inwards during respiration. The sliding of the liver along the abdominal wall and also the perpendicular movement of the wall itself to the dominant motion during the breathing cycle clearly cause a discontinuity in the displacement field.

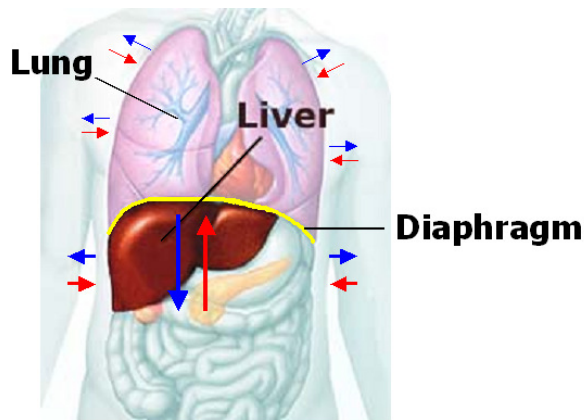


Figure 1.1: The movement of the liver, the thoracic wall and the abdominal wall during respiration. *Blue arrows*: Movement during inspiration. *Red arrows*: Movement during expiration.

A common approach to preserve the discontinuities in the displacement field, is to manually segment the objects of interest and registering them separately. The final discontinuous displacement field is then achieved, by composing the so obtained results. This semi-automatic approach is, however, very time consuming because of the need of prior manual segmentations.

A related method, is the one of Schmidt-Richberg *et al.* [73], where a direction-dependent regularisation method was proposed to preserve discontinuities in the displacement field. Their approach, however, needs prior information of the normals at the object boundaries and therefore a good manual segmentation of the objects of interest has to be provided here too in advance.

Another discontinuity preserving image registration method was proposed by Ruan *et al.* [70], where a regularisation based on the divergence and curl of the displacement field is introduced to preserve sliding motions. From their results it is, however, not clear how well this method will perform compared to other discontinuity preserving image registration methods.

The aim of this thesis is to develop a new non-rigid image registration method, that is able to preserve discontinuities in the displacement field which are caused by breathing induced organ motion. For this we combine motion segmentation with optical flow based registration in a variational framework and show how the minimisation of the resulting energy functionals can be achieved in an efficient way.

In the following, we would like to address the main topics that are important for the understanding of the proposed methods. In Section 1.1 we provide an outline of image registration. In Section 1.2 we address a related field to image registration called optical flow. Then, in Section 1.3 we discuss motion segmentation approaches. Afterwards, the continuous cuts framework is introduced in Section 1.4. Finally, we address in Section 1.5 some possibilities for the optimisation and discuss in Section 1.6 the inclusion of landmark correspondences into the image registration methods.

The last section of this chapter, Section 1.7, gives an outline of this thesis and summarises the contributions.

1.1 Image Registration

Image registration is an ill-posed inverse problem and therefore a rather difficult task. To solve the problem, usually additional constraints are required like adding for example a regularisation term or making prior assumptions about the sought transformation. Image registration has a wide range of applications, not only in the medical field but also especially in remote sensing and computer vision [94]. Introductions to image registration and surveys of well-known methods can be found for example in [15, 45, 94, 25, 59] and the references therein.

In this section we would like to briefly address some general and important points of image registration. This outline is mainly based on the above mentioned surveys and we refer the interested reader to these works and the references therein for further reading.

1.1.1 The Principle of Image Registration

The aim of image registration is to estimate a transformation, that relates the positions of features in one image to the corresponding positions in other images. With the help of the determined transformation, the images can then be spatially aligned.

During image registration two images are considered, where one is regarded as static and the other one is transformed. There exist many dif-

ferent terms for these two images (see *e.g.* Appendix 1 in [25]), which can cause a confusion when they are not used in a consistent way. In this thesis, the static image will be always referred to as the *reference* image R and the image which is being transformed will be called the *template* image T .

More specifically, we define by $\Omega \subset \mathbb{R}^d$, $d \in \mathbb{N}$, the domain of the pixel positions $\vec{x} = (x_1, x_2, \dots, x_d)$ and then by the functions $R : \Omega \rightarrow \mathbb{R}$ and $T : \Omega \rightarrow \mathbb{R}$ our reference and template image. After a proper registration of the two images, the relation

$$T \circ \Phi \approx R, \quad (1.1)$$

should hold, where Φ is the *transformation* function. The transformation can also be written as

$$\Phi(\vec{x}) := \vec{x} + \vec{w}(\vec{x}), \quad (1.2)$$

where

$$\vec{w} : \Omega \rightarrow \mathbb{R}^d, \quad (1.3)$$

describes the so called *displacement field*. This will be the intrinsic function we are focusing on in this thesis.

An illustration to the introduced terms for image registration is shown in Fig. 1.2.

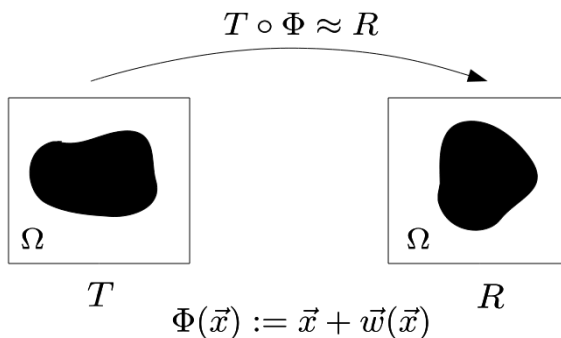


Figure 1.2: An illustration of the principle of image registration.

Here, we will work with two-dimensional images ($d = 2$) and the displacement field \vec{w} therefore consists then of the two components $u, v : \Omega \rightarrow \mathbb{R}$ with $\vec{w}(\vec{x}) := (u(\vec{x}), v(\vec{x}))$. For convenience we will use later the abbreviations \vec{w} , u and v for $\vec{w}(\vec{x})$, $u(\vec{x})$ and $v(\vec{x})$.

The estimation of the transformation Φ , respectively the displacement \vec{w} , can be performed by considering all the pixel positions $\vec{x} \in \Omega$ or only a subset of them. In our proposed variational approaches we will be estimating them by considering the whole domain Ω .

1.1.2 The Right Choice of an Image Registration Method

The choice of a suitable image registration method varies from application to application and depends on different aspects, mainly on the type of images, the complexity of the assumed motion, the aimed accuracy and the desired time of computation.

Rigid versus Non-Rigid Registration Methods

Nowadays, there exist plenty of different image registration methods and one can find many different variants in the literature on how to group them (see *e.g.* [15, 94, 59]). Concerning the type of transformation, they can be subdivided into those methods which are capable to estimate a rigid transformation or more generally an affine transformation between the images and those which are able to capture a more complex motion by determining a non-rigid transformation. In a similar fashion, one can talk about parametric and non-parametric image registration methods or about feature-based and intensity-based image registration methods, to just mention a few more possible classifications. Rigid image registration methods are in general easier to implement and faster than the non-rigid ones. However, depending on the kind of apparent motion, one has to be aware of most likely obtaining less accurate results when using rigid registration instead of non-rigid registration. Especially in the medical field, there is the need for non-rigid registration methods. For images of bones and often also for images of the brain rigid registration methods are accurate enough, whereas for the correct estimation of soft-tissue deformations non-rigid registration methods are crucial. References to rigid registration methods can be found for example in the works [89, 33, 45] and some non-rigid methods that became very popular in the medical field are for example the ones proposed by Thirion [82] and Rueckert *et al.* [72].

Similarity Measures

Next, having a look at the modalities of the images one wants to register, intensity-based image registration methods need to have an appropriate similarity measure between the warped template image $T \circ \Phi$ and the reference image R to be able to deliver satisfying registration results. For mono-modal images, the similarity measure is often chosen as the sum of squared differences (SSD), the sum of absolute differences (SAD) or the correlation coefficient (CC). On the other hand, for multi-modal images, the use of mutual

information (MI) or normalised mutual information (NMI) is very popular. We refer the reader to [45] for a more detailed discussion on similarity measures. In the following chapters, we will make use of similarity measures that are based on the grey value constancy constraint

$$R(\vec{x}) = T(\vec{x} + \vec{w}),$$

and the gradient constancy constraint

$$\nabla R(\vec{x}) = \nabla T(\vec{x} + \vec{w}),$$

similar as in [16, 4, 5]. The grey value constancy constraint alone cannot handle slight brightness changes in the images, whereas, similarly to the CC, the gradient constancy constraint can do so.

Interpolation Methods

Another important component in image registration methods is the interpolation method that is used to calculate the warped template image. The transformation function Φ does not necessarily map the pixel positions again to exact pixel locations. In fact, usually the mapped values fall in between pixel positions. To be able to estimate the grey values of the template image T at this positions and finally calculating the warped image $T \circ \Phi$, an interpolation method is needed. Commonly used methods are for example the nearest neighbour, the bilinear or the bicubic interpolation. During the iterations of intensity-based image registration methods, the current estimate of the transformation function Φ is updated by considering the quality of the similarity measure, which in turn depends on the warped template image $T \circ \Phi$ and the reference image R . The calculation of the warped image $T \circ \Phi$ is therefore performed several times during the registration procedure and interpolation artefacts influence the registration result and its accuracy. However, the computational complexity increases for interpolation methods with higher accuracy and in the end, one is forced to make a compromise between accuracy and computational efficiency of the image registration method.

Image Registration as an Optimisation Task

Image registration is an optimisation task and the right choice of an optimisation method can facilitate and speed up the registration process immensely. However, this choice is mostly not straightforward and becomes somehow an optimisation problem itself. The optimisation of a cost function for image registration is almost always a non-linear and non-convex problem, especially for non-rigid registration methods. The risk of getting stuck in local

optima during optimisation is therefore very high. Some remedies have to be found, like for example providing a good initial guess, applying a hierarchical approach and so on. A common approach to find a good initial guess for non-rigid registration methods, is to roughly align the images first by applying a rigid registration method. Finally, a global optimum is not always the desired one, as it can provide a physically unreliable transformation. In this case, additional constraints have to be embedded into the optimisation problem. In the end, sometimes only a careful inspection of the registration result can confirm that the correct optimum has been found.

1.1.3 The Validation of Image Registration Methods

The validation of an image registration method consists not only of a qualitative evaluation of the results by visual assessment, but also of a quantification of the registration accuracy. Especially when an image registration method is intended for clinical use, where inaccurate registration results could cause severe consequences, a prior proper validation of the method is indispensable.

Visual Assessment

The first obvious way to validate the registration results is a visual assessment, which is ideally performed by a medical expert and consist for example of a colour overlay, a difference image, or a chequerboard representation of the registered template and reference image. This will, however, provide only a qualitative validation of the image registration method.

Comparison of Similarity Measures

Another way to compare the registered template image to reference image is to calculate the similarity between them by making use of a similarity measure, like for example the ones mentioned in Section 1.1.2. For a quantitative validation, the so gained values can then be compared to the corresponding values before registration and additionally to the resulting similarity values of other registration methods. To prevent a biased comparison, one should use similarity measures that are *independent* of the considered registration methods. In the following chapters for example, we will make use of the mean squared error (MSE) and the normalised mutual information (NMI) to perform a quantitative comparison. With the definitions from Section 1.1.1 and by denoting the discrete pixel positions as \vec{x}_k with $k = 1, \dots, N$, we can

define the mean squared error by

$$\text{MSE} := \frac{1}{N} \sum_{k=1}^N (T(\vec{x}_k + \vec{w}(\vec{x}_k)) - R(\vec{x}_k))^2.$$

Furthermore, by considering two images A and B , whose intensity values lie in the set $\{0, 1, \dots, 255\}$, the normalised mutual information can be defined by

$$\text{NMI} := \frac{H(A) + H(B)}{H(A, B)},$$

where H is the so called entropy measure. The entropy of A is given by

$$H(A) := - \sum_{a=0}^{255} p(a) \log(p(a)),$$

where $p(a)$ is the probability that image A takes the intensity value a . Similarly, we can define the entropy of image B given by $H(B)$. The probabilities $p(a)$ respectively $p(b)$ can be deduced from the corresponding intensity histograms of the images A and B . Finally, the joint entropy $H(A, B)$ is defined by

$$H(A, B) := - \sum_{a=0}^{255} \sum_{b=0}^{255} p(a, b) \log(p(a, b))$$

where $p(a, b)$ is the joint probability that image A takes the intensity value a and image B takes value b . For the registered template image and the reference image, the normalised mutual information can then be calculated by first transforming the corresponding intensity values to the set $\{0, 1, \dots, 255\}$ and finally using the formulas given above.

Robustness and Consistency Tests

The robustness of an image registration method can be determined by the discrepancy of the resulting transformation, when different initialisations for the algorithm are used [81] or the images are perturbed by for example adding noise. There exist also various other types of consistency tests for the validation of an image registration method [36, 90, 46]. One can for example check whether the registration of the template to the reference image results into the same alignment like when registering the reference to the template image. However, especially for non-rigid registration methods this is rather

unlikely. To automatically satisfy this one-to-one mapping property and to guarantee a preservation of the topology, the so called diffeomorphic image registration methods were introduced and we refer the reader in this context to the works [7, 83] and the references therein. Another common approach for consistency checking is to use three images A , B , C , and for a perfect registration method the composition of the estimated transformations from A to B , B to C and C to A should turn out to be the identity transformation. In reality, however, the resulting transformation won't be the identity, but one can draw conclusions about the registration accuracy of the method by considering the resulting transformation's deviation from identity. Since the individual transformations between the different image pairs of A , B and C are not independent from each other, they always have one image in common, one should keep in mind that the true error of the method can be underestimated.

Validation by Using Known Landmark Correspondences

Another common validation approach, *independently* of the used registration method, consist of the determination of corresponding landmark positions (the so called target points [33]) or regions in both images. The so gained correspondences are then compared after registration and the alignment error calculated. For rigid image registration methods an error analysis based on fiducial points has been derived by Fitzpatrick *et al.* in [33] and further extended in [32]. Such an error analysis can, however, not be performed for non-rigid image registration methods.

Validation by Using Gold Standards

Test images, for which the transformation is known, can also be used to validate the image registration method. The transformation that is estimated by the registration method is then compared to the so called "gold standard" transformation. Whereas it is easy to create simple synthetic test images with uncomplicated transformations, the generation of real-world test images with physically reasonable transformations is, however, not so straightforward. Schnabel *et al.* [74] proposed a way to simulate biomechanical deformations in human breast tissue by using the finite element method. The so gained simulated transformations were then used as a gold standard for validation. In [86], a fiducial-based thin-plate spline method was used to calculate a gold standard transformation for a pair of sequential CT images. The so gained transformation was then used to create the test images for validation. If the transformation is, however, unknown, as it is normally the case, another

image registration method, which is known to perform very well on the given images, can be used as a gold standard method for validation, as it was for example done in the comprehensive evaluation project of West *et al.* [89] for intermodality rigid-registration methods or in the work of Wang *et al.* [86] for a intramodality non-rigid registration method with the help of fiducial markers.

1.2 Optical Flow

A closely related field from computer vision to image registration is the one called optical flow. Optical flow is the apparent motion in a sequence of images and can be defined as the two-dimensional velocity field that describes the changes in intensity between the images. Surveys and discussions to optical flow methods can be found for example in [9, 10, 34, 87].

Some of the first methods that were proposed to calculate the optical flow between images are the global variational method of Horn and Schunck [47] and the local method of Lucas and Kanade [57], which were both introduced in 1981. Since then optical flow became an active field of research and several of the proposed methods were based on these works. Many methods make for example use of the so called *optical flow constraint* (OFC) [47], where it is assumed that the intensity of a point in the image keeps constant during its movement over time. More precisely, for $I(x, y, t)$ being the intensity value at the point (x, y) in the image to the time t , the OFC is given by

$$I_x(x, y, t) u(x, y) + I_y(x, y, t) v(x, y) + I_t(x, y, t) = 0,$$

where (u, v) denotes the optical flow. This constraint is, however, not enough to estimate both components of the optical flow. This problem is known as the *aperture problem* and Horn and Schunck [47] resolved it by introducing an additional smoothness constraint for the optical flow. In their variational approach they minimise the energy functional

$$\begin{aligned} E_{HS}(u, v) = & \int_{\Omega} (I_x(x, y, t) u(x, y) + I_y(x, y, t) v(x, y) + I_t(x, y, t))^2 dx dy \\ & + \mu \int_{\Omega} |\nabla u(x, y)|^2 + |\nabla v(x, y)|^2 dx dy, \end{aligned}$$

where $\Omega \subset \mathbb{R}^2$ is the domain of the points (x, y) and $\mu \in \mathbb{R}^+$ is a weighting parameter. The OFC usually only holds for small displacements (u, v) and therefore it is rather difficult to estimate large motions with its help. To be able to cope with large displacements it became thus common to apply

coarse-to-fine strategies in optical flow methods [11, 58, 16]. Furthermore, slight brightness changes in the images can already cause problems in the OFC and remedies have to be found, like for example considering the gradient constancy constraint [16] or introducing an additional function that explicitly models illumination changes [20].

In contrast to image registration, a lot of research was also done in estimating discontinuous optical flow respectively discontinuous displacement fields. See for example [61, 75, 62, 11, 8, 58, 16, 4, 24, 5, 17, 67, 92]. Making use of these investigations in image registration therefore seems likely. Many of the proposed methods are using for example the total variation of the displacement fields as a smoothness constraint, that is known to preserve discontinuities and was first applied in computer vision by Rudin *et al.* [71] for image denoising. Other interesting methods use the concept of motion segmentation to preserve discontinuities in the displacement field.

In the following we would like to recapitulate in Section 1.2.1 the variational optical flow method of Brox *et al.* [16], that became popular because of its robust and accurate optical flow estimation. Our first proposed method in Chapter 2 incorporates the optical flow method of Brox *et al.* [16] and in our following proposed methods in Chapter 3 and Chapter 4 related formulations are used for the energy functionals.

1.2.1 The Optical Flow Method of Brox

The variational method of Brox *et al.* [16] is known to produce very accurate optical flow estimations. To achieve discontinuities in the displacement field, an approximation of the total variation was used as a smoothness constraint. The authors worked with image sequences $I : \Omega \times [0, t_{end}] \rightarrow \mathbb{R}$, where $\Omega \subset \mathbb{R}^2$ is the domain of the pixel positions \vec{x} and $t_{end} \in \mathbb{R}^+$ denotes the point of time to the last image in the sequence. For later use, we will write down the proposed energy functional in [16] by assuming that the image sequence I consist of only two images. By adopting the notations from Section 1.1.1, we call the first image the reference image R and the second one the template image T . Furthermore, we also take over the notations for the displacement field \vec{w} with its two components u and v .

Brox *et al.* [16] incorporated in their energy functional the grey value constancy constraint

$$R(\vec{x}) = T(\vec{x} + \vec{w}),$$

and the gradient constancy constraint

$$\nabla R(\vec{x}) = \nabla T(\vec{x} + \vec{w}).$$

More specifically, their fidelity term f and their smoothness term s are defined by

$$\begin{aligned} f(\vec{w}) = f(u, v) &:= \Psi \left(|T(\vec{x} + \vec{w}) - R(\vec{x})|^2 + \gamma |\nabla T(\vec{x} + \vec{w}) - \nabla R(\vec{x})|^2 \right) \text{ and} \\ s(\vec{w}) = s(u, v) &:= \Psi \left(|\nabla u|^2 + |\nabla v|^2 \right), \end{aligned} \quad (1.4)$$

where $\gamma \in \mathbb{R}_0^+$ is a weighting parameter between the grey value constancy constraint and the gradient constancy constraint and the function $\Psi(z^2) = \sqrt{z^2 + \epsilon^2}$, with $\epsilon \in \mathbb{R}^+$ small, results in an approximation of the L^1 -norm. Furthermore, Ψ is concave in terms of z^2 , thus being robust against outliers, and convex with respect to z , which facilitates the minimisation process of the total energy functional

$$E_{Brox}(\vec{w}) = \int_{\Omega} f(\vec{w}) + \mu s(\vec{w}) d\vec{x}. \quad (1.5)$$

The regularisation through the smoothness term s is weighted by a parameter $\mu \in \mathbb{R}^+$ and results in an approximation of the vectorial total variation of the displacement field \vec{w} . Thus, discontinuities in the displacement field are expected to be preserved.

In the end, the energy functional Eq. (1.5) is minimised in a coarse-to-fine strategy with the help of a fixed point iteration scheme that is derived from the corresponding Euler-Lagrange equations.

1.3 Motion Segmentation

Discontinuities in the displacement field mainly appear at the boundaries of moving objects in the images. Therefore the prior knowledge of motion boundaries could support the estimation of discontinuous displacement fields inherently. On the other hand, when having the knowledge of a proper discontinuous displacement field, the calculation of the motion segmentation can be performed without any problems. Thus, we have a chicken-and-egg problem since in general the proper motion segmentation and the discontinuous displacement field are unknown in advance.

Many methods were proposed to combine motion segmentation with the optical flow estimation to achieve discontinuous displacement fields, as it was for example done in the works [75, 62, 58, 24, 4, 5, 17]. The level set approaches of Amiaz and Kiryati [4, 5] inspired us to the development of our proposed discontinuity preserving registration methods, that are presented in the following chapters. We therefore would like to recapitulate the idea behind their method, which is based on the optical flow method of Brox *et*

al. [16], that was presented in Section 1.2.1, and the level set approach of Vese and Chan [84] for image segmentation, that tries to solve the Mumford and Shah segmentation problem. Before explaining the segmentation approach of Vese and Chan [84] more detailed in Section 1.3.2, we address the Mumford and Shah segmentation problem in Section 1.3.1. In Section 1.3.3, we introduce then the motion segmentation approach of Amiaz and Kiryati [4, 5].

1.3.1 The Mumford and Shah Segmentation Problem

Let $\Omega \subset \mathbb{R}^d$, $d \in \mathbb{N}$, be an open and bounded set and let us denote by the function $g : \Omega \rightarrow \mathbb{R}$ the given image we would like to segment. For the purpose of illustration we consider only the two-dimensional case $d = 2$ in the following, although the domain Ω could be basically of any dimension. Mumford and Shah [60] described the segmentation problem in computer vision as the computation of a partition of the domain $\Omega = \dot{\cup}_{i=1}^n \Omega_i \dot{\cup} \Gamma$ such that g varies smoothly within each Ω_i and discontinuously across the boundary Γ between the different Ω_i 's. Thus, they proposed to minimise the following energy functional

$$E_{MS}(\tilde{g}, \Gamma) = \int_{\Omega} (\tilde{g}(\vec{x}) - g(\vec{x}))^2 d\vec{x} + \mu \int_{\Omega \setminus \Gamma} |\nabla \tilde{g}(\vec{x})|^2 d\vec{x} + \nu |\Gamma|, \quad (1.6)$$

where $|\Gamma|$ is the length of the boundary Γ , $\mu, \nu \in \mathbb{R}_0^+$ are weighting parameters and the function $\tilde{g} : \Omega \rightarrow \mathbb{R}$ is then a piecewise smooth approximation of g .

The Mumford-Shah problem was studied thoroughly in the last decades and theoretical results for the existence and regularity of minimisers were established. In practise it is not easy to minimise the Mumford-Shah energy functional Eq. (1.6) because of the lower dimensionality of the unknown boundary Γ and the non-convexity of the minimisation problem. Plenty of methods were proposed to solve the Mumford-Shah problem, amongst others for example the Ambrosio and Tortorelli approaches with their Γ -convergence results [2, 3], the level set approaches of Chan and Vese [22, 84] and the recently proposed approach of Pock *et al.* [66].

In the following section we would like to focus on the level set approach of Vese and Chan [84].

1.3.2 The Level Set Approach of Vese and Chan

The level set approaches of Chan and Vese [22, 84] provide an efficient way to solve the Mumford-Shah segmentation problem by reformulating and ap-

proximating the Mumford-Shah energy functional Eq. (1.6) for particular cases.

The key idea behind the level set approaches is to implicitly represent a boundary set with the zero level set of a function. Osher and Sethian [64] proposed this representation to track evolving curves and surfaces and thereby provided the foundation of the so called level set methods. We refer the reader to [76], [63] for further reading.

Now, let $\Omega \subset \mathbb{R}^2$ be an open and bounded set and $\Sigma \subseteq \Omega$ an open subset. Furthermore, let $\phi : \Omega \rightarrow \mathbb{R}$ be a Lipschitz continuous function such that

$$\begin{aligned}\phi(\vec{x}) &> 0 && \text{if } \vec{x} \in \Sigma, \\ \phi(\vec{x}) &< 0 && \text{if } \vec{x} \in \Omega \setminus \Sigma \text{ and} \\ \phi(\vec{x}) &= 0 && \text{if } \vec{x} \in \Gamma = \partial\Sigma.\end{aligned}$$

Thus, the boundary Γ is implicitly given by the zero level set of the function ϕ . See Fig. 1.3 for an illustration. The function ϕ is known as the level set

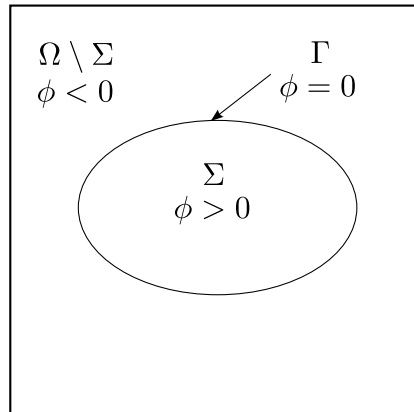


Figure 1.3: The boundary Γ is implicitly represented by the zero level set of the function ϕ .

function and a typical example of it is the signed distance function to the boundary Γ .

For the formulation of the Vese and Chan energy functionals [84], one also needs the so called Heaviside function $H : \mathbb{R} \rightarrow \{0, 1\}$ defined by

$$H(z) = \begin{cases} 1 & \text{if } z \geq 0, \\ 0 & \text{if } z < 0. \end{cases}$$

Note, that one can then rewrite the length of the boundary Γ as

$$|\Gamma| = \int_{\Omega} |DH(\phi(\vec{x}))| d\vec{x}.$$

See for example [28] and compare also to the Definition 1.3 in Section 1.4.1 for a deeper insight.

First, Chan and Vese proposed in [22] a level set approach to calculate a piecewise constant approximation \tilde{g} of an image g , where \tilde{g} can take only two values. Their suggested energy functional for minimisation turns out to be a special case of the Mumford-Shah functional with a piecewise constant function \tilde{g} in Eq. (1.6). Later on, Vese and Chan [84] extended their level set approach to calculate piecewise constant approximations that can take more than two values and further enhanced their model to calculate piecewise smooth approximations. Again the proposed energy functionals for minimisation are closely related to the Mumford-Shah functional Eq. (1.6).

The Vese and Chan energy functional for the piecewise smooth case with one level set function for example (see [84]) is given by

$$\begin{aligned}
E_{VC}(\tilde{g}^+, \tilde{g}^-, \phi) &= \int_{\Omega} (\tilde{g}^+(\vec{x}) - g(\vec{x}))^2 H(\phi(\vec{x})) d\vec{x} \\
&+ \int_{\Omega} (\tilde{g}^-(\vec{x}) - g(\vec{x}))^2 (1 - H(\phi(\vec{x}))) d\vec{x} \\
&+ \mu \int_{\Omega} |\nabla \tilde{g}^+(\vec{x})|^2 H(\phi(\vec{x})) d\vec{x} \\
&+ \mu \int_{\Omega} |\nabla \tilde{g}^-(\vec{x})|^2 (1 - H(\phi(\vec{x}))) d\vec{x} \\
&+ \nu \int_{\Omega} |\nabla H(\phi(\vec{x}))| d\vec{x}, \tag{1.7}
\end{aligned}$$

where $\mu, \nu \in \mathbb{R}_0^+$ are weighting parameters and

$$\begin{aligned}
\tilde{g}^+ &\in C^1(\Sigma; \mathbb{R}) = C^1(\{x \in \Omega \mid \phi(\vec{x}) \geq 0\}; \mathbb{R}), \\
\tilde{g}^- &\in C^1(\Omega \setminus \Sigma; \mathbb{R}) = C^1(\{x \in \Omega \mid \phi(\vec{x}) \leq 0\}; \mathbb{R}).
\end{aligned}$$

The final piecewise smooth approximation $\tilde{g} : \Omega \rightarrow \mathbb{R}$ of the image $g : \Omega \rightarrow \mathbb{R}$ is then obtained by setting

$$\tilde{g}(\vec{x}) = \tilde{g}^+(\vec{x}) H(\phi(\vec{x})) + \tilde{g}^-(\vec{x}) (1 - H(\phi(\vec{x}))) \quad \text{for all } \vec{x} \in \Omega.$$

Note, that we used the notation $\nabla H(\phi(\vec{x}))$ instead of using the correct weak derivative formulation $DH(\phi(\vec{x}))$ in the last term of Eq. (1.7). For the facilitation of the minimisation Chan and Vese proposed in their works [22, 84] to take into account a regularised version H_ϵ as an approximation of the Heaviside function H with $H_\epsilon \rightarrow H$ as $\epsilon \rightarrow 0$. Thus, we consider from now on H to be H_ϵ and therefore the notation of the strong derivative to be acceptable.

As we can see, the Vese-Chan energy functional E_{VC} in Eq. (1.7) is a reformulation of the Mumford-Shah energy functional E_{MS} in Eq. (1.6) by making use of the level set framework.

Depending on the image g one aims to segment, sometimes one level set function is not enough to represent the optimal boundary set Γ . Therefore, Vese and Chan showed in [84] how one can formulate an energy functional for the piecewise smooth case with two level set functions and stated that in general not more than two level set functions are needed.

Finally, all the proposed energy functionals of Vese and Chan [84] were minimised in an iterative scheme by deriving explicit solutions where it is possible or by solving the corresponding Euler-Lagrange equations.

1.3.3 The Approach of Amiaz and Kiryati

The optical flow method of Amiaz and Kiryati [4, 5] is a motion segmentation approach. Their idea is to embed the optical flow method of Brox *et al.* [16] (see Section 1.2.1) into the piecewise smooth segmentation framework of Vese and Chan [84] (see Section 1.3.2). The so achieved optical flow method is then able to calculate piecewise smooth displacement fields with sharp discontinuities.

Let $\Omega \subset \mathbb{R}^2$ be an open and bounded set containing the pixel positions \vec{x} . Furthermore, we recall the definitions of the level set function ϕ and the regularised Heaviside function H from Section 1.3.2. The energy functional proposed by Amiaz and Kiryati [4, 5] is then given by

$$\begin{aligned}
 E_{AK}(\vec{w}^+, \vec{w}^-, \phi) &= E_{AK}(u^+, v^+, u^-, v^-, \phi) \\
 &= \int_{\Omega} f(\vec{w}^+) H(\phi(\vec{x})) d\vec{x} + \int_{\Omega} f(\vec{w}^-) (1 - H(\phi(\vec{x}))) d\vec{x} \\
 &+ \mu \int_{\Omega} s(\vec{w}^+) H(\phi(\vec{x})) d\vec{x} + \mu \int_{\Omega} s(\vec{w}^-) (1 - H(\phi(\vec{x}))) d\vec{x} \\
 &+ \nu \int_{\Omega} |\nabla H(\phi(\vec{x}))| d\vec{x}, \tag{1.8}
 \end{aligned}$$

where $\mu, \nu \in \mathbb{R}_0^+$ are again weighting parameters, f and s are defined as in Eq. (1.4) in Section 1.2.1 and $\vec{w}^+, \vec{w}^- : \Omega \rightarrow \mathbb{R}^2$ make up the final displacement field $\vec{w} : \Omega \rightarrow \mathbb{R}^2$ by setting

$$\vec{w}(\vec{x}) = \vec{w}^+(\vec{x}) H(\phi(\vec{x})) + \vec{w}^-(\vec{x}) (1 - H(\phi(\vec{x}))) \quad \text{for all } \vec{x} \in \Omega.$$

The energy functional Eq. (1.8) was minimised by iteratively solving the corresponding Euler-Lagrange equations. The Euler-Lagrange equations for

the displacement fields \vec{w}^+ and \vec{w}^- were solved with a fixed point iteration scheme, that is related to the one proposed by Brox *et al.* [16]. For the level set function ϕ , the Euler-Lagrange equation was solved similar as in Vese and Chan's work [84] through a gradient descent equation. Amiaz and Kiryati [4, 5] proposed different ways for the initialisation of the displacement fields \vec{w}^+ , \vec{w}^- and the level set function ϕ and showed amongst others improved results in comparison to Brox *et al.*'s optical flow method [16]. For further reading, we refer the reader also to the subsequent motion segmentation approach of Brox *et al.* [17] that is related to the ones of Amiaz and Kiryati [4, 5].

1.4 Continuous Cuts Framework

Inspired by the works of Strang [78, 79], Chan *et al.* [21] proposed a promising algorithm that is able to calculate global minimisers of certain non-convex optimisation problems that appear in the field of image segmentation and image denoising. The basic idea is to reformulate the original non-convex problem into a convex one and to show that a global minimiser of the original problem can be found by solving its convex reformulation followed by a thresholding of the so obtained result.

The approach of Chan *et al.* [21], sometimes also called "continuous cuts" [37], is a convex relaxation approach and it was further studied and improved by Bresson *et al.* in [13]. Convex relaxation approaches became an active field of research in computer vision during the last few years, since they are able to easily find solutions that are equal or close to the global minimisers of non-convex optimisation problems which are in general difficult to solve. Recently, Brown *et al.* [14] proposed for example a method to find a global minimiser of the total Chan-Vese segmentation problem [22] by reformulating it completely into a convex one. Further interesting papers about convex relaxation approaches can be found for example in the references of [14].

As in the sections before, let again $\Omega \subset \mathbb{R}^2$ be an open and bounded set, ϕ the level set function and H the Heaviside function. We consider now a general energy functional of the form

$$E_\phi(\phi) = \int_{\Omega} D^+(\vec{x}) H(\phi(\vec{x})) d\vec{x} + \int_{\Omega} D^-(\vec{x}) (1 - H(\phi(\vec{x}))) d\vec{x} + \nu \int_{\Omega} |\nabla H(\phi(\vec{x}))| d\vec{x}, \quad (1.9)$$

where $\nu \in \mathbb{R}_0^+$ is a weighting parameter and $D^+, D^- : \Omega \rightarrow \mathbb{R}$ are measurable functions. For the Vese and Chan energy functional Eq. (1.7) in Section 1.3.2

these functions would be for example

$$D^\pm(\vec{x}) = (\tilde{g}^\pm(\vec{x}) - g(\vec{x}))^2 + \mu |\nabla \tilde{g}^\pm(\vec{x})|^2,$$

for some fixed \tilde{g}^\pm . Similarly, one gets for the energy functional of Amiaz and Kiryati Eq. (1.8) in Section 1.3.3

$$D^\pm(\vec{x}) = f(\vec{w}^\pm) + \mu s(\vec{w}^\pm),$$

for fixed values of \vec{w}^\pm .

The energy functional Eq. (1.9) is non-convex with respect to ϕ and therefore there is a high risk of getting stuck in a local minimum during the minimisation procedure. To leverage this risk, we would like to follow the initial approach of Chan *et al.* [21] that supports us in finding a global minimum for the segmentation.

Before explaining the approach in more detail, we would like to recapitulate in Section 1.4.1 some mathematical definitions and theorems we will need then later on. In Section 1.4.2, we present then a global minimiser theorem by following the concepts in [21].

1.4.1 Some Mathematical Definitions and Theorems

In the following we would like to recall some mathematical definitions and properties, most of them originating from the theory of functions of bounded variation. Some famous textbooks in this context are [1], [28], [38] and [93]. We will use then these theoretical foundations in the next section to prove a global minimiser theorem.

First of all, let us recall the layer cake representation theorem, which is a useful tool in mathematics.

Theorem 1.1 (Layer Cake Representation). *Let $f : \Omega \subseteq \mathbb{R}^n \rightarrow \mathbb{R}_0^+$ be a real-valued, non-negative measurable function. From the formula $f(x) = \int_0^{f(x)} 1 dt$ it easily follows the layer cake representation*

$$f(x) = \int_0^\infty \mathbf{1}_{L(f,t)}(x) dt \quad \forall x \in \Omega,$$

where $\mathbf{1}_A$ is the characteristic function (or indicator function) of a subset $A \subseteq \mathbb{R}^n$ and $L(f, t) = \{x \in \Omega \mid f(x) \geq t\}$ the upper level set of f .

Remark 1.1. The formula is called layer cake representation because the value $f(x)$ is represented with the help of the layers $L(f, t)$.

Remark 1.2. A more general formulation of the layer cake representation and its proof can be found for example in [55].

Remark 1.3. Instead of using the original layer cake representation in Theorem 1.1 we will use the equivalent formulation

$$f(x) = \int_0^\infty \mathbf{1}_{\tilde{L}(f,x)}(t) dt \quad \forall x \in \Omega,$$

where $\tilde{L}(f, x) = \{t \in \mathbb{R}_0^+ \mid f(x) \geq t\}$.

Next, we present an essential definition in the theory of functions of bounded variation, namely the one of the total variation.

Definition 1.1 (Total Variation). Let $\Omega \subseteq \mathbb{R}^n$ be an open set. The total variation of a function $u \in L^1_{\text{loc}}(\Omega)$ is defined as

$$TV(u) = \int_\Omega |Du| := \sup \left\{ \int_\Omega u(x) \operatorname{div} \varphi(x) dx \mid \varphi \in C_c^1(\Omega, \mathbb{R}^n), \|\varphi\|_\infty \leq 1 \right\}.$$

With the help of the total variation one is able to define the space of functions of bounded variation.

Definition 1.2 (The Space BV). Let $\Omega \subseteq \mathbb{R}^n$ be an open set. The Banach space of functions of bounded variation is defined as

$$BV(\Omega) := \{u \in L^1(\Omega) \mid TV(u) < \infty\},$$

and its norm is given by $\|u\|_{BV} := \|u\|_{L^1} + TV(u)$.

The following definition of the perimeter of a set will be also of importance afterwards.

Definition 1.3 (Perimeter). Let $\Omega \subseteq \mathbb{R}^n$ be an open set and $E \subseteq \Omega$ be a measurable set. The perimeter of E in Ω is defined as

$$\operatorname{Per}(E, \Omega) := TV(\mathbf{1}_E) = \int_\Omega |D\mathbf{1}_E|,$$

where $\mathbf{1}_E$ is the characteristic function of E .

A fundamental and very useful result in mathematics is the so-called coarea formula. It is known to be a helpful tool in many mathematical proofs and in the following we state the first established coarea formula.

Theorem 1.2 (Coarea Formula of Federer). *Let $\Omega \subseteq \mathbb{R}^n$ be an open set and $u : \Omega \rightarrow \mathbb{R}^k$, with $1 \leq k < n$, a Lipschitz function. For a function $g \in L^1(\Omega)$ the coarea formula is given by*

$$\int_{\Omega} g(x) \mathcal{J}u(x) dx = \int_{\mathbb{R}^k} \left(\int_{u^{-1}(y)} g(x) d\mathcal{H}^{n-k}(x) \right) dy,$$

where $\mathcal{J}u(x)$ is the Jacobian of u at x and \mathcal{H}^{n-k} is the $(n - k)$ -dimensional Hausdorff measure.

Remark 1.4. The Jacobian of u at x , also known as the functional determinant, is given by $\mathcal{J}u(x) := \sqrt{\det(J_u(x)^T \cdot J_u(x))}$, where $J_u(x)$ is the Jacobian matrix of u at x .

Remark 1.5. With $k = 1$ and $g \equiv 1$ we get

$$\int_{\Omega} |\nabla u(x)| dx = \int_{-\infty}^{\infty} \left(\int_{u^{-1}(y)} 1 d\mathcal{H}^{n-1}(x) \right) dy = \int_{-\infty}^{\infty} \mathcal{H}^{n-1}(u^{-1}(y)) dy.$$

Remark 1.6. The coarea formula in Theorem 1.2 was first established by Federer and can be found for example in [29] or [30].

Note, that this coarea formula holds only for Lipschitz functions u . Since we would like to work with more general functions later on, we indicate in the following also a coarea formula that holds for functions u of bounded variation.

Theorem 1.3 (Coarea Formula of Fleming and Rishel). *Let $\Omega \subseteq \mathbb{R}^n$ be an open set and $u \in BV(\Omega)$. Then*

$$TV(u) = \int_{\Omega} |Du| = \int_{-\infty}^{\infty} \text{Per}(\{x \in \Omega \mid u(x) \geq t\}, \Omega) dt.$$

Remark 1.7. An analogue formula holds also for the perimeter of the lower level sets $\{x \in \Omega \mid u(x) \leq \eta\}$.

Remark 1.8. The formula in Theorem 1.3 was introduced by Fleming and Rishel [35]. It is an extension of the coarea formula of Federer in Theorem 1.2 for $k = 1$ and $g \equiv 1$ (cf. Remark 1.5) to functions of bounded variation $u \in BV(\Omega)$.

1.4.2 Global Minimiser

In this section we would like to show how we can make use of Chan *et al.*'s approach [21] to achieve a global minimiser for the segmentation.

First, note that we can write the energy functional Eq. (1.9) also as

$$E_{\Sigma}(\Sigma) = \int_{\Sigma} D^{+}(\vec{x}) d\vec{x} + \int_{\Omega \setminus \Sigma} D^{-}(\vec{x}) d\vec{x} + \nu \text{Per}(\Sigma, \Omega), \quad (1.10)$$

by using the definitions of the level set function ϕ and the Heaviside function H in Section 1.3.2. Thus, $\Sigma \subseteq \Omega \subset \mathbb{R}^2$ is the open subset over which the function ϕ is positive. Additionally, we also made use of Definition 1.3 in Section 1.4.1 for the perimeter, which represents in our case the length of the boundary Γ (see again Section 1.3.2).

To follow Chan *et al.*'s work [21], let us introduce now a binary function

$$\tilde{u} : \begin{cases} \mathbb{R}^2 \rightarrow \{0, 1\} \\ \vec{x} \mapsto \tilde{u}(\vec{x}) := \mathbf{1}_{\Sigma}(\vec{x}), \end{cases}$$

and we can write $\Sigma = \{\vec{x} \in \Omega \mid \tilde{u}(\vec{x}) = 1\}$. The function \tilde{u} can also be called the characteristic function or the indicator function of the set Σ . With its help we can reformulate then the energy functional Eq. (1.9) respectively Eq. (1.10) as

$$\begin{aligned} E_{\tilde{u}}(\tilde{u}) &= \int_{\Omega} D^{+}(\vec{x}) \tilde{u}(\vec{x}) d\vec{x} + \int_{\Omega} D^{-}(\vec{x}) (1 - \tilde{u}(\vec{x})) d\vec{x} \\ &\quad + \nu \int_{\Omega} |\nabla \tilde{u}(\vec{x})| d\vec{x}. \end{aligned} \quad (1.11)$$

Chan and Vese [22] mentioned also the possibility of this reformulation for their energy functional. For simplicity and to be consistent to the work of Chan *et al.* [21], we used the notation $\nabla \tilde{u}(\vec{x})$ instead of mathematically correctly using $D\tilde{u}(\vec{x})$.

We would like to point out again, that the energy functionals E_{ϕ} Eq. (1.9), E_{Σ} Eq. (1.10) and $E_{\tilde{u}}$ Eq. (1.11) are just different ways of formulations for the same energy.

Similar as in [21] we finally arrive at the theorem below that enables us to find a global minimum for the segmentation. The minimisation of the convex energy functional $E_{\tilde{u}}$ over the non-convex set of binary functions \tilde{u} is turned into a convex problem by allowing the feasible functions for \tilde{u} to take values between 0 and 1. The final binary function is then achieved by thresholding the optimal solution for this convexified problem. This thresholding can be interpreted as a cut and therefore this approach is also known as ‘‘continuous cuts’’ [37].

Theorem 1.4. *For any given functions $D^+, D^- : \Omega \rightarrow \mathbb{R}$ that are measurable, a global minimiser for $E_\Sigma(\cdot)$ can be found by solving the convex problem*

$$\min_{0 \leq \tilde{u} \leq 1} E_{\tilde{u}}(\tilde{u})$$

and finally setting

$$\Sigma = \Sigma(\eta) := \{\vec{x} \in \Omega \mid \tilde{u}(\vec{x}) \geq \eta\} \text{ for almost every } \eta \text{ with } \eta \in [0, 1].$$

Proof. The proof can be carried out similarly to the one in [21].

With the help of the layer cake representation in Theorem 1.1 respectively the subsequent Remark 1.3 in Section 1.4.1 we can write

$$\begin{aligned} \tilde{u}(\vec{x}) &= \int_0^1 \mathbf{1}_{\{\eta \in [0,1] \mid \tilde{u}(\vec{x}) \geq \eta\}}(\eta) \, d\eta \\ &= \int_0^1 \mathbf{1}_{[0, \tilde{u}(\vec{x})]}(\eta) \, d\eta. \end{aligned}$$

We get then

$$\begin{aligned} \int_{\Omega} D^+(\vec{x}) \tilde{u}(\vec{x}) \, d\vec{x} &= \int_{\Omega} D^+(\vec{x}) \int_0^1 \mathbf{1}_{[0, \tilde{u}(\vec{x})]}(\eta) \, d\eta \, d\vec{x} \\ &= \int_{\Omega} \int_0^1 D^+(\vec{x}) \mathbf{1}_{[0, \tilde{u}(\vec{x})]}(\eta) \, d\eta \, d\vec{x} \\ &\stackrel{\text{Fubini}}{=} \int_0^1 \int_{\Omega} D^+(\vec{x}) \mathbf{1}_{[0, \tilde{u}(\vec{x})]}(\eta) \, d\vec{x} \, d\eta \\ &= \int_0^1 \int_{\Omega \cap \{\vec{x} \mid \tilde{u}(\vec{x}) \geq \eta\}} D^+(\vec{x}) \, d\vec{x} \, d\eta \\ &= \int_0^1 \int_{\Sigma(\eta)} D^+(\vec{x}) \, d\vec{x} \, d\eta, \end{aligned}$$

with $\Sigma(\eta) := \{\vec{x} \in \Omega \mid \tilde{u}(\vec{x}) \geq \eta\}$. Similarly we obtain

$$\begin{aligned} \int_{\Omega} D^-(\vec{x}) (1 - \tilde{u}(\vec{x})) \, d\vec{x} &= \int_{\Omega} D^-(\vec{x}) \, d\vec{x} - \int_{\Omega} D^-(\vec{x}) \tilde{u}(\vec{x}) \, d\vec{x} \\ &= \int_0^1 \int_{\Omega} D^-(\vec{x}) \, d\vec{x} \, d\eta - \int_0^1 \int_{\Sigma(\eta)} D^-(\vec{x}) \, d\vec{x} \, d\eta \\ &= \int_0^1 \int_{\Omega \setminus \Sigma(\eta)} D^-(\vec{x}) \, d\vec{x} \, d\eta. \end{aligned}$$

With the help of the coarea formula in Theorem 1.3 in Section 1.4.1 and the fact that \tilde{u} takes its values in $[0, 1]$ we can furthermore write

$$\begin{aligned} \int_{\Omega} |\nabla \tilde{u}(\vec{x})| d\vec{x} &= \int_0^1 \text{Per}(\{\vec{x} \in \Omega \mid \tilde{u}(\vec{x}) \geq \eta\}, \Omega) d\eta \\ &= \int_0^1 \text{Per}(\Sigma(\eta), \Omega) d\eta. \end{aligned}$$

After putting then all together, we get the following relation between $E_{\tilde{u}}$ and E_{Σ} .

$$\begin{aligned} E_{\tilde{u}}(\tilde{u}) &= \int_0^1 \int_{\Sigma(\eta)} D^+(\vec{x}) d\vec{x} d\eta + \int_0^1 \int_{\Omega \setminus \Sigma(\eta)} D^-(\vec{x}) d\vec{x} d\eta \\ &\quad + \nu \int_0^1 \text{Per}(\Sigma(\eta), \Omega) d\eta \\ &= \int_0^1 E_{\Sigma}(\Sigma(\eta)) d\eta. \end{aligned} \tag{1.12}$$

Let now \tilde{u} be a minimiser of the convex problem

$$\min_{0 \leq \tilde{u} \leq 1} E_{\tilde{u}}(\tilde{u}).$$

Since the problem is convex, \tilde{u} is a global minimiser and from Eq. (1.12) it follows that for almost every $\eta \in [0, 1]$ the set $\Sigma(\eta)$ will be a global minimiser of the energy functional $E_{\Sigma}(\cdot)$. \square

We will make use of this general theorem in the following chapters. Our energy functionals there will, however, also be dependent on the displacement fields and therefore the overall minimisation problem will remain a non-convex one despite using Theorem 1.4. Nevertheless, with the above theorem we are able to say that a global minimiser for the segmentation can be found for *fixed* displacement fields.

In their work [21], Chan *et al.* applied the continuous cuts framework amongst others to the level set approach of Chan and Vese [22] for a piecewise constant approximation of an image, where the approximation can take only two values c_1 and c_2 . Similarly as we did before, they argued with the help of a theorem that a global minimiser for the segmentation can be found for *fixed* values of c_1 and c_2 . In Fig. 1.4 we show the results we obtained for this case. Similarly, we show in Fig. 1.5 the results we obtained when we applied the continuous cuts framework [21] to the level set approach of Vese and Chan [84] for a piecewise smooth approximation of an image with the help of one level

set function (see Eq. 1.7 in Section 1.3.2). To solve the in the continuous cuts framework reformulated problems numerically, we used a different approach than the one described in [21]. More specifically, we introduced an auxiliary variable \tilde{v} and made use of the fast numerical method of Chambolle [19], similar as it was done in [67, 92] (see also Chapter 2 later). As we can see in Fig. 1.4 and Fig. 1.5, the resulting segmentation function \tilde{u} gets close to a binary function although the minimisation is performed over non-binary functions. This phenomenon was also pointed out by Chan *et al.* [21] and we will see a similar behaviour for our motion segmentation approaches in the following chapters.

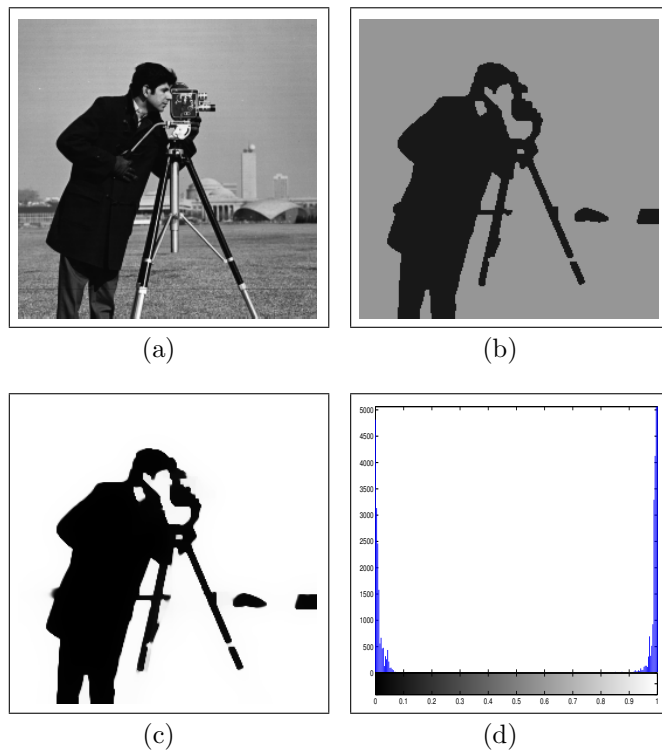


Figure 1.4: Application of the continuous cuts framework for a piecewise constant approximation of an image by two values. Here, (a) shows the input image, (b) the piecewise constant approximation and (c) the corresponding segmentation function \tilde{u} with its histogram (d).

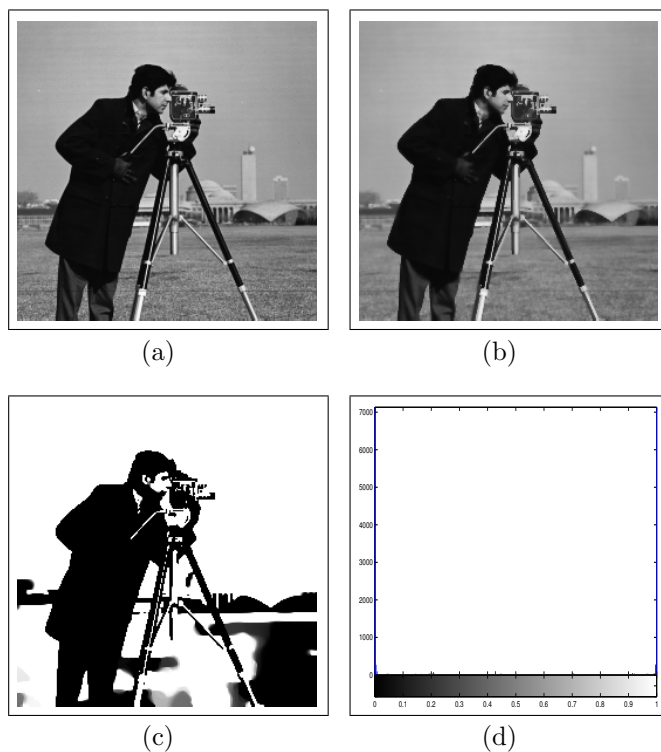


Figure 1.5: Application of the continuous cuts framework for a piecewise smooth approximation of an image. We show in (a) the input image, in (b) the piecewise smooth approximation and in (c) the corresponding segmentation function \tilde{u} with its histogram in (d).

1.5 Optimisation

Variational approaches are known to perform very well because they are formulated in a continuous framework and can achieve like this even subpixel accuracy. This is a big advantage compared to Markov random field approaches, which are based on discrete graph representations as for example in [43, 12]. We therefore formulate our proposed image registration methods in a variational framework. The first step in variational approaches is to define a suitable energy functional, which incorporates the desired constraints in the fidelity term and is regularised by a smoothness term. The minimisation of this energy functional should then lead to the optimal displacement field.

A common attempt for the minimisation of the energy functional is to derive the corresponding Euler-Lagrange equations and to finally solve them. However, since especially for image registration methods the energy func-

tional is normally non-convex, the Euler-Lagrange equations are in general not easy to solve. Frequently, the gradient descent method is applied [22, 84, 4, 5, 17] or a linearisation of the non-linear terms is performed [16, 4, 5, 17, 67, 92] to solve the equations. Brox *et al.* [16] for example developed a fixed point iteration scheme by linearising the resulting Euler-Lagrange equations. A similar scheme was then also used in the subsequent works [4, 5, 17].

For non-convex minimisation problems the risk of getting stuck in a local minimum is very high, despite linearisation. In image registration especially for large displacements, a coarse-to-fine strategy can be a remedy for this risk [11, 58, 16]. The idea is to build image pyramids by filtering and down-sampling the original images and to start the method at the coarsest level of these pyramids and successively evolving the intermediate results towards the finest level. See Fig. 1.6 for an illustration.

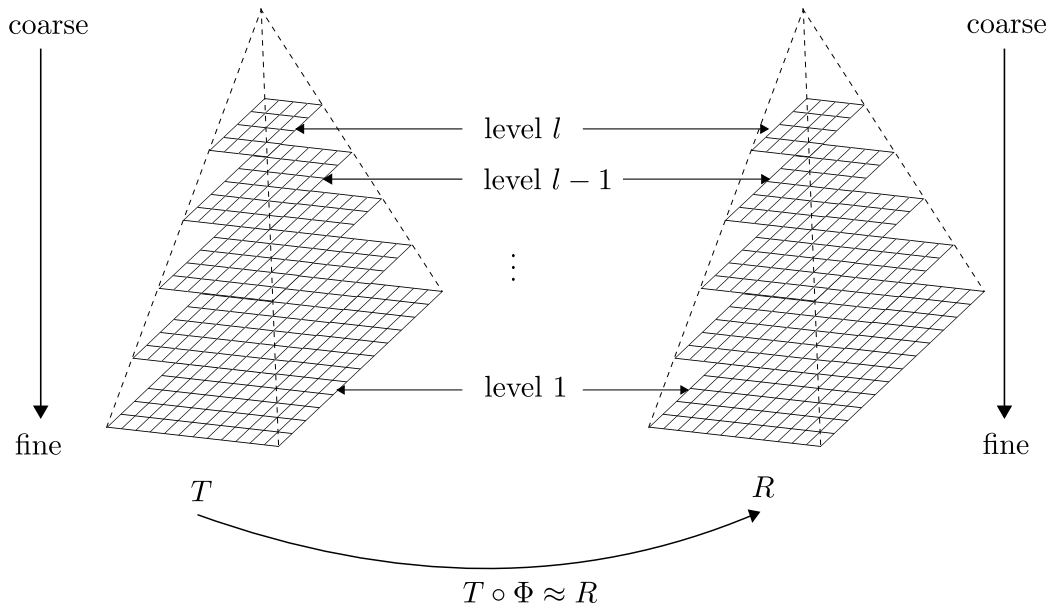


Figure 1.6: An illustration of the coarse-to-fine strategy.

Convex relaxation approaches became very popular in computer vision during the last few years [21, 13, 14]. Their aim is to reformulate the non-convex minimisation problem into a partly or fully convex one. The minimisation of this convexified problem leads then to a solution that is equal or close to the global minimiser of the original non-convex problem. In the following chapters we will make use of the convex relaxation approach of Chan *et al.* [21] (see Section 1.4) for the convex formulation of our energy functionals with respect to the motion segmentation function. Because of

the non-convexity of our energy functionals with respect to the displacement fields, our overall minimisation problems will remain, however, non-convex and are solved therefore in a coarse-to-fine strategy.

The minimisation of energy functionals that use the total variation (see Definition 1.1) for regularisation cannot be performed directly, because the total variation is not differentiable everywhere. Various approaches have been proposed to circumvent this difficulty. A widely used way is to use an approximation of the total variation [16, 4, 5] so that the Euler-Lagrange equations can be derived without any problems and solved appropriately. In Chapter 2 we will also use an approximation of the total variation for the displacement field and solve the resulting Euler-Lagrange equations similar as in [16, 4, 5] with the help of a fixed point iteration scheme. Another possibility to solve total variation based minimisation problems is to use the fast and easily implementable algorithm of Chambolle [19] as it was for example done in [67, 92]. We will use this method in Chapter 2 to minimise our energy functional there with respect to the motion segmentation function. The Split Bregman method, that was proposed by Goldstein and Osher [40], became also very popular for solving total variation based minimisation problems. Recently, Chambolle and Pock [20] proposed a primal-dual method to solve a certain class of minimisation problems, where most of them make use of the total variation. This method is closely related to the primal-dual method proposed by Esser *et al.* [27]. In their experiments, Chambolle and Pock [20] showed that they achieved faster convergence with their proposed method compared to other sophisticated methods, amongst others the Split Bregman method [40]. We will therefore use this promising primal-dual method in Chapters 3 and 4 to solve our minimisation problems there.

1.6 Landmarks

Landmark positions define the location of certain features in an image, as for example anatomically outstanding structures in medical images. One differs between the so called “hard” and “soft” landmarks [59], where hard landmarks are fiducial markers which are placed at certain positions on the patient before the image acquisition and soft landmarks are specified on the images themselves by a medical expert or sophisticated automatic detection tools. As mentioned in Section 1.1.3, landmark correspondences can be used for the validation of an image registration method and for rigid image registration methods there exists an error analysis based on fiducial points [33, 32].

Landmark correspondences in the images can also act as additional clues

for the estimation of the displacement field and prevent the image registration method to get stuck in a local minima during the optimisation procedure. Many image registration and optical flow methods exist that integrate the information of landmark correspondences to achieve a better estimation of the displacement field, as for example the works [42, 48, 53, 65, 18]. The recent work of Brox and Malik [18] explains how descriptor matchings, respectively landmark correspondences, can easily be included into a variational framework. We will make use of this idea in Chapter 4 to extend our work in Chapter 3. Instead of using a dense correspondence field, as it was done in [18], we use the landmarks extracted by the Affine Scale Invariant Feature Transform (A-SIFT) method [91]. This is a recently developed algorithm that extends the well known SIFT method [56] and allows landmark matching under affine deformations. Thus, it usually finds a lot more matches than the SIFT method. To get rid of possible false matches, the so obtained putative matches are then filtered by fitting a homography to the matches using RANSAC [31]. For a comparison, we visualise in Fig. 1.7 the landmark correspondences in MR images of the liver that were found by the SIFT method [56], the A-SIFT method [91] and the remaining A-SIFT matches after the filtering with RANSAC [31].

1.7 Outline and Contribution

In this thesis we propose different variational approaches for non-rigid image registration, which are able to preserve discontinuities in the displacement field through motion segmentation with the continuous cuts framework described in Section 1.4.

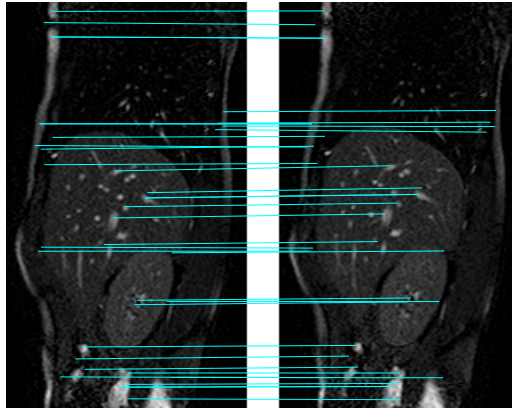
In Chapter 2, we propose a method that is based on the approach of Amiaz and Kiryati [4, 5] which was sketched in Section 1.3.3 before. Instead of using the level set representation for the motion segmentation we make use of the continuous cuts framework and are able to introduce a proposition that enables us to find a global minimiser for the motion segmentation for fixed displacement fields. Since the overall minimisation problem remains non-convex, we perform the minimisation procedure in a coarse-to-fine strategy. In contrast to the work of Amiaz and Kiryati [4, 5], we are able to use simple initialisation for the displacement fields and the motion segmentation without the need of any additional methods. Furthermore, the minimisation with respect to the displacement fields is performed similar as in [4, 5] respectively [16] through a fixed point iteration scheme and the one with respect to the motion segmentation through the fast dual method of Chambolle [19]. Experimental results are then shown for synthetic and real MR images of

breathing induced liver motion.

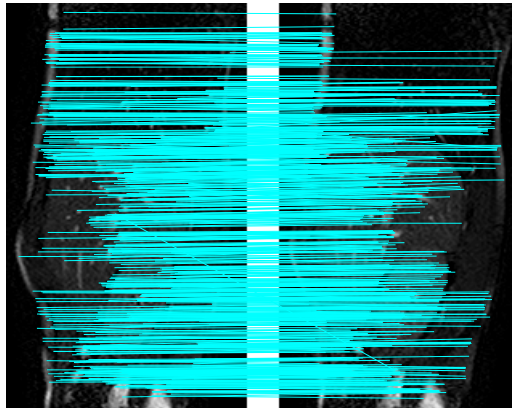
In Chapter 3, the pure L^1 -norm is used for the total variation of the displacement fields instead of using an approximation of it, as it was done in Chapter 2 before. Furthermore, the previous fidelity term is replaced by the sum of the absolute values of the similarity constraints. Like this, we fully remove the approximation function Ψ of the L^1 -norm, which was used in Chapter 2 and usually leads to a slow convergence for a small ϵ and to blurred results for large values of ϵ [67]. We show how this new complex minimisation problem can be solved by using the fast primal-dual method of Chambolle and Pock [20] to estimate both, the motion segmentation function and the displacement fields. We propose two variants on how to apply the primal-dual method for the minimisation of the energy functional with respect to the displacement fields. Finally, experimental results are shown for synthetic images and MR images with apparent breathing induced liver motion. Furthermore, we are able to show an improvement in the computational time compared to the previously proposed method in Chapter 2.

To support the image registration process to capture large displacements and to avoid unreliable estimations for the motion fields and the motion segmentation the inclusion of landmark correspondences is performed in Chapter 4. The landmark correspondences are established by using the Affine Scale Invariant Feature Transform (A-SIFT) method [91] followed by a RANSAC filtering [31]. The incorporation of the so gained landmark correspondences into the energy functional, that was proposed in Chapter 3, is then achieved similar as in the work of Brox and Malik [18]. Finally, we applied again the fast primal-dual method of Chambolle and Pock [20] for the minimisation of the energy functional with respect to both, the displacement fields and the motion segmentation as it was done in Chapter 3. For the minimisation of the displacement fields we used the proposed first variant in Chapter 3 to apply the primal-dual method. However, we could have also used the proposed second variant to apply the primal-dual method. Experimental results for MR images of breathing induced liver motion show that more reliable motion segmentation results can be found with the incorporation of the landmarks correspondences.

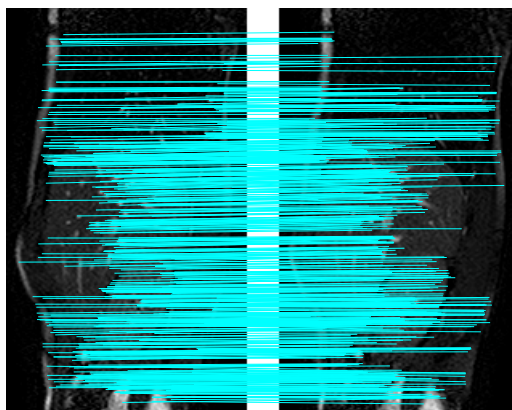
Finally, we discuss in Chapter 5 the results of this thesis and mention some interesting possibilities for future research.



(a) SIFT: 37 matches



(b) A-SIFT: 746 matches



(c) A-SIFT with RANSAC: 645 matches

Figure 1.7: The landmark correspondences found by SIFT (a), A-SIFT (b) and the remaining A-SIFT matches after applying RANSAC (c).

Chapter 2

Discontinuity Preserving Registration through Motion Segmentation with Continuous Cuts

The content of this chapter has been published in [49].

Discontinuous displacement fields are quite common in the medical field, in particular at organ boundaries with breathing induced organ motion. The sliding motion of the liver along the abdominal wall clearly causes a discontinuous displacement field. Today's common medical image registration methods, however, cannot properly deal with this kind of motion as their regularisation term enforces a smooth displacement field. Since these motion discontinuities appear at organ boundaries, motion segmentation could play an important guiding role during registration.

In this chapter we propose a novel method that integrates registration and globally optimal motion segmentation in a variational framework. The energy functional is formulated such that the segmentation, via continuous cuts [21], supports the computation of discontinuous displacement fields. The proposed energy functional is then minimised in a coarse-to-fine strategy by using a fast dual method for motion segmentation and a fixed point iteration scheme for motion estimation. Experimental results are shown for synthetic and real MR images of breathing induced liver motion.

2.1 Introduction

Image registration is an essential tool for many medical applications. Registration is a yet powerful but also very challenging task as it is generally an ill-posed problem. A good survey on the state-of-the-art in image registration can be found in [94]. Although today's image registration methods can handle rigid and non-rigid motion nicely, they have difficulties dealing with discontinuous motion fields. These discontinuities occur for example when organs, such as the liver, are sliding along the abdominal wall during the breathing cycle. Whereas the organs are moving mainly in superior-inferior direction, the abdominal wall is moving anterior-posteriorly. The regularisation constraints of the state-of-the-art registration methods, however, enforce a smooth displacement field along these discontinuities yielding inaccurate motion information.

Although the problem of discontinuities has been a topic of research in image segmentation and classical optical flow for some decades, its influence on medical image registration was neglected. Mumford and Shah for example introduced in their pioneering work [60] from 1989 a functional, that avoids spatial smoothing on a certain set of the image and therefore preserves the discontinuities there. Several methods were proposed to solve the Mumford and Shah minimisation problem. One such approach is the widely used method proposed by Vese and Chan [84]. They reformulated the Mumford-Shah functional in a level set framework to perform piecewise constant and piecewise smooth segmentation of an image. Another seminal approach, which is known to preserve discontinuities and is based on the total variation (TV), was proposed by Rudin *et al.* [71] for image denoising. The beneficial behaviour of the TV was also exploited in image registration and optical flow, see *e.g.* [67] and [16].

Recently, Schmidt-Richberg *et al.* [73] introduced a direction-dependent regularisation method to preserve discontinuities in the displacement field. This regularisation method, however, depends on the calculation of the normals at the object boundaries and therefore a rather good manual segmentation has to be provided in advance.

Since motion discontinuities appear in particular at object boundaries, motion segmentation can influence the registration process positively. More specifically, it is a chicken-and-egg problem. By providing a good motion segmentation, a proper discontinuous displacement field can be estimated and vice versa. In fact, motion estimation and motion segmentation can benefit from each other. One method that combines optical flow computation with motion segmentation was proposed by Amiaz and Kiryati [5]. They embedded the optical flow method of Brox *et al.* [16] into the level set

framework of Vese and Chan [84]. A drawback of the level set formulation is, that it is non-convex and therefore is fraught with the risk of getting stuck in local minima during optimisation of the energy functional.

In this chapter we propose a variational elastic registration approach able to properly handle discontinuities. To guarantee a globally optimal motion segmentation, we will make use of the approach of Chan *et al.* [21], also called “continuous cuts” in [37]. Instead of formulating a level set function, we define a binary function and extend it to a continuous function. The resulting minimisation problem then becomes convex with respect to this continuous function and the globally optimal motion segmentation is gained by a threshold, which can be interpreted as a cut. Although motion segmentation turns into a convex problem, motion estimation still remains a non-convex optimisation task and will be solved similar to [16] and [5] through fixed point iterations.

2.2 Method

In this section we describe the proposed registration method which integrates the accurate optical flow estimation of Brox *et al.* [16] into the convex segmentation method of Chan *et al.* [21], in order to find smooth displacement fields whilst preserving the discontinuities. The generalisation of the method from 2D to higher dimensional images is straightforward.

2.2.1 Registration and Motion Segmentation Framework

Optical Flow-based Registration

Let $\Omega \subset \mathbb{R}^2$ be the domain of the pixel positions $\vec{x} = (x_1, x_2)$. We then define by the functions $R : \Omega \rightarrow \mathbb{R}$ and $T : \Omega \rightarrow \mathbb{R}$ our reference and template image. The aim of image registration is to find a transformation $\Phi(\vec{x}) := \vec{x} + \vec{w}(\vec{x})$ such that the relation $T \circ \Phi \approx R$ holds. The function

$$\vec{w} : \begin{cases} \Omega \rightarrow \mathbb{R}^2 \\ \vec{x} \mapsto \vec{w}(\vec{x}) := (u(\vec{x}), v(\vec{x})) \end{cases},$$

with $u, v : \Omega \rightarrow \mathbb{R}$, describes the displacement field and will be the intrinsic function we investigate. For convenience we will use the abbreviations \vec{w} , u and v for $\vec{w}(\vec{x})$, $u(\vec{x})$ and $v(\vec{x})$.

To solve a non-rigid registration problem with expected discontinuities in the displacement field, we adopt the method proposed by Brox *et al.* [16], that has been proven to be highly accurate for optical flow estimation. They define the energy functional as

$$E_{Brox}(\vec{w}) = \int_{\Omega} f(\vec{w}) + \mu s(\vec{w}) d\vec{x}, \quad (2.1)$$

where $\mu \in \mathbb{R}^+$ is a weighting parameter, f and s are the fidelity term and the smoothness term, respectively, which are defined as

$$f(\vec{w}) = f(u, v) := \Psi \left(|T(\vec{x} + \vec{w}) - R(\vec{x})|^2 + \gamma |\nabla T(\vec{x} + \vec{w}) - \nabla R(\vec{x})|^2 \right) \text{ and} \\ s(\vec{w}) = s(u, v) := \Psi \left(|\nabla u|^2 + |\nabla v|^2 \right).$$

The function $\Psi(z^2) = \sqrt{z^2 + \epsilon^2}$, with $\epsilon \in \mathbb{R}^+$ small, results in an approximation of the L^1 -norm and it is robust against outliers. The fidelity term f incorporates the gradient constancy constraint to complement the grey value constancy constraint, which is weighted by a parameter $\gamma \in \mathbb{R}_0^+$.

Motion Segmentation

Now we would like to integrate the optical flow estimation into the convex segmentation model of Chan *et al.* in [21]. Instead of using the level set function $\phi : \Omega \rightarrow \mathbb{R}$ and the Heaviside function $H : \mathbb{R} \rightarrow \{0, 1\}$ to differentiate the displacement field \vec{w} into \vec{w}^+ and \vec{w}^- as proposed by Amiaz and Kiryati [5], we choose a binary function

$$\tilde{u} : \begin{cases} \mathbb{R}^2 \rightarrow \{0, 1\} \\ \vec{x} \mapsto \tilde{u}(\vec{x}) := \mathbf{1}_{\Sigma}(\vec{x}), \end{cases}$$

where $\Sigma \subseteq \Omega \subset \mathbb{R}^2$ with $\Sigma := \{\vec{x} \in \Omega \mid \tilde{u}(\vec{x}) = 1\}$. By defining $D(\vec{w}) := f(\vec{w}) + \mu s(\vec{w})$ as a data term, we formulate our energy functional as

$$E(\vec{w}^+, \vec{w}^-, \tilde{u}) = \int_{\Omega} D(\vec{w}^+) \tilde{u}(\vec{x}) d\vec{x} + \int_{\Omega} D(\vec{w}^-) (1 - \tilde{u}(\vec{x})) d\vec{x} \\ + \nu \int_{\Omega} |\nabla \tilde{u}(\vec{x})| d\vec{x}, \quad (2.2)$$

where the last term of the above energy is a regularisation defined by the TV, and $\nu \in \mathbb{R}^+$ is a weighting parameter to control the weighting of the

fidelity and smoothness term in D with respect to the TV of \tilde{u} . As pointed out by Chan *et al.* in [21], Eq. (2.2) is strongly related to the Mumford-Shah functional [60] and can be written as

$$\tilde{E}(\vec{w}^+, \vec{w}^-, \Sigma) = \int_{\Sigma} D(\vec{w}^+) d\vec{x} + \int_{\Omega \setminus \Sigma} D(\vec{w}^-) d\vec{x} + \nu \text{Per}(\Sigma, \Omega), \quad (2.3)$$

where $\text{Per}(\Sigma, \Omega)$ denotes the perimeter of the set $\Sigma \subseteq \Omega$. In order to find a global minimiser Σ_{\min} of $\tilde{E}(\vec{w}^+, \vec{w}^-, \cdot)$, we arrive at the proposition below.

Proposition 2.1. *For any fixed $\vec{w}^+, \vec{w}^- : \Omega \rightarrow \mathbb{R}^2$, a global minimiser for $\tilde{E}(\vec{w}^+, \vec{w}^-, \cdot)$ can be found by solving the convex problem*

$$\min_{0 \leq \tilde{u} \leq 1} E(\vec{w}^+, \vec{w}^-, \tilde{u})$$

and finally setting

$$\Sigma = \Sigma(\eta) := \{\vec{x} \in \Omega \mid \tilde{u}(\vec{x}) \geq \eta\} \text{ for almost every } \eta \text{ with } \eta \in [0, 1].$$

Proof. The proof can be carried out similarly to the one in [21] with the help of the layer cake representation and the coarea formula. (See also the proof of Theorem 1.4 in Section 1.4.2.) \square

Note, that the set of functions, over which minimisation is performed, is not restricted to binary functions \tilde{u} anymore. To achieve a convex problem the feasible set allows for functions that take values between 0 and 1. We refer the reader to [21] for further exploration. To this end, by having the globally optimal motion segmentation we obtain the final displacement field $\vec{w} := \vec{w}^+ \tilde{u} + \vec{w}^- (1 - \tilde{u})$.

To illustrate our method we show a synthetic example in Fig. 2.1. The motion segmentation function \tilde{u} splits the displacement field \vec{w} into the parts \vec{w}^+ and \vec{w}^- . The function \tilde{u} is close to a binary function, although we perform minimisation over non-binary functions. This property was also pointed out in [21].

2.2.2 Minimisation

To minimise our energy functional in Eq. (2.2) with respect to \tilde{u} in a fast and efficient way, we follow an approach similar to Pock *et al.* in [67], which allows us to exploit the powerful work of Chambolle [19]. We introduce a new variable \tilde{v} and consider the energy functional

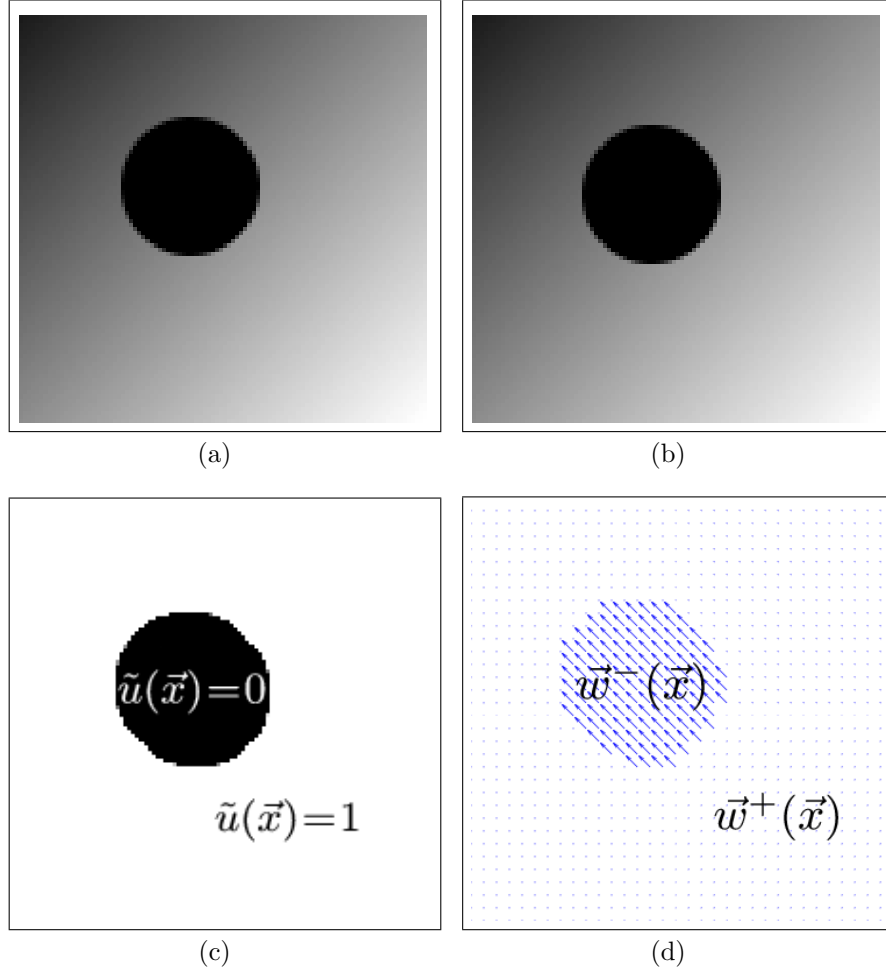


Figure 2.1: The template image (a), the reference image (b), the motion segmentation function \tilde{u} (c) and the displacement field \vec{w} (d).

$$\begin{aligned} \hat{E}(\vec{w}^+, \vec{w}^-, \tilde{u}, \tilde{v}) = & \nu \int_{\Omega} |\nabla \tilde{u}(\vec{x})| d\vec{x} + \frac{1}{2\theta} \int_{\Omega} (\tilde{u}(\vec{x}) - \tilde{v}(\vec{x}))^2 d\vec{x} \\ & + \int_{\Omega} D(\vec{w}^+) \tilde{v}(\vec{x}) d\vec{x} + \int_{\Omega} D(\vec{w}^-) (1 - \tilde{v}(\vec{x})) d\vec{x}. \end{aligned} \quad (2.4)$$

For a small $\theta \in \mathbb{R}^+$ the minimisation of Eq. (2.4) with respect to \tilde{u} and \tilde{v} leads to $\tilde{u} \approx \tilde{v}$ and therefore approximates the energy functional E in Eq. (2.2). We propose the following iterative scheme to minimise the energy functional \hat{E} with respect to \vec{w}^+ , \vec{w}^- , \tilde{u} and \tilde{v} :

1. For fixed \tilde{v} , solve

$$\min_{\tilde{u}} \left\{ \int_{\Omega} |\nabla \tilde{u}(\vec{x})| d\vec{x} + \frac{1}{2\theta\nu} \int_{\Omega} (\tilde{u}(\vec{x}) - \tilde{v}(\vec{x}))^2 d\vec{x} \right\}. \quad (2.5)$$

2. For fixed \tilde{v} , solve

$$\min_{\vec{w}^+} \left\{ \int_{\Omega} D(\vec{w}^+) \tilde{v}(\vec{x}) d\vec{x} \right\}. \quad (2.6)$$

3. For fixed \tilde{v} , solve

$$\min_{\vec{w}^-} \left\{ \int_{\Omega} D(\vec{w}^-) (1 - \tilde{v}(\vec{x})) d\vec{x} \right\}. \quad (2.7)$$

4. For fixed \vec{w}^+ , \vec{w}^- and \tilde{u} , solve

$$\min_{\tilde{v} \in [0,1]} \left\{ \frac{1}{2\theta} \int_{\Omega} (\tilde{u}(\vec{x}) - \tilde{v}(\vec{x}))^2 d\vec{x} + \int_{\Omega} D(\vec{w}^+) \tilde{v}(\vec{x}) d\vec{x} + \int_{\Omega} D(\vec{w}^-) (1 - \tilde{v}(\vec{x})) d\vec{x} \right\}. \quad (2.8)$$

The minimisation problem Eq. (2.5) is basically the denoising problem of the Rudin, Osher and Fatemi (ROF) model [71], and can be solved by the fast dual method of Chambolle [19]. The resulting Euler-Lagrange equations for Eq. (2.6) and Eq. (2.7) are similar to the ones in [5], and can be solved by the fixed point iteration scheme as described there. For the minimisation problem Eq. (2.8), the explicit solution can be derived from the corresponding Euler-Lagrange equation and is given by

$$\tilde{v}(\vec{x}) = \min \left\{ \max \left\{ \tilde{u}(\vec{x}) - \theta (D(\vec{w}^+) - D(\vec{w}^-)), 0 \right\}, 1 \right\}. \quad (2.9)$$

2.2.3 Implementation

Although, we have a convex minimisation problem with respect to the functions \tilde{u} and \tilde{v} , the ones with respect to the displacement fields w^+ and w^- are still non-convex. To avoid the risk of getting stuck in a local minimum during the optimisation of the displacement fields, we wrap the iterative minimisation procedure in a coarse-to-fine framework. By choosing a minimal size n_{min} of the images at the coarsest level, we calculate the number of levels with the help of a certain scaling factor ξ . In our experiments we set $n_{min} = 32$ and $\xi = 0.9$. The coarse-to-fine strategy has also the advantage, that we

can use trivial initialisations for the displacement fields. In contrary, Amiaz and Kiryati [5] had to use additional methods to initialise the displacement fields. At the coarsest level we therefore initialise the displacement fields \vec{w}^+ and \vec{w}^- with $\vec{0}$.

Because of Proposition 2.1 the choice of the initialisation for the function \tilde{u} should be irrelevant for fixed \vec{w}^+ and \vec{w}^- . Whatever initialisation we choose, a global minimiser will be obtained when \vec{w}^+ and \vec{w}^- are fixed. Although we are updating the displacement fields \vec{w}^+ and \vec{w}^- regularly during the optimisation procedure, a similar property has been also exploited during the experiments by choosing a random initialisation for \tilde{u} . Again, this is a great advantage of our method in contrast to the one in [5], where the initialisation for the level set function ϕ was also dependent on additional methods.

Our final iteration scheme consist of two loops. The outer loop iterates over the pyramid levels. In each level an inner loop updates the values for \tilde{u} , \vec{w}^+ , \vec{w}^- and \tilde{v} , following steps 1 - 4 in Section 2.2.2. Thus, in each iteration of this inner loop one step of Chambolle's method [19] is performed to update \tilde{u} . To achieve a better convergence of \tilde{u} we update \vec{w}^+ and \vec{w}^- only each 10th iteration by executing one step of the inner fixed point iteration as described in [16] and [5]. To obtain the motion segmentation Σ we choose $\eta = 0.5$ and set $\Sigma = \Sigma(\eta) := \{\vec{x} \in \Omega \mid \tilde{u}(\vec{x}) \geq \eta\}$ (see Proposition 2.1). Finally, \tilde{v} is updated according to the explicit solution given in Eq. (2.9).

As soon as the finest level is reached, the inner loop is executed until a certain tolerance or the maximum number of iterations is reached. The final displacement field is then obtained by setting

$$\vec{w}(\vec{x}) = \begin{cases} \vec{w}^+(\vec{x}) & \text{if } \vec{x} \in \Sigma, \\ \vec{w}^-(\vec{x}) & \text{if } \vec{x} \in \Omega \setminus \Sigma, \end{cases}$$

and we use bicubic interpolation to calculate the images $T(\vec{x} + \vec{w}^\pm)$ during the iterations and to obtain the final registered image $T(\vec{x} + \vec{w})$.

2.3 Results

In this section we give a qualitative and quantitative evaluation of the proposed method on MR images of the liver, where the liver is sliding along the chest wall. In particular we compare our method to the demon algorithm with anisotropic diffusion filtering [26] and the registration algorithm of Brox *et al.* [16], which are known to preserve discontinuities in the displacement field.

In Fig. 2.2 a qualitative result is given comparing the various methods. One can clearly see, that a discontinuous motion field is achieved by our method and compared to the demon algorithm with anisotropic diffusion filtering and the registration algorithm of Brox *et al.* these discontinuities are more defined. The proposed approach managed to nicely separate the motion of the abdominal wall and the motion of the internal organs.

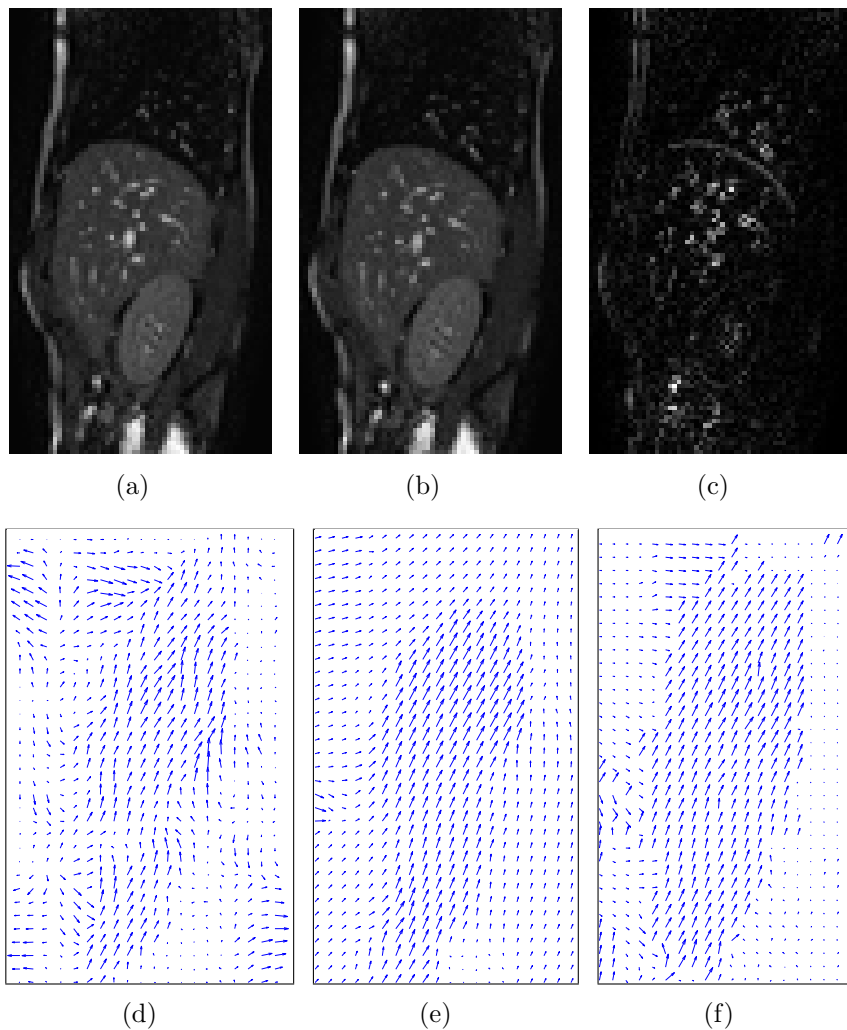


Figure 2.2: The template image (a), the reference image (b) and the difference image (c). The displacement field for the demon algorithm with anisotropic diffusion filtering is shown in (d), the one for the registration algorithm of Brox *et al.* in (e) and finally the one of our method in (f).

In Fig. 2.3 a quantitative evaluation is shown for 22 different liver image pairs. We chose the parameters for all the three methods by optimising them

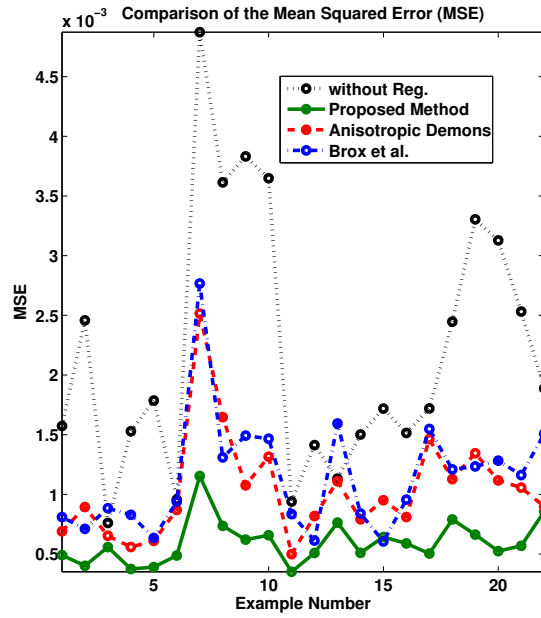
with respect to these image pairs. The parameters of our method were set to $\gamma = 0.4$, $\mu = 0.05$, $\nu = 20$, $\theta = 0.2$ and $\epsilon = 0.00001$. For the demon algorithm with anisotropic diffusion filtering we could use the suggested parameters and for Brox *et al.*'s method we used $\gamma = 5$, $\alpha = 80$ and $\sigma = 0.9$. The registration results were compared by calculating the mean squared error (MSE) and the normalised mutual information (NMI), where the grey values were scaled from 0 to 1. For all examples the proposed method performed better than the demon algorithm with anisotropic diffusion filtering. Compared to the method of Brox *et al.*, our approach provided better results except for the mean squared error in example 15.

Using the R software package (Version 2.10.1), we used the Kolmogorov-Smirnov test to check the normal distribution of the results. Assuming a significance level of 0.05, the t-tests showed that the proposed method performed significantly better than the demon algorithm with anisotropic diffusion filtering and the method of Brox *et al.* for MSE and NMI with both $p < 0.05$.

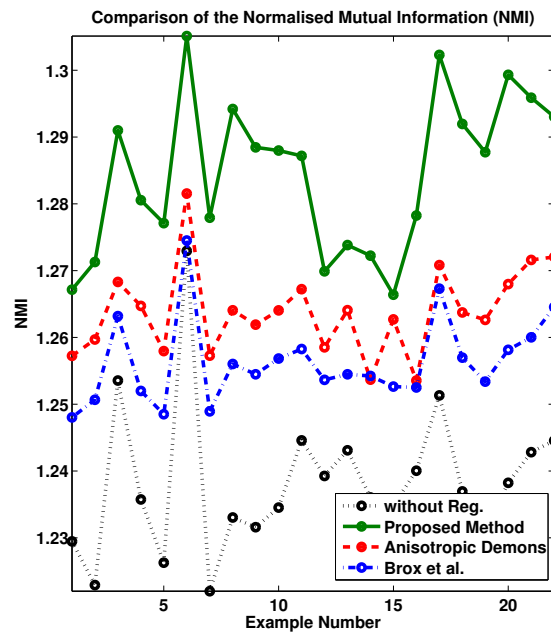
2.4 Conclusion

In this chapter we presented a novel discontinuity preserving non-rigid registration method, which uses the advantage of the continuous cuts framework. We introduced a Proposition, which shows that a globally optimal motion segmentation can be found for fixed displacement fields \vec{w}^+ and \vec{w}^- . During motion estimation the so gained motion segmentation plays an aiding role. The minimisation of the energy functional is implemented in a coarse-to-fine strategy and exploits the rapidity of the dual method of Chambolle [19] and the accuracy of Brox *et al.*'s optical flow method. Our experimental results demonstrated desirable performance of the proposed method in comparison with those of the demon algorithm with anisotropic diffusion filtering and the registration algorithm of Brox *et al.*

Currently, we are working on a fast primal-dual method [20] based on the pure L^1 -norm to improve the efficiency and accuracy of the method. We also plan to investigate the use of multi-label functions \tilde{u} in order to capture more complex piecewise smooth displacement fields.



(a)



(b)

Figure 2.3: Quantitative evaluation for 22 pairs of liver images with a discontinuous displacement field. Comparison of the MSE (a) and NMI (b).

Chapter 3

A Primal-Dual Approach for Discontinuity Preserving Registration through Motion Segmentation with Continuous Cuts

The content of this chapter has been submitted to a journal [50]. A preliminary version has been published in [52].

Image registration is a powerful tool in medical image analysis and facilitates the clinical routine in several aspects. There are many well established elastic registration methods, but none of them can so far preserve discontinuities in the displacement field. These discontinuities appear in particular at organ boundaries during the breathing induced organ motion.

In this chapter we exploit again the fact, that motion segmentation could play a guiding role during discontinuity preserving registration. The motion segmentation is embedded like before in a continuous cut framework [21]. This time the pure L^1 -norm is used for the smoothness term and the fidelity term is replaced by the sum of the absolute values of the similarity constraints. We show that a primal-dual method can be used to estimate a solution to this challenging variational problem and that like this an improvement in the computational time can be achieved. Experimental results are presented for artificial as well as MR Images with apparent breathing induced sliding motion of the liver along the abdominal wall.

3.1 Introduction

Image registration became an indispensable tool for many medical applications including the image-guided therapy systems. Today’s image registration methods [94] are powerful at handling rigid as well as non-rigid motion on mono- and multi-modal images. With the introduction of imaging technologies capable of capturing 4D organ motion, such as 4D-MRI [85], 4D-CT or 4D-Ultrasound, imagery of sliding organs became a significant focus of research. Most of the state-of-the-art image registration methods cannot yet properly deal with these data sets, as their regularisations cause continuous motion fields over the organ boundaries.

In recent publications, the concept of the direction-dependent regularisation of the displacement field, has been introduced *e.g.* [73]. The drawback of these methods is the necessity of providing a good manual segmentation of the boundaries. Approaches that don’t rely on prior manual segmentations have been a topic of research for some decades in classical computer vision such as optical flow. Transfer of these research results into the medical field was, however, scarce. Already in 1989, Mumford and Shah [60] proposed in their pioneering work a functional for image segmentation that avoids spatial smoothing in certain locations of the image, thus preserving discontinuities. Some years later, Weickert and Schnörr [88] proposed an extension of non-quadratic variational regularisation for discontinuities preserving optical flow that uses spatio-temporal regularisers instead of flow-driven spatial smoothness. The resulting convex function guaranteed global convergence that could be solved with standard gradient based optimisation schemes. Vese and Chan [84] then introduced a level set framework based approach to efficiently solve the Mumford and Shah minimisation problem for segmentation. Another influential approach based on the total variation (TV), known to preserve discontinuities, was proposed by Rudin, Osher and Fatemi [71], the ROF-model. The beneficial behaviour of the TV was also exploited in recent registration and optical flow methods, as for example by [16] and [67].

Motion segmentation has been a topic of research for quite some time. In 1993, Nesi [62] proposed a variational optical flow approach that incorporates a variable for the presence of discontinuities and leads to a piecewise smooth motion estimation. Cremers and Schnörr introduced in [23] a variational approach seamlessly integrating motion segmentation and shape regularisation into one single energy functional. In [24] the authors formulated the motion segmentation problem in a Bayesian inference framework. Whereas the motion discontinuity could be represented either as an explicit spline function or by an implicit level set formulation allowing for an arbitrary number of objects to segment. As motion discontinuities mainly appear at object

boundaries, it seems natural to combine motion segmentation and registration. Given a good motion segmentation, a proper discontinuous motion field can be estimated and vice versa. Amiaz and Kiryati [5] tried to leverage this property by combining motion segmentation with the optical flow method of Brox *et al.* [16] in a level set framework. They showed that motion segmentation lead to better discontinuities in the motion field. However, their approach highly depends on the initialisation for the motion segmentation and displacement field. Furthermore, the level set approach is prone to local minima and a rather good initialisation has to be provided in advance.

In this chapter we propose an elastic registration approach that handles discontinuities in the motion field by combining motion segmentation and registration in a variational scheme. For motion segmentation we make use of the so called “continuous cuts” [21, 37] scheme that guarantees a globally optimal solution for a fixed motion field. In contrast to our previous work [49], which was outlined in Chapter 2, the proposed energy functional is this time TV- L^1 regularised for both the motion segmentation and the displacement field and the fidelity term is formulated as a sum of absolute values of the constraints. Minimising the TV- L^1 regularised functionals is, however, inherently difficult due to the non-smoothness of the TV. This is an active field of research, such as [20, 40, 54, 77] and the references therein, which are mainly based on operator splitting methods in convex analysis that split energy functionals into the non-linear and linear terms. In this chapter we show how to solve the proposed complex energy functional with the primal-dual method of Chambolle and Pock [20], which is very efficient for a wide class of non-smooth problems.

3.2 Registration and Motion Segmentation Framework

In this section we describe the proposed registration method which integrates the displacement field estimation into the convex segmentation method of Chan *et al.* [21], in order to find smooth displacement fields whilst preserving the discontinuities.

3.2.1 Registration

Let $\Omega \subset \mathbb{R}^2$ be the domain of the pixel positions $\vec{x} = (x_1, x_2)$. We then define by the functions $R : \Omega \rightarrow \mathbb{R}$ and $T : \Omega \rightarrow \mathbb{R}$ our reference and template image. The aim of image registration is to find a transformation

$\Phi(\vec{x}) := \vec{x} + \vec{w}(\vec{x})$ such that the relation $T \circ \Phi \approx R$ holds. The function

$$\vec{w} : \begin{cases} \Omega \rightarrow \mathbb{R}^2 \\ \vec{x} \mapsto \vec{w}(\vec{x}) := (u(\vec{x}), v(\vec{x})) \end{cases},$$

with $u, v : \Omega \rightarrow \mathbb{R}$, describes the displacement field and will be the intrinsic function we investigate. For convenience we will use the abbreviations \vec{w} , u and v for $\vec{w}(\vec{x})$, $u(\vec{x})$ and $v(\vec{x})$.

To solve a non-rigid registration problem with expected discontinuities in the displacement field, we want to follow a variational approach and we therefore first consider the energy functional

$$E_{fs}(\vec{w}) = \int_{\Omega} f(\vec{w}) + \mu s(\vec{w}) d\vec{x}, \quad (3.1)$$

where $\mu \in \mathbb{R}^+$ is a weighting parameter, f and s are the fidelity term and the smoothness term, respectively, which are defined as

$$\begin{aligned} f(\vec{w}) = f(u, v) := & \gamma_1 |T(\vec{x} + \vec{w}) - R(\vec{x})| \\ & + \gamma_2 |\partial_{x_1} T(\vec{x} + \vec{w}) - \partial_{x_1} R(\vec{x})| \\ & + \gamma_2 |\partial_{x_2} T(\vec{x} + \vec{w}) - \partial_{x_2} R(\vec{x})| \end{aligned} \quad (3.2)$$

and

$$s(\vec{w}) = s(u, v) := \sqrt{|\nabla u|^2 + |\nabla v|^2} = |\nabla \vec{w}|. \quad (3.3)$$

The fidelity term f incorporates the constraints for the grey value constancy and the gradient constancy and the corresponding weighting parameters are given by $\gamma_1, \gamma_2 \in \mathbb{R}_0^+$. The smoothness term s results in the L^1 -norm respectively the vectorial TV of \vec{w} .

The energy functional E_{fs} is motivated by the energy functional proposed by Brox *et al.* [16]. Instead of using the approximation function Ψ for the L^1 -norm, here the pure L^1 -norm is used for the smoothness term s and for the fidelity term f the sum of the absolute grey value difference and the componentwise absolute gradient differences is taken.

3.2.2 Motion Segmentation

Now we would like to integrate the formulation of the energy functional above into the convex segmentation model of Chan *et al.* [21]. To differentiate the displacement field \vec{w} into \vec{w}^+ and \vec{w}^- , we therefore choose a binary function

$$\tilde{u} : \begin{cases} \mathbb{R}^2 \rightarrow \{0, 1\} \\ \vec{x} \mapsto \tilde{u}(\vec{x}) := \mathbf{1}_{\Sigma}(\vec{x}), \end{cases}$$

where $\Sigma \subseteq \Omega \subset \mathbb{R}^2$ with $\Sigma := \{\vec{x} \in \Omega \mid \tilde{u}(\vec{x}) = 1\}$. By defining $D(\vec{w}) := f(\vec{w}) + \mu s(\vec{w})$ as a data term, we formulate our energy functional as

$$\begin{aligned} E(\vec{w}^+, \vec{w}^-, \tilde{u}) &= \int_{\Omega} D(\vec{w}^+) \tilde{u}(\vec{x}) \, d\vec{x} + \int_{\Omega} D(\vec{w}^-) (1 - \tilde{u}(\vec{x})) \, d\vec{x} \\ &\quad + \nu \int_{\Omega} |\nabla \tilde{u}(\vec{x})| \, d\vec{x}, \end{aligned} \quad (3.4)$$

where the last term of the above energy is a regularisation defined by the TV, and $\nu \in \mathbb{R}^+$ is a constant parameter.

The energy functional E Eq. (3.4) is very much related to the energy functional proposed by Amiaz and Kiryati [5]. Instead of applying the Heaviside function to a level set function, the binary function \tilde{u} is used here. Furthermore the approximation function Ψ for the L^1 -norm, which was used in [5], is omitted here. Instead the pure L^1 -norm is used for the smoothness terms $s(\vec{w}^{\pm})$ Eq. (3.3) and the fidelity terms $f(\vec{w}^{\pm})$ are replaced by a sum of absolute values of the constraints Eq. (3.2).

As pointed out by Chan *et al.* in [21], Eq. (3.4) is strongly related to the Mumford-Shah functional [60] and can be written as

$$\tilde{E}(\vec{w}^+, \vec{w}^-, \Sigma) = \int_{\Sigma} D(\vec{w}^+) \, d\vec{x} + \int_{\Omega \setminus \Sigma} D(\vec{w}^-) \, d\vec{x} + \nu \text{Per}(\Sigma, \Omega), \quad (3.5)$$

where $\text{Per}(\Sigma, \Omega)$ denotes the perimeter of the set $\Sigma \subseteq \Omega$.

Remark 3.1. One can show, that a global minimiser Σ_{min} of $\tilde{E}(\vec{w}^+, \vec{w}^-, \cdot)$ can be found by solving the convexified problem $\min_{0 \leq \tilde{u} \leq 1} E(\vec{w}^+, \vec{w}^-, \tilde{u})$ and finally setting $\Sigma = \Sigma(\eta) := \{\vec{x} \in \Omega \mid \tilde{u}(\vec{x}) \geq \eta\}$ for almost every η with $\eta \in [0, 1]$. (See also Proposition 1 in [49] respectively Proposition 2.1 in Chapter 2 and Theorem 1.4 in Section 1.4.2.) In fact, this holds for any data terms $D(\vec{w}^+)$ and $D(\vec{w}^-)$ that are measurable.

Finally, we obtain the aimed displacement field by setting $\vec{w} := \vec{w}^+ \tilde{u} + \vec{w}^- (1 - \tilde{u})$.

At this point, we would like to refer again to Fig. 2.1 in Chapter 2, where the principle of the motion segmentation is illustrated by an example.

3.3 Minimisation

3.3.1 Iterative Scheme

To facilitate the minimisation procedure we replace the fidelity term f in Eq. (3.2) by its partly linearised version

$$f(\vec{w}) = \gamma_1 |\rho_1(\vec{w})| + \gamma_2 |\rho_2^{(1)}(\vec{w})| + \gamma_2 |\rho_2^{(2)}(\vec{w})|, \quad (3.6)$$

where

$$\rho_1(\vec{w}) = \rho_1(\vec{x}, \vec{w}_0, \vec{w}) := T(\vec{x} + \vec{w}_0) + \nabla T(\vec{x} + \vec{w}_0)^\top (\vec{w} - \vec{w}_0) - R(\vec{x}), \quad (3.7)$$

$$\begin{aligned} \rho_2^{(1)}(\vec{w}) &= \rho_2^{(1)}(\vec{x}, \vec{w}_0, \vec{w}) \\ &:= \partial_{x_1} T(\vec{x} + \vec{w}_0) + \left(\begin{array}{c} \partial_{x_1 x_1} T(\vec{x} + \vec{w}_0) \\ \partial_{x_2 x_1} T(\vec{x} + \vec{w}_0) \end{array} \right)^\top (\vec{w} - \vec{w}_0) - \partial_{x_1} R(\vec{x}), \end{aligned} \quad (3.8)$$

and

$$\begin{aligned} \rho_2^{(2)}(\vec{w}) &= \rho_2^{(2)}(\vec{x}, \vec{w}_0, \vec{w}) \\ &:= \partial_{x_2} T(\vec{x} + \vec{w}_0) + \left(\begin{array}{c} \partial_{x_1 x_2} T(\vec{x} + \vec{w}_0) \\ \partial_{x_2 x_2} T(\vec{x} + \vec{w}_0) \end{array} \right)^\top (\vec{w} - \vec{w}_0) - \partial_{x_2} R(\vec{x}), \end{aligned} \quad (3.9)$$

with \vec{w}_0 fixed.

The minimisation of the energy functional E Eq. (3.4) with respect to \vec{w}^+ , \vec{w}^- and \tilde{u} is then performed by the following iterative scheme:

1. For fixed \vec{w}^+ and \vec{w}^- , solve

$$\begin{aligned} \min_{\tilde{u} \in [0,1]} \left\{ \int_{\Omega} D(\vec{w}^+) \tilde{u}(\vec{x}) d\vec{x} + \int_{\Omega} D(\vec{w}^-) (1 - \tilde{u}(\vec{x})) d\vec{x} \right. \\ \left. + \nu \int_{\Omega} |\nabla \tilde{u}(\vec{x})| d\vec{x} \right\}. \end{aligned} \quad (3.10)$$

2. For fixed \tilde{u} , solve

$$\min_{\vec{w}^+} \left\{ \int_{\Omega} D(\vec{w}^+) \tilde{u}(\vec{x}) d\vec{x} \right\}. \quad (3.11)$$

3. For fixed \tilde{u} , solve

$$\min_{\vec{w}^-} \left\{ \int_{\Omega} D(\vec{w}^-) (1 - \tilde{u}(\vec{x})) d\vec{x} \right\}. \quad (3.12)$$

Although problem Eq. (3.10) is convex, it is important to note that the overall minimisation of the energy functional E Eq. (3.4) is a non-convex optimisation problem. For the minimisation of non-convex energy functionals there exist convex relaxation methods, which are able to provide solutions close to a global minimum. Recently, Strekalovskiy *et al.* [80] proposed such a method for non-convex vector-valued labeling problems. In this chapter, however, we won't make use of these kind of methods.

Note that compared to our previous work [49] (see Chapter 2), this time we do not introduce an auxiliary \tilde{v} in the energy functional. Therefore our iterative scheme consist of only 3 steps instead of 4. The reason for this change is, that we intend to use a different numerical approach to solve our problem. More precisely, to solve the subproblems Eq. (3.10), Eq. (3.11) and Eq. (3.12) in a fast and efficient way, we follow a primal-dual approach as described by Chambolle and Pock in [20]. We therefore recapitulate in the next section the basic notations and formulations.

3.3.2 Basic Framework for the Primal-Dual Approach of Chambolle and Pock

First, we define by X and Y two finite-dimensional real vector spaces. Their inner products are denoted by $\langle \cdot, \cdot \rangle_X$ respectively $\langle \cdot, \cdot \rangle_Y$ and their induced norms are given by $\|\cdot\|_X = \sqrt{\langle \cdot, \cdot \rangle_X}$ respectively $\|\cdot\|_Y = \sqrt{\langle \cdot, \cdot \rangle_Y}$. The general non-linear primal problem we consider is of the form

$$\min_{x \in X} F(Kx) + G(x), \quad (3.13)$$

where $F : Y \rightarrow [0, +\infty)$ and $G : X \rightarrow [0, +\infty)$ are proper, convex and lower semi-continuous and the map $K : X \rightarrow Y$ is a continuous linear operator. The corresponding primal-dual formulation of Eq. (3.13) is the saddle-point problem

$$\min_{x \in X} \max_{y \in Y} \langle Kx, y \rangle_Y + G(x) - F^*(y), \quad (3.14)$$

with $F^* : Y \rightarrow \mathbb{R} \cup \{+\infty\}$ being the convex conjugate of F . We assume that the problems above have at least one solution $(\hat{x}, \hat{y}) \in X \times Y$ and therefore it holds

$$\begin{aligned} K\hat{x} &\in \partial F^*(\hat{y}), \\ -(K^*\hat{y}) &\in \partial G(\hat{x}), \end{aligned}$$

where $\partial F^*(\hat{y})$ and $\partial G(\hat{x})$ are the subdifferentials of the convex functions F^* at \hat{y} and G at \hat{x} . Furthermore we assume that F and G are “simple”, *i.e.*

that the resolvent operators $(I + \sigma \partial F^*)^{-1}$ and $(I + \tau \partial G)^{-1}$, with $\sigma, \tau \in \mathbb{R}^+$ small enough, are easy to compute. For a convex function f the resolvent of the operator $\tau \partial f$ at \tilde{x} can be calculated in our case by

$$x = (I + \tau \partial f)^{-1}(\tilde{x}) = \arg \min_x \left\{ \frac{\|x - \tilde{x}\|^2}{2\tau} + f(x) \right\}. \quad (3.15)$$

In this chapter we will only make use of Algorithm 1 in [20] with the extrapolation parameter $\theta = 1$. Although interesting, the usage of the other proposed algorithms is left for the moment for later research.

To apply Algorithm 1 in [20] to the minimisation problems Eq. (3.10), Eq. (3.11) and Eq. (3.12), we first need to rewrite them in their discretised version, then identify the functions F and G and finally derive the resolvent operators $(I + \sigma \partial F^*)^{-1}$ and $(I + \tau \partial G)^{-1}$.

For the discrete setting we therefore define by

$$\vec{x}_{i,j} = (x_{1i,j}, x_{2i,j}) = (ih, jh), \quad i = 1, \dots, M, j = 1, \dots, N,$$

the pixel positions in the image domain with h being the spatial step size. For the calculations of the finite differences, the discrete divergence operator, the discretised inner products and further details we refer the reader to [20] and the references therein.

In the following section we will derive the resolvent operators for the three given minimisation problems Eq. (3.10), Eq. (3.11) and Eq. (3.12).

3.4 Derivation of the Resolvent Operators

3.4.1 Resolvent Operators for Problem Eq. (3.10)

Let us consider the continuous problem Eq. (3.10). As mentioned already before, we need to rewrite the problem in its discretised version to be able to apply a primal-dual approach for the minimisation. We use the spaces $X = \mathbb{R}^{MN}$ and $Y = X \times X$ and their inner products

$$\langle s, t \rangle_X = \sum_{i,j} s_{i,j} t_{i,j}, \quad s, t \in X \quad \text{and} \quad (3.16)$$

$$\langle p, q \rangle_Y = \sum_{i,j} p_{i,j}^{(1)} q_{i,j}^{(1)} + p_{i,j}^{(2)} q_{i,j}^{(2)},$$

$$p = (p^{(1)}, p^{(2)}), \quad q = (q^{(1)}, q^{(2)}) \in Y. \quad (3.17)$$

Using the rectangle rule we can rewrite problem Eq. (3.10) in the discretised version

$$h^2 \min_{\tilde{u} \in [0,1]^{MN}} \left\{ \nu \|\nabla \tilde{u}\|_1 + \sum_{i,j} \left(D(\vec{w}_{i,j}^+) \tilde{u}_{i,j} + D(\vec{w}_{i,j}^-) (1 - \tilde{u}_{i,j}) \right) \right\}, \quad (3.18)$$

where the factor h^2 can be neglected, since it has no influence on the optimal solution. The semi-norm $\|\nabla s\|_1$, with $s \in X$, is defined by $\|\nabla s\|_1 = \sum_{i,j} |(\nabla s)_{i,j}|$, where $|(\nabla s)_{i,j}| = \sqrt{((\nabla s)_{i,j}^{(1)})^2 + ((\nabla s)_{i,j}^{(2)})^2}$.

Comparing Eq. (3.18) to Eq. (3.13), we see that $K = \nabla$, $F(\nabla \tilde{u}) = \nu \|\nabla \tilde{u}\|_1$ and $G(\tilde{u}) = \sum_{i,j} D(\vec{w}_{i,j}^+) \tilde{u}_{i,j} + D(\vec{w}_{i,j}^-) (1 - \tilde{u}_{i,j})$. The solution of the resolvent operator with respect to F^* can be derived as

$$p = (I + \sigma \partial F^*)^{-1}(\tilde{p}) \implies p_{i,j} = \nu \frac{\tilde{p}_{i,j}}{\max\{\nu, |\tilde{p}_{i,j}|\}},$$

and the one with respect to G as

$$\tilde{u} = (I + \tau \partial G)^{-1}(\hat{u}) \implies \tilde{u}_{i,j} = \min\{\max\{\hat{u}_{i,j} - \tau (D(\vec{w}_{i,j}^+) - D(\vec{w}_{i,j}^-)), 0\}, 1\}.$$

Remark 3.2. The primal-dual formulation of problem Eq. (3.18) is a special case of the general problem considered in Pock *et al.*'s work [66] and the resulting primal-dual algorithm is then the same as described there. Namely, the dual variable p is projected onto the convex set, a disc with radius ν , and with a truncation of the primal variable \tilde{u} the projection on the feasible convex set $[0, 1]$ is achieved.

Remark 3.3. The observant readers probably noticed, that we slightly misused the mathematical notation to make the formulas more pleasing to the eye. More precisely, instead of writing $D(\vec{w}_{i,j}^\pm)$ we should have been using $D(\vec{w}^\pm)|_{i,j}$, since discretisation is performed after the function D is applied. In the following we will also make use of this sloppy notation for the functions ρ_1 , $\rho_2^{(1)}$ and $\rho_2^{(2)}$ given in Eq. (3.7), Eq. (3.8) and Eq. (3.9).

3.4.2 Resolvent Operators for Problem Eq. (3.11)

Now we consider the continuous problem Eq. (3.11). If we have a closer look at this minimisation problem, we see that we only receive information about \vec{w}^+ on the domain Σ where \tilde{u} will be set to 1. Although theoretically reasonable, for the numerical calculations the implementation gets facilitated

by having a smooth extension of \bar{w}^+ to the domain $\Omega \setminus \Sigma$. We therefore consider instead the problem

$$\min_{\bar{w}^+} \left\{ \int_{\Omega} f(\bar{w}^+) \tilde{u}(\bar{x}) + \mu s(\bar{w}^+) d\bar{x} \right\}. \quad (3.19)$$

Comparing Eq. (3.11) to Eq. (3.19) the only difference is, that the factor \tilde{u} is not applied to the smoothness term s anymore.

For the primal-dual approach we will consider two different variants, in the following referred to as **VARIANT I** and **VARIANT II**. We will use the spaces $X = \mathbb{R}^{MN} \times \mathbb{R}^{MN}$ and $Y = Y_1 = X \times X$ (for **VARIANT I**) respectively $Y = Y_2 = Y_1 \times \mathbb{R}^{MN} \times \mathbb{R}^{MN} = (\mathbb{R}^{MN})^6$ (for **VARIANT II**). The inner product of X is the same as in Eq. (3.17) and the one for Y_1 and Y_2 are defined by

$$\begin{aligned} \langle p, q \rangle_{Y_1} &= \sum_{i,j} p_{i,j}^{(1)} q_{i,j}^{(1)} + p_{i,j}^{(2)} q_{i,j}^{(2)} + p_{i,j}^{(3)} q_{i,j}^{(3)} + p_{i,j}^{(4)} q_{i,j}^{(4)}, \\ p &= (p^{(1)}, p^{(2)}, p^{(3)}, p^{(4)}), \quad q = (q^{(1)}, q^{(2)}, q^{(3)}, q^{(4)}) \in Y_1, \end{aligned} \quad (3.20)$$

respectively

$$\begin{aligned} \langle p, q \rangle_{Y_2} &= \sum_{i,j} p_{i,j}^{(1)} q_{i,j}^{(1)} + p_{i,j}^{(2)} q_{i,j}^{(2)} + p_{i,j}^{(3)} q_{i,j}^{(3)} + p_{i,j}^{(4)} q_{i,j}^{(4)} + p_{i,j}^{(5)} q_{i,j}^{(5)} + p_{i,j}^{(6)} q_{i,j}^{(6)}, \\ p &= (p^{(1)}, p^{(2)}, p^{(3)}, p^{(4)}, p^{(5)}, p^{(6)}), \\ q &= (q^{(1)}, q^{(2)}, q^{(3)}, q^{(4)}, q^{(5)}, q^{(6)}) \in Y_2. \end{aligned} \quad (3.21)$$

After the discretisation of problem Eq. (3.19) we obtain

$$\begin{aligned} \min_{\bar{w}^+ \in X} \left\{ \mu \|\nabla \bar{w}^+\|_1 + \sum_{i,j} \left(\gamma_1 |\rho_1(\bar{w}_{i,j}^+)| \right. \right. \\ \left. \left. + \gamma_2 |\rho_2^{(1)}(\bar{w}_{i,j}^+)| + \gamma_2 |\rho_2^{(2)}(\bar{w}_{i,j}^+)| \right) \tilde{u}_{i,j} \right\}, \end{aligned} \quad (3.22)$$

where this time $\|\nabla s\|_1$, with $s = (s_1, s_2) \in X$, is given by $\|\nabla s\|_1 = \sum_{i,j} |(\nabla s)_{i,j}|$ with $|(\nabla s)_{i,j}| = \sqrt{((\nabla s_1)_{i,j}^{(1)})^2 + ((\nabla s_1)_{i,j}^{(2)})^2 + ((\nabla s_2)_{i,j}^{(1)})^2 + ((\nabla s_2)_{i,j}^{(2)})^2}$.

In the following we want to have a look at the two different variants on how to solve Eq. (3.22) with the primal-dual approach, namely **VARIANT I** and **VARIANT II**, separately. We therefore split the following derivations into two sections named accordingly.

Variant I

In this section we want to describe a first variant on how to solve Eq. (3.22) with the primal-dual approach.

When we compare Eq. (3.22) to Eq. (3.13), we see that we can choose the corresponding functions as $K = \nabla$, $F(\nabla \vec{w}^+) = \mu \|\nabla \vec{w}^+\|_1$ and

$$G(\vec{w}^+) = \sum_{i,j} (\gamma_1 |\rho_1(\vec{w}_{i,j}^+)| + \gamma_2 |\rho_2^{(1)}(\vec{w}_{i,j}^+)| + \gamma_2 |\rho_2^{(2)}(\vec{w}_{i,j}^+)|) \tilde{u}_{i,j}. \quad (3.23)$$

We want to point out again, that in this variant we will use the space $Y = Y_1$ defined at the beginning of Section 3.4.2. From the resolvent operator with respect to F^* we obtain then

$$q = (I + \sigma \partial F^*)^{-1}(\tilde{q}) \implies q_{i,j} = \mu \frac{\tilde{q}_{i,j}}{\max\{\mu, |\tilde{q}_{i,j}|\}}. \quad (3.24)$$

The derivation of the resolvent operator with respect to G is not that straightforward and more effort has to be put in to find a suitable solution. It is common that the resolvent operators of functions, that are sums of quadratic and absolute norms, lead to so called thresholding schemes [19, 92]. This will be also the case here. Having a closer look at the definition of G Eq. (3.23) and equation Eq. (3.15), we see that we have to solve

$$\begin{aligned} \vec{w}^+ &= (I + \tau \partial G)^{-1}(\vec{w}_0^+) \\ &= \arg \min_{\vec{w}^+ \in X} \left\{ \frac{\|\vec{w}^+ - \vec{w}_0^+\|_X^2}{2\tau} + G(\vec{w}^+) \right\} \\ &= \arg \min_{\vec{w}^+ = (u^+, v^+) \in X} \left\{ \frac{1}{2\tau} \sum_{i,j} \left((u_{i,j}^+ - u_{0,i,j}^+)^2 + (v_{i,j}^+ - v_{0,i,j}^+)^2 \right) \right. \\ &\quad \left. + \sum_{i,j} (\gamma_1 |\rho_1(\vec{w}_{i,j}^+)| + \gamma_2 |\rho_2^{(1)}(\vec{w}_{i,j}^+)| + \gamma_2 |\rho_2^{(2)}(\vec{w}_{i,j}^+)|) \tilde{u}_{i,j} \right\}. \end{aligned} \quad (3.25)$$

For $\tilde{u}_{i,j} = 0$ we can conclude from Eq. (3.25) that $\vec{w}_{i,j}^+ = \vec{w}_{0,i,j}^+$. On the other hand, for $\tilde{u}_{i,j} = 1$ we have to distinguish the cases

$$\rho_1(\vec{w}_{i,j}^+) \begin{pmatrix} \geq \\ = \end{pmatrix} 0, \quad \rho_2^{(1)}(\vec{w}_{i,j}^+) \begin{pmatrix} \geq \\ = \end{pmatrix} 0, \quad \rho_2^{(2)}(\vec{w}_{i,j}^+) \begin{pmatrix} \geq \\ = \end{pmatrix} 0, \quad (3.26)$$

which turn out to be 27 in total. The chosen numbering for the different cases is shown in Table 3.1.

Table 3.1: This table indicates the numbering of the 27 cases (see Eq. (3.26)).

Case No.	$\rho_1(\vec{w}_{i,j}^+) \diamond 0$	$\rho_2^{(1)}(\vec{w}_{i,j}^+) \diamond 0$	$\rho_2^{(2)}(\vec{w}_{i,j}^+) \diamond 0$
1	>	>	>
2	<	>	>
3	=	>	>
4	>	<	>
5	<	<	>
6	=	<	>
7	>	>	<
8	<	>	<
9	=	>	<
10	>	<	<
11	<	<	<
12	=	<	<
13	>	=	>
14	<	=	>
15	=	=	>
16	>	=	<
17	<	=	<
18	=	=	<
19	>	=	=
20	<	=	=
21	=	=	=
22	>	>	=
23	<	>	=
24	=	>	=
25	>	<	=
26	<	<	=
27	=	<	=

• **Geometric Interpretation of Problem Eq. (3.25) with $\tilde{u}_{i,j} = 1$**

Before explaining the derivation of the explicit solutions and the needed reformulation of the conditions for the different cases in Eq. (3.26) in more detail, we want to give a deeper insight of the geometric interpretation of problem Eq. (3.25) with $\tilde{u}_{i,j} = 1$. To facilitate the notation in the following, we introduce the terms

$$\begin{aligned} a_{i,j} &= \nabla T(\vec{x} + \vec{w}_0^+) \Big|_{i,j}, \\ b_{i,j} &= \begin{pmatrix} \partial_{x_1 x_1} T(\vec{x} + \vec{w}_0^+) \\ \partial_{x_2 x_1} T(\vec{x} + \vec{w}_0^+) \end{pmatrix} \Big|_{i,j}, \\ c_{i,j} &= \begin{pmatrix} \partial_{x_1 x_2} T(\vec{x} + \vec{w}_0^+) \\ \partial_{x_2 x_2} T(\vec{x} + \vec{w}_0^+) \end{pmatrix} \Big|_{i,j}, \end{aligned} \quad (3.27)$$

and

$$x_{i,j} = \tau \gamma_1 a_{i,j}, \quad y_{i,j} = \tau \gamma_2 b_{i,j}, \quad z_{i,j} = \tau \gamma_2 c_{i,j}. \quad (3.28)$$

Using the definitions in Eq. (3.7), Eq. (3.8) and Eq. (3.9) and the notation in Eq. (3.27), we can rewrite $\rho_1(\vec{w}_{i,j}^+)$, $\rho_2^{(1)}(\vec{w}_{i,j}^+)$ and $\rho_2^{(2)}(\vec{w}_{i,j}^+)$ as

$$\begin{aligned} \rho_1(\vec{w}_{i,j}^+) &= \rho_1(\vec{w}_{0i,j}^+) + a_{i,j}^T (\vec{w}_{i,j}^+ - \vec{w}_{0i,j}^+), \\ \rho_2^{(1)}(\vec{w}_{i,j}^+) &= \rho_2^{(1)}(\vec{w}_{0i,j}^+) + b_{i,j}^T (\vec{w}_{i,j}^+ - \vec{w}_{0i,j}^+), \text{ and} \\ \rho_2^{(2)}(\vec{w}_{i,j}^+) &= \rho_2^{(2)}(\vec{w}_{0i,j}^+) + c_{i,j}^T (\vec{w}_{i,j}^+ - \vec{w}_{0i,j}^+). \end{aligned} \quad (3.29)$$

Note, that with $\rho_1(\vec{w}_{i,j}^+) = 0$ a line $l_{a_{i,j}}$ is defined with its normal vector being parallel to the vector $a_{i,j}$. Similarly, $\rho_2^{(1)}(\vec{w}_{i,j}^+) = 0$ defines a line $l_{b_{i,j}}$ and $\rho_2^{(2)}(\vec{w}_{i,j}^+) = 0$ a line $l_{c_{i,j}}$.

Now we can argue similar to Zach *et al.* in [92] for the geometric interpretation. The mathematical structure of their minimisation problem for which they derive the thresholding scheme is very similar to the one we have in Eq. (3.25) with $\tilde{u}_{i,j} = 1$. The first term in Eq. (3.25), $(u_{i,j}^+ - u_{0i,j}^+)^2 + (v_{i,j}^+ - v_{0i,j}^+)^2$, is the squared distance of $\vec{w}_{i,j}^+$ to $\vec{w}_{0i,j}^+$, and the terms $|\rho_1(\vec{w}_{i,j}^+)|$, $|\rho_2^{(1)}(\vec{w}_{i,j}^+)|$, $|\rho_2^{(2)}(\vec{w}_{i,j}^+)|$ define the unsigned distances to the lines $l_{a_{i,j}}$, $l_{b_{i,j}}$, $l_{c_{i,j}}$, respectively. Considering now all $\vec{w}_{\delta i,j}^+$ with a fixed distance δ to $\vec{w}_{0i,j}^+$, we see that problem Eq. (3.25) with $\tilde{u}_{i,j} = 1$ is minimised for the $\vec{w}_{\delta i,j}^+$ closest to the three lines $l_{a_{i,j}}$, $l_{b_{i,j}}$ and $l_{c_{i,j}}$. See Fig. 3.1 for an illustration.

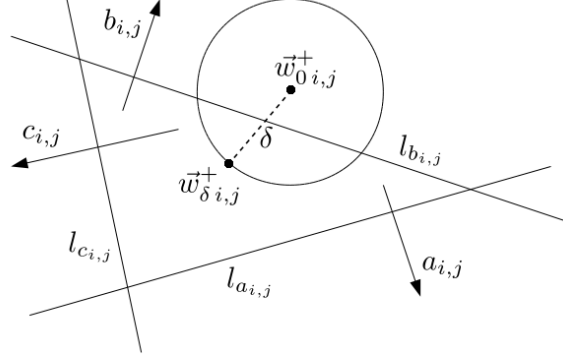


Figure 3.1: The geometric interpretation of minimisation problem Eq. (3.25) with $\tilde{u}_{i,j} = 1$.

• **Derivation of the Explicit Solutions for Problem Eq. (3.25) with $\tilde{u}_{i,j} = 1$**

We are ready now to derive for each of the cases an explicit solution by using Eq. (3.25). We show the derivation of the solutions only for four different cases. The explicit solutions for the remaining cases can be calculated in a similar fashion as the presented ones.

Case 1 and Similar Ones. Let us consider the first case in Table 3.1, *i.e.*

$$\begin{aligned} \rho_1(\vec{w}_{i,j}^+) &= \rho_1(\vec{w}_{0i,j}^+) + a_{i,j}^T (\vec{w}_{i,j}^+ - \vec{w}_{0i,j}^+) > 0, \\ \rho_2^{(1)}(\vec{w}_{i,j}^+) &= \rho_2^{(1)}(\vec{w}_{0i,j}^+) + b_{i,j}^T (\vec{w}_{i,j}^+ - \vec{w}_{0i,j}^+) > 0, \\ \rho_2^{(2)}(\vec{w}_{i,j}^+) &= \rho_2^{(2)}(\vec{w}_{0i,j}^+) + c_{i,j}^T (\vec{w}_{i,j}^+ - \vec{w}_{0i,j}^+) > 0. \end{aligned} \quad (3.30)$$

Solving problem Eq. (3.25) for this case leads to the equation

$$\frac{1}{2\tau} 2(\vec{w}_{i,j}^+ - \vec{w}_{0i,j}^+) + \gamma_1 a_{i,j} + \gamma_2 b_{i,j} + \gamma_3 c_{i,j} \stackrel{!}{=} \vec{0},$$

and by using the notation in Eq. (3.28) the explicit solution can then be written as

$$\vec{w}_{i,j}^+ = \vec{w}_{0i,j}^+ - x_{i,j} - y_{i,j} - z_{i,j}. \quad (3.31)$$

The derivation of the explicit solutions for the cases 2, 4, 5, 7, 8, 10 and 11 in Table 3.1 is performed similarly. There are, however, other cases left which need another treatment, as for example case number 3.

Case 3 and Similar Ones. The condition for case 3 in Table 3.1 is given by

$$\begin{aligned}\rho_1(\vec{w}_{i,j}^+) &= \rho_1(\vec{w}_{0i,j}^+) + a_{i,j}^T (\vec{w}_{i,j}^+ - \vec{w}_{0i,j}^+) = 0, \\ \rho_2^{(1)}(\vec{w}_{i,j}^+) &= \rho_2^{(1)}(\vec{w}_{0i,j}^+) + b_{i,j}^T (\vec{w}_{i,j}^+ - \vec{w}_{0i,j}^+) > 0, \\ \rho_2^{(2)}(\vec{w}_{i,j}^+) &= \rho_2^{(2)}(\vec{w}_{0i,j}^+) + c_{i,j}^T (\vec{w}_{i,j}^+ - \vec{w}_{0i,j}^+) > 0.\end{aligned}$$

Here we have to distinguish the two situations $a_{i,j} \neq \vec{0}$ and $a_{i,j} = \vec{0}$.

- If $a_{i,j} \neq \vec{0}$:

From $\rho_1(\vec{w}_{i,j}^+) = 0$ we see, that the solution $\vec{w}_{i,j}^+$ has to lie on the line $l_{a_{i,j}}$ and of course the distance of it to the other lines $l_{b_{i,j}}$ and $l_{c_{i,j}}$ should be minimal. Therefore we can assume that the solution is of the form

$$\vec{w}_{i,j}^+ = \vec{w}_{0i,j}^+ + \alpha_1 a_{i,j} + \beta_{0pp} n_{a_{i,j}}, \quad (3.32)$$

where $n_{a_{i,j}}$ is the normal to $a_{i,j}$. Geometrically this means, that $\vec{w}_{0i,j}^+$ is first orthogonally projected to the line $l_{a_{i,j}}$ and afterwards moved along the line such that it minimises the distance to $l_{b_{i,j}}$ and $l_{c_{i,j}}$.

The unknown α_1 is determined by replacing the term $(\vec{w}_{i,j}^+ - \vec{w}_{0i,j}^+)$ in the equation $\rho_1(\vec{w}_{i,j}^+) = 0$ using Eq. (3.32), which leads to

$$\alpha_1 = -\frac{\rho_1(\vec{w}_{0i,j}^+)}{|a_{i,j}|^2}. \quad (3.33)$$

Solving problem Eq. (3.25) for the current case and replacing again the term $(\vec{w}_{i,j}^+ - \vec{w}_{0i,j}^+)$ using Eq. (3.32) leads after some simple calculations to the second parameter

$$\beta_{0pp} = \frac{n_{a_{i,j}}^T (-y_{i,j} - z_{i,j})}{|n_{a_{i,j}}|^2}.$$

- If $a_{i,j} = \vec{0}$:

Since $a_{i,j}$ vanishes, there is also no line $l_{a_{i,j}}$ we have to consider and we can directly derive the solution $\vec{w}_{i,j}^+$ by just solving Eq. (3.25), similar to the first case in Table 3.1, and we get the solution

$$\vec{w}_{i,j}^+ = \vec{w}_{0i,j}^+ - y_{i,j} - z_{i,j}.$$

Finally, we can derive the explicit solution for the cases 6, 9, 12, 13, 14, 16, 17, 22, 23, 25 and 26 in Table 3.1 similar to the case 3 above.

Case 15 and Similar Ones. Let us now consider case number 15, which was not covered so far. The condition is this time give by

$$\begin{aligned}\rho_1(\vec{w}_{i,j}^+) &= \rho_1(\vec{w}_{0i,j}^+) + a_{i,j}^T (\vec{w}_{i,j}^+ - \vec{w}_{0i,j}^+) = 0, \\ \rho_2^{(1)}(\vec{w}_{i,j}^+) &= \rho_2^{(1)}(\vec{w}_{0i,j}^+) + b_{i,j}^T (\vec{w}_{i,j}^+ - \vec{w}_{0i,j}^+) = 0, \\ \rho_2^{(2)}(\vec{w}_{i,j}^+) &= \rho_2^{(2)}(\vec{w}_{0i,j}^+) + c_{i,j}^T (\vec{w}_{i,j}^+ - \vec{w}_{0i,j}^+) > 0,\end{aligned}$$

and we see that we have now two equal signs, namely for $\rho_1(\vec{w}_{i,j}^+)$ and $\rho_2^{(1)}(\vec{w}_{i,j}^+)$. This time we have to distinguish the situations $a_{i,j} \neq \vec{0}$, $a_{i,j} = \vec{0} \wedge b_{i,j} \neq \vec{0}$ and $a_{i,j} = \vec{0} \wedge b_{i,j} = \vec{0}$.

- If $a_{i,j} \neq \vec{0}$:

From $\rho_1(\vec{w}_{i,j}^+) = 0$ and $\rho_2^{(1)}(\vec{w}_{i,j}^+) = 0$ we see, that the solution $\vec{w}_{i,j}^+$ has to lie on the lines $l_{a_{i,j}}$ and $l_{b_{i,j}}$ and should have a minimal distance to the line $l_{c_{i,j}}$. Thus, we assume that the explicit solution is of the form

$$\vec{w}_{i,j}^+ = \vec{w}_{0i,j}^+ + \alpha_1 a_{i,j} + \beta_{00p} n_{a_{i,j}}. \quad (3.34)$$

Similar to the last paragraph, replacing the term $(\vec{w}_{i,j}^+ - \vec{w}_{0i,j}^+)$ in the equation $\rho_1(\vec{w}_{i,j}^+) = 0$ by making use of Eq. (3.34) leads to the same α_1 as in Eq. (3.33). For the parameter β_{00p} we get

$$\beta_{00p} = \begin{cases} \frac{-\rho_2^{(1)}(\vec{w}_{0i,j}^+) - \alpha_1 b_{i,j}^T a_{i,j}}{b_{i,j}^T n_{a_{i,j}}} & \text{if } b_{i,j}^T n_{a_{i,j}} \neq 0, \\ \frac{n_{a_{i,j}}^T (-z_{i,j})}{|n_{a_{i,j}}|^2} & \text{if } b_{i,j}^T n_{a_{i,j}} = 0. \end{cases} \quad (3.35)$$

The case where $b_{i,j}^T n_{a_{i,j}} \neq 0$ in Eq. (3.35), which is equivalent to $a_{i,j} \nparallel b_{i,j}$, indicates that the lines $l_{a_{i,j}}$ and $l_{b_{i,j}}$ are not parallel and that they therefore intersect each other in one point. The solution $\vec{w}_{i,j}^+$ we look for will be at this intersection and the corresponding β_{00p} is calculated by replacing the term $(\vec{w}_{i,j}^+ - \vec{w}_{0i,j}^+)$ in the equation $\rho_2^{(1)}(\vec{w}_{i,j}^+) = 0$ using Eq. (3.34). For the case where $b_{i,j}^T n_{a_{i,j}} = 0$ in Eq. (3.35), which is equivalent to $a_{i,j} \parallel b_{i,j}$, we conclude that the lines $l_{a_{i,j}}$ and $l_{b_{i,j}}$ are parallel. This means, that if the solution $\vec{w}_{i,j}^+$ lies on the line $l_{a_{i,j}}$ it necessarily also lies on the line $l_{b_{i,j}}$ and the parameter β_{00p} is calculated by solving problem Eq. (3.25) for the current case and replacing the term $(\vec{w}_{i,j}^+ - \vec{w}_{0i,j}^+)$ using Eq. (3.34).

- If $a_{i,j} = \vec{0} \wedge b_{i,j} \neq \vec{0}$:

Since $a_{i,j}$ vanishes, there is no need to consider the line $l_{a_{i,j}}$ and we

focus instead on the line $l_{b_{i,j}}$ on which the solution $\vec{w}_{i,j}^+$ has to lie on too. We therefore assume the solution has the form

$$\vec{w}_{i,j}^+ = \vec{w}_{0i,j}^+ + \alpha_2 b_{i,j} + \beta_{00p} n_{b_{i,j}}. \quad (3.36)$$

Replacing this time the term $(\vec{w}_{i,j}^+ - \vec{w}_{0i,j}^+)$ in the equation $\rho_2^{(1)}(\vec{w}_{i,j}^+) = 0$ with the help of Eq. (3.36) results in

$$\alpha_2 = -\frac{\rho_2^{(1)}(\vec{w}_{0i,j}^+)}{|b_{i,j}|^2}. \quad (3.37)$$

After solving problem Eq. (3.25) and replacing the term $(\vec{w}_{i,j}^+ - \vec{w}_{0i,j}^+)$ using Eq. (3.36) we get

$$\beta_{00p} = \frac{n_{b_{i,j}}^T(-z_{i,j})}{|n_{b_{i,j}}|^2}.$$

- If $a_{i,j} = \vec{0} \wedge b_{i,j} = \vec{0}$:

This time both, $a_{i,j}$ and $b_{i,j}$ vanish and the corresponding lines $l_{a_{i,j}}$ and $l_{b_{i,j}}$ play not a role in the derivation of the solution $\vec{w}_{i,j}^+$ anymore. We can directly solve problem Eq. (3.25) without any prior assumption, similar as done before in other cases, and we get

$$\vec{w}_{i,j}^+ = \vec{w}_{0i,j}^+ - z_{i,j}.$$

The derivation of the explicit solutions for the cases 18, 19, 20, 24 and 27 in Table 3.1 is done similarly to the case 15 explained above.

Case 21. There is now one case left, which was not discussed so far. The corresponding condition from Table 3.1 is

$$\begin{aligned} \rho_1(\vec{w}_{i,j}^+) &= \rho_1(\vec{w}_{0i,j}^+) + a_{i,j}^T(\vec{w}_{i,j}^+ - \vec{w}_{0i,j}^+) = 0, \\ \rho_2^{(1)}(\vec{w}_{i,j}^+) &= \rho_2^{(1)}(\vec{w}_{0i,j}^+) + b_{i,j}^T(\vec{w}_{i,j}^+ - \vec{w}_{0i,j}^+) = 0, \\ \rho_2^{(2)}(\vec{w}_{i,j}^+) &= \rho_2^{(2)}(\vec{w}_{0i,j}^+) + c_{i,j}^T(\vec{w}_{i,j}^+ - \vec{w}_{0i,j}^+) = 0, \end{aligned}$$

This time we have three equal signs and we have to distinguish the situations $a_{i,j} \neq \vec{0}$, $a_{i,j} = \vec{0} \wedge b_{i,j} \neq \vec{0}$, $a_{i,j} = \vec{0} \wedge b_{i,j} = \vec{0} \wedge c_{i,j} \neq \vec{0}$ and $a_{i,j} = \vec{0} \wedge b_{i,j} = \vec{0} \wedge c_{i,j} = \vec{0}$.

- If $a_{i,j} \neq \vec{0}$:

Since $\rho_1(\vec{w}_{i,j}^+) = 0$, $\rho_2^{(1)}(\vec{w}_{i,j}^+) = 0$ and $\rho_2^{(2)}(\vec{w}_{i,j}^+) = 0$, we see that the solution $\vec{w}_{i,j}^+$ has to lie this time on all three lines $l_{a_{i,j}}$, $l_{b_{i,j}}$ and $l_{c_{i,j}}$. For $a_{i,j} \neq \vec{0}$ we assume that the explicit solution is of the form

$$\vec{w}_{i,j}^+ = \vec{w}_{0i,j}^+ + \alpha_1 a_{i,j} + \beta_{000} n_{a_{i,j}}. \quad (3.38)$$

Like in the paragraphs before, replacing the term $(\vec{w}_{i,j}^+ - \vec{w}_{0i,j}^+)$ in $\rho_1(\vec{w}_{i,j}^+) = 0$ by making use of Eq. (3.38) leads to a α_1 being equal to the one in Eq. (3.33). To determine β_{000} in Eq. (3.38), we argue as follows:

- * If $b_{i,j}^T n_{a_{i,j}} \neq 0$, which is equivalent to $a_{i,j} \not\parallel b_{i,j}$, we use Eq. (3.38) in $\rho_2^{(1)}(\vec{w}_{i,j}^+) = 0$ and get

$$\beta_{000} = \frac{-\rho_2^{(1)}(\vec{w}_{0i,j}^+) - \alpha_1 b_{i,j}^T a_{i,j}}{b_{i,j}^T n_{a_{i,j}}}.$$

- * If $b_{i,j}^T n_{a_{i,j}} = 0$ and $c_{i,j}^T n_{a_{i,j}} \neq 0$, that is $a_{i,j} \parallel b_{i,j}$ and $a_{i,j} \not\parallel c_{i,j}$, we use Eq. (3.38) in $\rho_2^{(2)}(\vec{w}_{i,j}^+) = 0$ and get

$$\beta_{000} = \frac{-\rho_2^{(2)}(\vec{w}_{0i,j}^+) - \alpha_1 c_{i,j}^T a_{i,j}}{c_{i,j}^T n_{a_{i,j}}}.$$

- * If $b_{i,j}^T n_{a_{i,j}} = 0$ and $c_{i,j}^T n_{a_{i,j}} = 0$, this means that $a_{i,j} \parallel b_{i,j}$ and $a_{i,j} \parallel c_{i,j}$. Thus all the three lines $l_{a_{i,j}}$, $l_{b_{i,j}}$ and $l_{c_{i,j}}$ are parallel and by solving problem Eq. (3.25) and using Eq. (3.38) we get

$$\beta_{000} = 0.$$

- If $a_{i,j} = \vec{0} \wedge b_{i,j} \neq \vec{0}$:

Similar as in the discussion of Eq. (3.36) in case 15, we assume the solution is of the form

$$\vec{w}_{i,j}^+ = \vec{w}_{0i,j}^+ + \alpha_2 b_{i,j} + \beta_{000} n_{b_{i,j}}. \quad (3.39)$$

Replacing the term $(\vec{w}_{i,j}^+ - \vec{w}_{0i,j}^+)$ in $\rho_2^{(1)}(\vec{w}_{i,j}^+) = 0$ by making use of Eq. (3.39) leads to a α_2 being equal to the one in Eq. (3.37). For β_{000} in Eq. (3.39), we argue as follows:

- * If $c_{i,j}^T n_{b_{i,j}} \neq 0$, which is equivalent to $b_{i,j} \not\parallel c_{i,j}$, we make use of Eq. (3.39) in $\rho_2^{(2)}(\vec{w}_{i,j}^+) = 0$ and get

$$\beta_{000} = \frac{-\rho_2^{(2)}(\vec{w}_{0i,j}^+) - \alpha_2 c_{i,j}^T b_{i,j}}{c_{i,j}^T n_{b_{i,j}}}.$$

- * If $c_{i,j}^T n_{b_{i,j}} = 0$, which means $b_{i,j} \parallel c_{i,j}$, we get by solving Eq. (3.25) and using Eq. (3.39)

$$\beta_{000} = 0.$$

- If $a_{i,j} = \vec{0} \wedge b_{i,j} = \vec{0} \wedge c_{i,j} \neq \vec{0}$:
Here, $a_{i,j}$ and $b_{i,j}$ vanish and we focus therefore on the line $l_{c_{i,j}}$ on which the solution $\vec{w}_{i,j}^+$ has to lie. We assume the explicit solution is of the form

$$\vec{w}_{i,j}^+ = \vec{w}_{0i,j}^+ + \alpha_3 c_{i,j}, \quad (3.40)$$

where α_3 is calculated by using equation Eq. (3.40) to replace $(\vec{w}_{i,j}^+ - \vec{w}_{0i,j}^+)$ in $\rho_2^{(2)}(\vec{w}_{i,j}^+) = 0$ and is given by

$$\alpha_3 = -\frac{\rho_2^{(2)}(\vec{w}_{0i,j}^+)}{|c_{i,j}|^2}.$$

- If $a_{i,j} = \vec{0} \wedge b_{i,j} = \vec{0} \wedge c_{i,j} = \vec{0}$:
In this situation we do not have to consider the lines $l_{a_{i,j}}$, $l_{b_{i,j}}$ and $l_{c_{i,j}}$ at all and solving Eq. (3.25) results into

$$\vec{w}_{i,j}^+ = \vec{w}_{0i,j}^+.$$

- **Reformulation of the Conditions for Problem Eq. (3.25) with $\tilde{u}_{i,j} = 1$**

Since $\vec{w}_{i,j}^+$ is unknown but $\vec{w}_{0i,j}^+$ in Eq. (3.7), Eq. (3.8) and Eq. (3.9) known, we have to rewrite the conditions for the 27 cases, which are defined by Eq. (3.26), in terms of $\rho_1(\vec{w}_{0i,j}^+)$, $\rho_2^{(1)}(\vec{w}_{0i,j}^+)$ and $\rho_2^{(2)}(\vec{w}_{0i,j}^+)$. This can be done by incorporating the derived explicit solutions and finding a proper partitioning of the space spanned by $\rho_1(\vec{w}_{0i,j}^+)$, $\rho_2^{(1)}(\vec{w}_{0i,j}^+)$ and $\rho_2^{(2)}(\vec{w}_{0i,j}^+)$ (see Fig. 3.2). A similar approach was used in the work of Zach *et al.* [92] to reformulate the conditions for their proposed thresholding scheme.

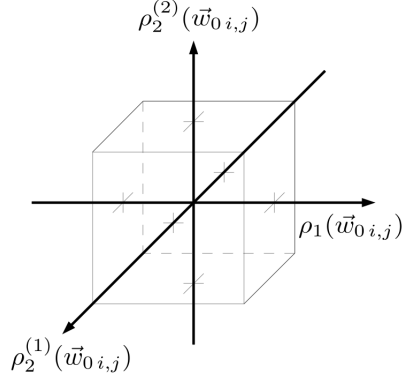


Figure 3.2: The space spanned by $\rho_1(\vec{w}_{0i,j}^+)$, $\rho_2^{(1)}(\vec{w}_{0i,j}^+)$ and $\rho_2^{(2)}(\vec{w}_{0i,j}^+)$.

As one can see in Fig. 3.2, we indicated a cube in the coordinate system, that will facilitate us the problem of finding a proper partitioning of the considered space. The edge length of the cube is chosen in such a way, that the critical values of the reformulated conditions are covered. The reader will understand the meaning of this sentence afterwards in a better way. For later need, we number the faces of the cube as shown in Fig. 3.3.

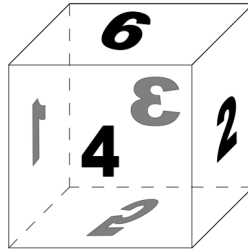


Figure 3.3: The numbering of the faces of the cube indicated in Fig. 3.2.

The orientation of the face numbers in Fig. 3.3 indicates from which direction we will look at the faces.

In the following we want to show how we can rewrite the conditions for the different cases. The same four groups of cases which were discussed in Section 3.4.2 are considered here too and for each of them the reformulation of the conditions can be achieved in a similar fashion.

Case 1 and Similar Ones. We start again with the first case in Table 3.1, which belongs to the group of cases that can be handled in the easiest way

compared to the other ones. The condition for this case is given in Eq. (3.30) and by using Eq. (3.31) to replace the term $(\vec{w}_{i,j}^+ - \vec{w}_{0,i,j}^+)$ in the condition we get

$$\begin{aligned}\rho_1(\vec{w}_{i,j}^+) &= \rho_1(\vec{w}_{0,i,j}^+) + a_{i,j}^T(-x_{i,j} - y_{i,j} - z_{i,j}) > 0, \\ \rho_2^{(1)}(\vec{w}_{i,j}^+) &= \rho_2^{(1)}(\vec{w}_{0,i,j}^+) + b_{i,j}^T(-x_{i,j} - y_{i,j} - z_{i,j}) > 0, \\ \rho_2^{(2)}(\vec{w}_{i,j}^+) &= \rho_2^{(2)}(\vec{w}_{0,i,j}^+) + c_{i,j}^T(-x_{i,j} - y_{i,j} - z_{i,j}) > 0,\end{aligned}$$

or rewritten

$$\begin{aligned}\rho_1(\vec{w}_{0,i,j}^+) &> -a_{i,j}^T(-x_{i,j} - y_{i,j} - z_{i,j}), \\ \rho_2^{(1)}(\vec{w}_{0,i,j}^+) &> -b_{i,j}^T(-x_{i,j} - y_{i,j} - z_{i,j}), \\ \rho_2^{(2)}(\vec{w}_{0,i,j}^+) &> -c_{i,j}^T(-x_{i,j} - y_{i,j} - z_{i,j}).\end{aligned}\tag{3.41}$$

One of the critical values we mentioned before concerning the edge length of the cube shown in Fig. 3.2 can be determined now for case number 1, namely by the values on the right-hand side in Eq. (3.41).

The reformulation of the conditions for the cases 2, 4, 5, 7, 8, 10 and 11 in Table 3.1 is achieved similarly to this case and the remaining seven critical values, which are necessary to define the edge length of the cube, are determined in the same way as above.

Remark 3.4. Before jumping to the next group of cases, we want to explain why the cube in Fig. 3.2 will help us in finding a proper partitioning of the space spanned by $\rho_1(\vec{w}_{0,i,j}^+)$, $\rho_2^{(1)}(\vec{w}_{0,i,j}^+)$ and $\rho_2^{(2)}(\vec{w}_{0,i,j}^+)$. Our aim is to divide the space into 27 parts, each one defining a region for which exactly one of the 27 cases may apply with their already derived explicit solutions. This partitioning should not be done just arbitrarily and has to be meaningful and be conform to the already set up formulations. Before we mentioned once, that we want the eight critical values from the paragraph before to be covered by the cube. The reason for this is, that like this it is possible to reduce the partitioning problem of the whole space to a partitioning problem of the cube. The uniquely defined regions of the cube are the ones from the corresponding eight cases discussed in the paragraph above and they define the corners of it. In Fig. 3.4 we show the location of the regions for different case numbers. For simplicity we drew all the regions with the same size, although they can and most likely will have different sizes. Note, that the region for case number 21 is not visible in the figure, because it fully lies in the interior of the cube.

Let us focus now on one face of the cube. We know the values for the boundaries of the corner regions from the critical values we got from the

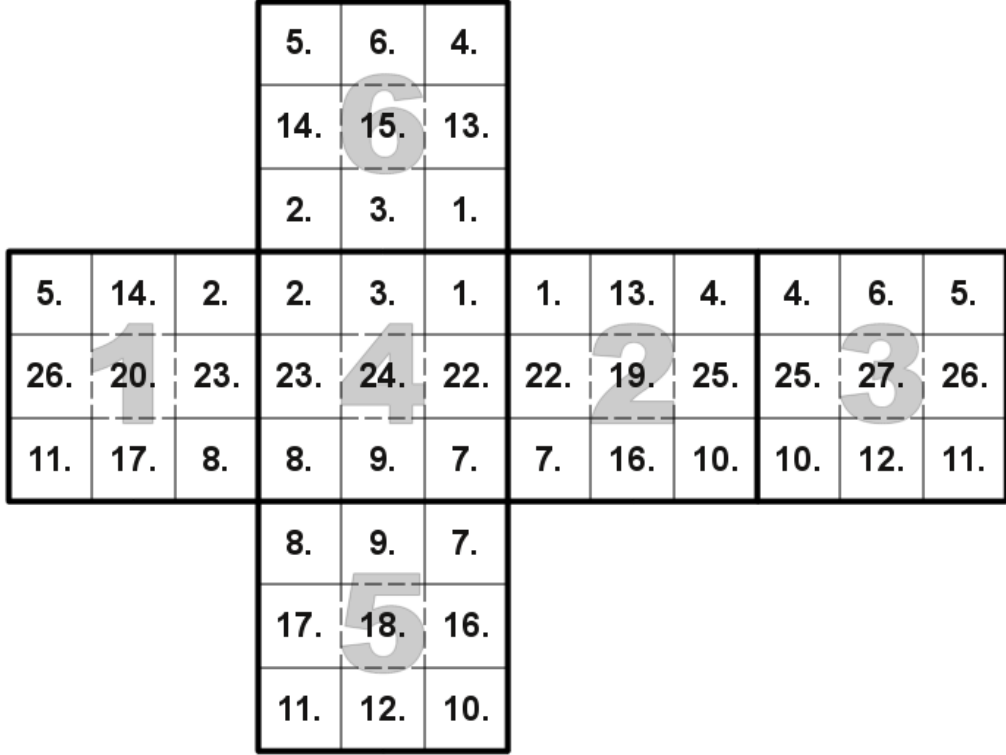


Figure 3.4: The net of the cube indicated in Fig. 3.2 with the corresponding case numbers for the different regions. The face numbers from Fig. 3.3 are visible in the background.

previous paragraph. They are fixed and we introduce for them the names $A_v, A_h, B_v, B_h, C_v, C_h, D_v$ and D_h as shown in Fig.3.5.

For face number 6 for example the values D_v and D_h will be the boundary values to region 1 (see Fig. 3.4) and after having a look at Eq. (3.41), we can conclude that $D_v = -a_{i,j}^T (-x_{i,j} - y_{i,j} - z_{i,j})$ and $D_h = -b_{i,j}^T (-x_{i,j} - y_{i,j} - z_{i,j})$. For each face it always holds that

$$A_v \leq B_v, \quad C_v \leq D_v, \quad B_h \leq D_h, \quad A_h \leq C_h.$$

For example, to see that $C_v \leq D_v$ we consider the reformulation of the condition for case number 2

$$\begin{aligned} \rho_1(\vec{w}_{0,i,j}^+) &< -a_{i,j}^T (+x_{i,j} - y_{i,j} - z_{i,j}), \\ \rho_2^{(1)}(\vec{w}_{0,i,j}^+) &> -b_{i,j}^T (+x_{i,j} - y_{i,j} - z_{i,j}), \\ \rho_2^{(2)}(\vec{w}_{0,i,j}^+) &> -c_{i,j}^T (+x_{i,j} - y_{i,j} - z_{i,j}), \end{aligned} \tag{3.42}$$

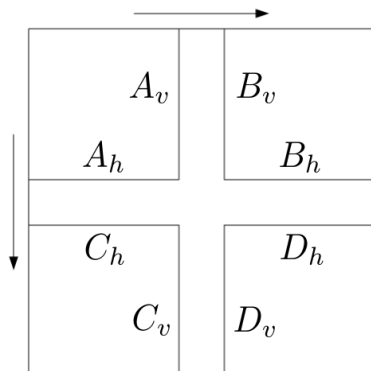


Figure 3.5: One face of the cube with the depicted corner regions and the labelling of the boundary values. The arrows indicate the direction of increase.

which can be derived, as mentioned before, similarly to case number 1. For face number 6 we see in the same manner as before by having a look at Fig. 3.4 and Eq. (3.42) that $C_v = -a_{i,j}^T (+x_{i,j} - y_{i,j} - z_{i,j})$. Since $a_{i,j}^T x_{i,j} = \tau \gamma_1 |a_{i,j}|^2 \geq 0$ (see Eq. (3.28)), we can conclude that $C_v \leq D_v$.

Let us consider again an arbitrary face of the cube. Although we have boundaries for the corner regions the ones for the regions in between are not fully defined. Since a rectangular division of the face seems to be adequate, we investigate the problem on how to achieve such a one. In Fig. 3.6 a face is depicted with its corner regions and two ways of possible divisions into 9 rectangles are shown, which we call the “clockwise” and “anti-clockwise” division method.

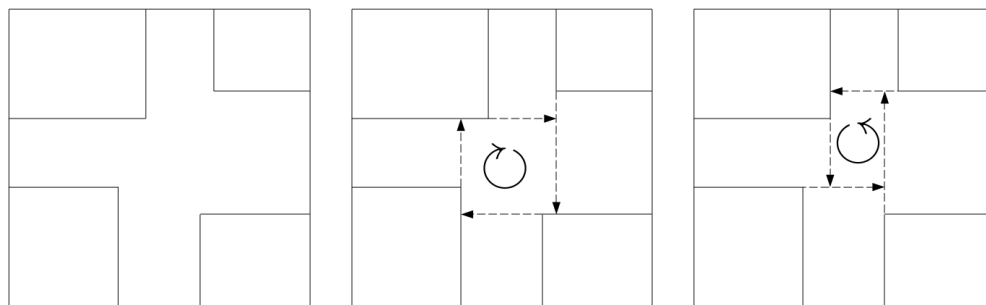


Figure 3.6: A face with its depicted corner regions (*left*) and the clockwise (*middle*) respectively anti-clockwise (*right*) division method.

Depending on the values for $A_v, A_h, B_v, B_h, C_v, C_h, D_v$ and D_h sometimes both, the clockwise and the anti-clockwise division method work, as for example in Fig. 3.6. Depending on the situation, however, there can be also values for which only the clockwise or the anti-clockwise or even none of the both methods will work, where in the latter situation another adequate division method has to be defined.

In Table 3.2 we list the different possible situations for the values $A_v, A_h, B_v, B_h, C_v, C_h, D_v$ and D_h .

Furthermore, we split the last situation S9 into its parts for later use and introduce the corresponding labelling in Table 3.3.

In the following, we go through the different situations given in Table 3.2 and Table 3.3 and decide which kind of method can be used to achieve a division of the face into 9 rectangular regions.

- Situation S1 in Table 3.2 is illustrated in Fig. 3.7 for face number 6 and the corresponding region numbers. For this situation, neither the clockwise nor the anti-clockwise division method will work, since the corner regions 1 and 5 overlap. An adapted division method, which is depicted in Fig. 3.7 will be used instead for this situation. Note, that

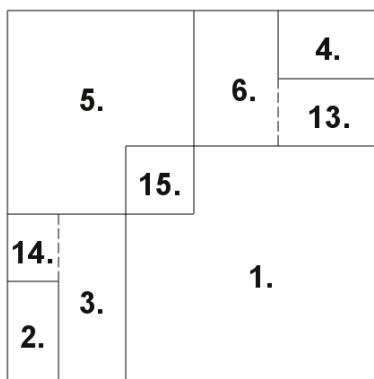


Figure 3.7: The division method used for situation S1 in Table 3.2. For the illustration we used face number 6 and the corresponding region numbers.

in this situation certain corner regions, which were defined through the reformulation of the conditions for the group of cases similar to case 1, have to be adapted by removing from them the region where they overlap.

- For the situations S2, S3, S5, S6 in Table 3.2 and S9.1, S9.2, S9.3, S9.4, S9.5 in Table 3.3 we can use the clockwise division method illustrated

Table 3.2: Different possible situations for the values $A_v, A_h, B_v, B_h, C_v, C_h, D_v$ and D_h .

No.	$A_v \diamond D_v$	$B_v \diamond C_v$	$A_h \diamond D_h$	$B_h \diamond C_h$
S1	>	>	>	<
S2	>	>	=	$\left(\begin{smallmatrix} \leq \\ = \end{smallmatrix}\right)$
S3	>	>	<	$\left(\begin{smallmatrix} \geq \\ \leq \\ = \end{smallmatrix}\right)$
S4	=	$\left(\begin{smallmatrix} \geq \\ = \end{smallmatrix}\right)$	>	<
S5	=	$\left(\begin{smallmatrix} \geq \\ = \end{smallmatrix}\right)$	=	$\left(\begin{smallmatrix} \leq \\ = \end{smallmatrix}\right)$
S6	=	$\left(\begin{smallmatrix} \geq \\ = \end{smallmatrix}\right)$	<	$\left(\begin{smallmatrix} \geq \\ \leq \\ = \end{smallmatrix}\right)$
S7	<	$\left(\begin{smallmatrix} \geq \\ \leq \\ = \end{smallmatrix}\right)$	>	<
S8	<	$\left(\begin{smallmatrix} \geq \\ \leq \\ = \end{smallmatrix}\right)$	=	$\left(\begin{smallmatrix} \leq \\ = \end{smallmatrix}\right)$
S9	<	$\left(\begin{smallmatrix} \geq \\ \leq \\ = \end{smallmatrix}\right)$	<	$\left(\begin{smallmatrix} \geq \\ \leq \\ = \end{smallmatrix}\right)$

Table 3.3: Splitting of the situation S9 in Table 3.2 into its parts.

No.	$A_v \diamond D_v$	$B_v \diamond C_v$	$A_h \diamond D_h$	$B_h \diamond C_h$
S9.1	<	>	<	>
S9.2	<	>	<	=
S9.3	<	>	<	<
S9.4	<	=	<	>
S9.5	<	=	<	=
S9.6	<	=	<	<
S9.7	<	<	<	>
S9.8	<	<	<	=
S9.9	<	<	<	<

in Fig. 3.6. We define the set of situations for which the clockwise division method can be applied by

$$\mathcal{S}_c := \{S2, S3, S5, S6, S9.1, S9.2, S9.3, S9.4, S9.5\}. \quad (3.43)$$

- Situation S9.7 in Table 3.3 needs again a special treatment to achieve a meaningful division, since neither the clockwise nor the anti-clockwise division method can be applied because of the overlapping of the corner regions 2 and 4, if we consider face number 6 for example. The adapted division method, which will be used instead, is shown in Fig. 3.8 for face number 6 and the corresponding region numbers. Note again, that also

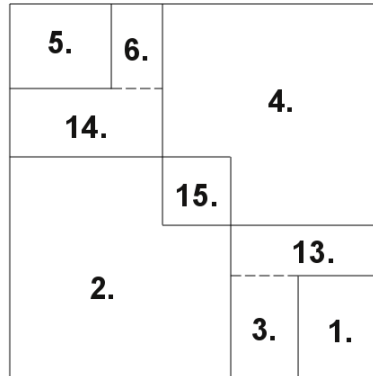


Figure 3.8: The division method used for situation S9.7 in Table 3.3. For the illustration we used again face number 6 and the corresponding region numbers.

in this situation certain corner regions have to be adapted by removing from them the region where they overlap.

- Finally, for the situations S4, S7, S8 in Table 3.2 and S9.6, S9.8, S9.9 in Table 3.3 we can use this time the anti-clockwise division method illustrated in Fig. 3.6. The set of situations for which the anti-clockwise division method can be applied is then given by

$$\mathcal{S}_{ac} := \{S4, S7, S8, S9.6, S9.8, S9.9\}. \quad (3.44)$$

We are now able to give an idea on how to reformulate the conditions for the remaining group of cases.

Case 3 and Similar Ones. The reformulation of the cases in this group with the same approach as for case number 1 will not lead to a proper partitioning of the space shown in Fig. 3.2. Instead we will use a more geometrically based approach which depends on the different situations the boundary values can take.

First we can derive for sure, independently which approach we use, that

$$|\rho_1(\vec{w}_{0i,j}^+) + a_{i,j}^T(-y_{i,j} - z_{i,j})| \leq a_{i,j}^T x_{i,j}.$$

This can be seen by considering Fig. 3.4, from which we can deduce that region 3 has to lie between the regions 1 and 2. By using the critical values of this adjacent regions, which can be determined from Eq. (3.41) and Eq. (3.42), we arrive at the inequality above.

For the reformulation of the condition with respect to $\rho_2^{(1)}(\vec{w}_{0i,j}^+)$, we consider the different situations in which the boundary values of the corner regions can be for face number 6.

- If the boundary values are in situation S1 given in Table 3.2, the reformulation is given by

$$\rho_2^{(1)}(\vec{w}_{0i,j}^+) + b_{i,j}^T(+x_{i,j} + y_{i,j} - z_{i,j}) \geq 0.$$

- If the boundary values are in one of the situations in the set \mathcal{S}_c defined in Eq. (3.43) or in situation S9.7 in Table 3.3, we get

$$\rho_2^{(1)}(\vec{w}_{0i,j}^+) + b_{i,j}^T(-x_{i,j} - y_{i,j} - z_{i,j}) > 0.$$

- If the boundary values are in one of the situations in \mathcal{S}_{ac} Eq. (3.44), the reformulation is

$$\rho_2^{(1)}(\vec{w}_{0i,j}^+) + b_{i,j}^T (+x_{i,j} - y_{i,j} - z_{i,j}) > 0.$$

For the reformulation of the condition with respect to $\rho_2^{(2)}(\vec{w}_{0i,j}^+)$, we consider this time the different situations belonging to face number 4.

- If the boundary values are in situation S1, the reformulation is given by

$$\rho_2^{(2)}(\vec{w}_{0i,j}^+) + c_{i,j}^T (-x_{i,j} - y_{i,j} + z_{i,j}) \geq 0.$$

- If the situation of the boundary values is in the set \mathcal{S}_c or corresponds to the situation S9.7, we get

$$\rho_2^{(2)}(\vec{w}_{0i,j}^+) + c_{i,j}^T (+x_{i,j} - y_{i,j} - z_{i,j}) > 0.$$

- Finally, if the situation of the boundary values is in \mathcal{S}_{ac} , the reformulation is

$$\rho_2^{(2)}(\vec{w}_{0i,j}^+) + c_{i,j}^T (-x_{i,j} - y_{i,j} - z_{i,j}) > 0.$$

Finally, the reformulation of the conditions for the cases 6, 9, 12, 13, 14, 16, 17, 22, 23, 25 and 26 in Table 3.1 is achieved similarly to this case.

Case 15 and Similar Ones. For this group of cases we will again make use of the different situations of the boundary values, but this time only for face number 6.

For the reformulation of the condition with respect to $\rho_1(\vec{w}_{0i,j}^+)$, we get the following list.

- If the boundary values are in situation S1

$$|\rho_1(\vec{w}_{0i,j}^+) + a_{i,j}^T (-z_{i,j})| < -a_{i,j}^T (+x_{i,j} + y_{i,j}).$$

- If the situation of the boundary values is in the set \mathcal{S}_c

$$|\rho_1(\vec{w}_{0i,j}^+) + a_{i,j}^T (-z_{i,j})| \leq -a_{i,j}^T (-x_{i,j} + y_{i,j}).$$

- If the boundary values are in situation S9.7

$$|\rho_1(\vec{w}_{0i,j}^+) + a_{i,j}^T(-z_{i,j})| < -a_{i,j}^T(+x_{i,j} - y_{i,j}).$$

- If the situation of the boundary values is in the set \mathcal{S}_{ac}

$$|\rho_1(\vec{w}_{0i,j}^+) + a_{i,j}^T(-z_{i,j})| \leq -a_{i,j}^T(-x_{i,j} - y_{i,j}).$$

For the reformulation of the condition with respect to $\rho_2^{(1)}(\vec{w}_{0i,j}^+)$, we get the following list.

- If the boundary values are in situation S1

$$|\rho_2^{(1)}(\vec{w}_{0i,j}^+) + b_{i,j}^T(-z_{i,j})| < -b_{i,j}^T(+x_{i,j} + y_{i,j}).$$

- If the situation of the boundary values is in the set \mathcal{S}_c

$$|\rho_2^{(1)}(\vec{w}_{0i,j}^+) + b_{i,j}^T(-z_{i,j})| \leq -b_{i,j}^T(-x_{i,j} - y_{i,j}).$$

- If the boundary values are in situation S9.7

$$|\rho_2^{(1)}(\vec{w}_{0i,j}^+) + b_{i,j}^T(-z_{i,j})| < -b_{i,j}^T(-x_{i,j} + y_{i,j}).$$

- If the situation of the boundary values is in the set \mathcal{S}_{ac}

$$|\rho_2^{(1)}(\vec{w}_{0i,j}^+) + b_{i,j}^T(-z_{i,j})| \leq -b_{i,j}^T(+x_{i,j} - y_{i,j}).$$

Finally, we obtain for the reformulation of the condition with respect to $\rho_2^{(2)}(\vec{w}_{0i,j}^+)$ the following list.

- If the boundary values are in situation S1

$$\rho_2^{(2)}(\vec{w}_{0i,j}^+) + \min \left\{ c_{i,j}^T(-x_{i,j} - y_{i,j} - z_{i,j}), \right. \\ \left. c_{i,j}^T(+x_{i,j} + y_{i,j} - z_{i,j}) \right\} > 0.$$

- If the situation of the boundary values is in the set \mathcal{S}_c or \mathcal{S}_{ac}

$$\rho_2^{(2)}(\vec{w}_{0i,j}^+) + \min \left\{ c_{i,j}^T(-x_{i,j} - y_{i,j} - z_{i,j}), \right. \\ c_{i,j}^T(+x_{i,j} - y_{i,j} - z_{i,j}), \\ c_{i,j}^T(-x_{i,j} + y_{i,j} - z_{i,j}), \\ \left. c_{i,j}^T(+x_{i,j} + y_{i,j} - z_{i,j}) \right\} > 0.$$

- If the boundary values are in situation S9.7

$$\rho_2^{(2)}(\vec{w}_{0i,j}^+) + \min \left\{ c_{i,j}^T (+x_{i,j} - y_{i,j} - z_{i,j}), \right. \\ \left. c_{i,j}^T (-x_{i,j} + y_{i,j} - z_{i,j}) \right\} > 0.$$

The reformulation of the conditions for the cases 18, 19, 20, 24 and 27 in Table 3.1 is done then similarly to the case 15 explained above.

Case 21. The last case which is left is case number 21. The corresponding region contains the part of the cube which was not covered so far with the corresponding regions of the other cases. Additionally, since it is unfortunately also possible that there are overlappings for some of the regions which appear at different faces, as for example the possible overlapping of region 1 with region 11, these overlappings are also assigned to case number 21 to finally achieve a proper partitioning.

One could get the impression that this handling of the overlappings is mathematically rather grubby, but to legitimate this we recall that an optimal solution of problem Eq. (3.25) will result in rather small values for $\rho_1(\vec{w}_{i,j}^+)$, $\rho_2^{(1)}(\vec{w}_{i,j}^+)$ and $\rho_2^{(2)}(\vec{w}_{i,j}^+)$ and therefore should be ideally close to case 21 in Table 3.1. Extending therefore the region for case number 21 should not be harmful. Furthermore, for small values of $\rho_1(\vec{w}_{i,j}^+)$, $\rho_2^{(1)}(\vec{w}_{i,j}^+)$ and $\rho_2^{(2)}(\vec{w}_{i,j}^+)$ a reformulation of the condition can lead more likely to overlappings of certain region parts. Therefore it seems to be adequate to assign these overlappings to region 21.

It is possible to define the region 21 in mathematical terms, but since we explained the content of this region already above this will be rather uninspiring and for the implementation an explicit formulation of the region is also not needed, since it can easily be depicted with the help of the other regions.

This concludes **Variant I** on how to solve Eq. (3.22) with the primal-dual approach.

Variant II

Now we describe a second variant on how to solve Eq. (3.22) with the primal-dual approach. First, note that similar as in Eq. (3.29), by using the definitions in Eq. (3.7), Eq. (3.8) and Eq. (3.9) and the notation in Eq. (3.27),

one can write $\rho_1(\vec{w}_{i,j}^+)$, $\rho_2^{(1)}(\vec{w}_{i,j}^+)$ and $\rho_2^{(2)}(\vec{w}_{i,j}^+)$ as

$$\begin{aligned}\rho_1(\vec{w}_{i,j}^+) &= a_{i,j}^T \vec{w}_{i,j}^+ + \kappa_{1i,j}, & \text{with } \kappa_{1i,j} &= \rho_1(\vec{w}_{0i,j}^+) - a_{i,j}^T \vec{w}_{0i,j}^+, \\ \rho_2^{(1)}(\vec{w}_{i,j}^+) &= b_{i,j}^T \vec{w}_{i,j}^+ + \kappa_{2i,j}, & \text{with } \kappa_{2i,j} &= \rho_2^{(1)}(\vec{w}_{0i,j}^+) - b_{i,j}^T \vec{w}_{0i,j}^+, \\ \rho_2^{(2)}(\vec{w}_{i,j}^+) &= c_{i,j}^T \vec{w}_{i,j}^+ + \kappa_{3i,j}, & \text{with } \kappa_{3i,j} &= \rho_2^{(2)}(\vec{w}_{0i,j}^+) - c_{i,j}^T \vec{w}_{0i,j}^+.\end{aligned}\quad (3.45)$$

Making use of Eq. (3.45) in Eq. (3.22) and comparing to Eq. (3.13), we see that we can choose the corresponding functions as

$$K : \begin{cases} X \rightarrow Y \\ \vec{w}^+ \mapsto K(\vec{w}^+) := (\nabla \vec{w}^+, g(b, \vec{w}^+), g(c, \vec{w}^+)) \end{cases},$$

with $g(s, \vec{w}^+)_{i,j} := s_{i,j}^T \vec{w}_{i,j}^+$ for $s, \vec{w}^+ \in X$, $i = 1, \dots, M$, $j = 1, \dots, N$,

$$\begin{aligned}F(\nabla \vec{w}^+, b^T \vec{w}^+, c^T \vec{w}^+) &= \mu \|\nabla \vec{w}^+\|_1 + \sum_{i,j} \gamma_2 \tilde{u}_{i,j} |\rho_2^{(1)}(\vec{w}_{i,j}^+)| + \sum_{i,j} \gamma_2 \tilde{u}_{i,j} |\rho_2^{(2)}(\vec{w}_{i,j}^+)| \\ &= \mu \|\nabla \vec{w}^+\|_1 + \sum_{i,j} \gamma_2 \tilde{u}_{i,j} |b_{i,j}^T \vec{w}_{i,j}^+ + \kappa_{2i,j}| + \sum_{i,j} \gamma_2 \tilde{u}_{i,j} |c_{i,j}^T \vec{w}_{i,j}^+ + \kappa_{3i,j}|,\end{aligned}$$

and

$$G(\vec{w}^+) = \sum_{i,j} \gamma_1 \tilde{u}_{i,j} |\rho_1(\vec{w}_{i,j}^+)|. \quad (3.46)$$

Recall, that this time we will use the space $Y = Y_2$, that was defined at the beginning of Section 3.4.2. For the purpose of simpler notation we define the variable

$$\begin{aligned}q_1 &:= (q^{(1)}, q^{(2)}, q^{(3)}, q^{(4)}), \\ \text{where } q &= (q^{(1)}, q^{(2)}, q^{(3)}, q^{(4)}, q^{(5)}, q^{(6)}) \in Y_2.\end{aligned}\quad (3.47)$$

The convex conjugate of F is given by

$$F^*(q) = F^*(q_1, q^{(5)}, q^{(6)}) = \begin{cases} -\langle \kappa_2, q^{(5)} \rangle_{\mathbb{R}^{MN}} - \langle \kappa_3, q^{(6)} \rangle_{\mathbb{R}^{MN}} & \text{if } q \in Q, \\ +\infty & \text{if } q \notin Q, \end{cases}$$

where

$$Q = \{q = (q_1, q^{(5)}, q^{(6)}) \in Y_2 \mid |q_{1i,j}| \leq \mu, |q_{i,j}^{(5)}| \leq \gamma_2 \tilde{u}_{i,j}, |q_{i,j}^{(6)}| \leq \gamma_2 \tilde{u}_{i,j}, \forall i = 1, \dots, M, j = 1, \dots, N\},$$

From the resolvent operator with respect to F^* we obtain then

$$q = (I + \sigma \partial F^*)^{-1}(\tilde{q}) \implies q_{1\ i,j} = \mu \frac{\tilde{q}_{1\ i,j}}{\max\{\mu, |\tilde{q}_{1\ i,j}|\}},$$

$$q_{i,j}^{(5)} = \begin{cases} 0 & \text{if } \gamma_2 \tilde{u}_{i,j} = 0, \\ \frac{\gamma_2 \tilde{u}_{i,j} (\tilde{q}_{i,j}^{(5)} + \sigma \kappa_{2\ i,j})}{\max\{\gamma_2 \tilde{u}_{i,j}, |\tilde{q}_{i,j}^{(5)} + \sigma \kappa_{2\ i,j}|\}} & \text{if } \gamma_2 \tilde{u}_{i,j} \neq 0, \end{cases}$$

and

$$q_{i,j}^{(6)} = \begin{cases} 0 & \text{if } \gamma_2 \tilde{u}_{i,j} = 0, \\ \frac{\gamma_2 \tilde{u}_{i,j} (\tilde{q}_{i,j}^{(6)} + \sigma \kappa_{3\ i,j})}{\max\{\gamma_2 \tilde{u}_{i,j}, |\tilde{q}_{i,j}^{(6)} + \sigma \kappa_{3\ i,j}|\}} & \text{if } \gamma_2 \tilde{u}_{i,j} \neq 0. \end{cases}$$

For the derivation of the resolvent operator with respect to G we look at the definition of G Eq. (3.46) and equation Eq. (3.15) and see that we have to solve

$$\begin{aligned} \bar{w}^+ &= (I + \tau \partial G)^{-1}(\bar{w}_0^+) \\ &= \arg \min_{\bar{w}^+ \in X} \left\{ \frac{\|\bar{w}^+ - \bar{w}_0^+\|_X^2}{2\tau} + G(\bar{w}^+) \right\} \\ &= \arg \min_{\bar{w}^+ = (u^+, v^+) \in X} \left\{ \frac{1}{2\tau} \sum_{i,j} \left((u_{i,j}^+ - u_{0\ i,j}^+)^2 + (v_{i,j}^+ - v_{0\ i,j}^+)^2 \right) \right. \\ &\quad \left. + \sum_{i,j} \gamma_1 \tilde{u}_{i,j} |\rho_1(\bar{w}_{i,j}^+)| \right\}. \end{aligned} \quad (3.48)$$

Finally, for $\tilde{u}_{i,j} = 0$ we can conclude again from Eq. (3.48) that $\bar{w}_{i,j}^+ = \bar{w}_{0\ i,j}^+$. On the other hand, for $\tilde{u}_{i,j} = 1$ the resolvent operator with respect to G leads again to a thresholding scheme similar as in [19, 92]. More precisely, when making use of the notations in Eq. (3.27), Eq. (3.28) and Eq. (3.33), we get

- If $a_{i,j} \neq \vec{0}$:

$$\bar{w}_{i,j}^+ = \bar{w}_{0\ i,j}^+ + \begin{cases} -x_{i,j} & \text{if } \rho_1(\bar{w}_{0\ i,j}^+) > a_{i,j}^T x_{i,j}, \\ x_{i,j} & \text{if } \rho_1(\bar{w}_{0\ i,j}^+) < -a_{i,j}^T x_{i,j}, \\ \alpha_1 a_{i,j} & \text{if } |\rho_1(\bar{w}_{0\ i,j}^+)| \leq a_{i,j}^T x_{i,j}. \end{cases}$$

- If $a_{i,j} = \vec{0}$:

$$\bar{w}_{i,j}^+ = \bar{w}_{0\ i,j}^+.$$

This concludes now **VARIANT II** on how to solve Eq. (3.22) with the primal-dual approach.

3.4.3 Resolvent Operators for Problem Eq. (3.12)

This section is very similar to Section 3.4.2 and we mainly have to just replace \vec{w}^+ by \vec{w}^- and \tilde{u} by $1 - \tilde{u}$. To achieve a smooth extension of \vec{w}^- to the domain Σ , we consider now instead of problem Eq. (3.12) the following problem

$$\min_{\vec{w}^-} \left\{ \int_{\Omega} f(\vec{w}^-) (1 - \tilde{u}(\vec{x})) + \mu s(\vec{w}^-) d\vec{x} \right\}. \quad (3.49)$$

The spaces X and $Y = Y_1$ (for **VARIANT I**) respectively $Y = Y_2$ (for **VARIANT II**) and their inner products are defined in the same way as in Section 3.4.2 and the discretisation of Eq. (3.49) is performed in the same manner as before. For **VARIANT I** the resolvent operator with respect to F^* is identical to Eq. (3.24) and for **VARIANT II** only slight changes appear. Finally, compared to the section before, there are also only very slight changes of the resolvent operator with respect to G for both, **VARIANT I** and **VARIANT II**.

3.5 Implementation

Although we have a convex minimisation problem with respect to the motion segmentation function \tilde{u} in Eq. (3.10) and partly linearised the fidelity term f in Eq. (3.6), we should keep in mind that the overall minimisation problem remains non-convex and that we have to update \vec{w}_0^+ and \vec{w}_0^- regularly. Therefore a coarse-to-fine strategy is applied to avoid the risk of getting stuck in a local minimum during the optimisation. The minimal size of the images at the coarsest level is set to $n_{min} = 32$ and the scaling factor for the pyramid to $\xi = 0.9$. At the coarsest level we initialise the displacement fields \vec{w}^+ and \vec{w}^- trivially with $\vec{0}$.

Because of the Remark in Section 3.2.2 one would expect, that the choice of the initialisation for the function \tilde{u} can be arbitrary. Indeed, whatever initialisation we choose, a global minimiser for the motion segmentation can be found for *fixed* \vec{w}^+ and \vec{w}^- . But in our case the values for \vec{w}^+ and \vec{w}^- are updated regularly during optimisation. Still a similar property has been observed during the experiments, by choosing different initialisations for \tilde{u} . See for example Fig. 3.11.

The final iteration scheme consists of two loops. The outer loop iterates over the pyramid levels. In each level an inner loop updates the values for \tilde{u} , \vec{w}^+ and \vec{w}^- , following steps 1 - 3 in Section 3.3.1. Thus, in each iteration of this inner loop one step of the primal-dual Algorithm 1 from [20] is performed with the appropriate resolvent operators from the previous sections to update \tilde{u} , \vec{w}^+ and \vec{w}^- . To achieve a better convergence of \tilde{u} we

update \vec{w}^+ and \vec{w}^- only every 50th iteration. The motion segmentation Σ is obtained by choosing $\eta = 0.5$ and setting $\Sigma = \Sigma(\eta) := \{\vec{x} \in \Omega \mid \tilde{u}(\vec{x}) \geq \eta\}$ (see Remark in Section 3.2.2).

As soon as the finest level is reached, the inner loop is executed until a certain tolerance or the maximum number of iterations is reached. The final displacement field is then obtained by setting

$$\vec{w}(\vec{x}) = \begin{cases} \vec{w}^+(\vec{x}) & \text{if } \vec{x} \in \Sigma, \\ \vec{w}^-(\vec{x}) & \text{if } \vec{x} \in \Omega \setminus \Sigma. \end{cases}$$

Bicubic interpolation is used to calculate the images $T(\vec{x} + \vec{w}^\pm)$ during the iterations and to obtain the final registered image $T(\vec{x} + \vec{w})$.

3.6 Results

In order to show the performance of the proposed method, we show qualitative and quantitative results.

For the results shown in Fig. 3.9, Fig. 3.10, Fig. 3.11, Fig. 3.12 and Fig. 3.13 we used **VARIANT I** of our method. Both variants of our method were used in the quantitative evaluation (Fig. 3.14) and the running time comparison (Table 3.4).

In Fig. 3.9, we show the registration result of a synthetic example, where a textured circle is moving down diagonally. We illustrate in Fig. 3.10 the evolution of the motion segmentation \tilde{u} with the corresponding histograms. Starting from the initial value, in this case we used the reference image, the final result becomes close to binary, as expected.

Although our energy functional is convex with respect to the motion segmentation function \tilde{u} , the overall minimisation task remains a non-convex problem. To decrease the influence of the non-convexity during the minimisation procedure, certain terms are linearised and a coarse-to-fine strategy is applied. Experiments for the synthetic example in Fig. 3.9 show, that due to this workaround different initialisation for \tilde{u} could be used to achieve similar results, as shown in Fig. 3.11.

In order to show the effect of the smoothness parameter ν for the TV of \tilde{u} , we show in Fig. 3.12 that we can obtain smoother results as ν increases.

Since we are interested in the discontinuities of the displacement field, we compare the proposed method to methods that are able to preserve discontinuities in the displacement field, in this case, the demon algorithm with anisotropic diffusion filtering [26], the registration algorithm of Brox *et al.* [16] and our previous work [49].

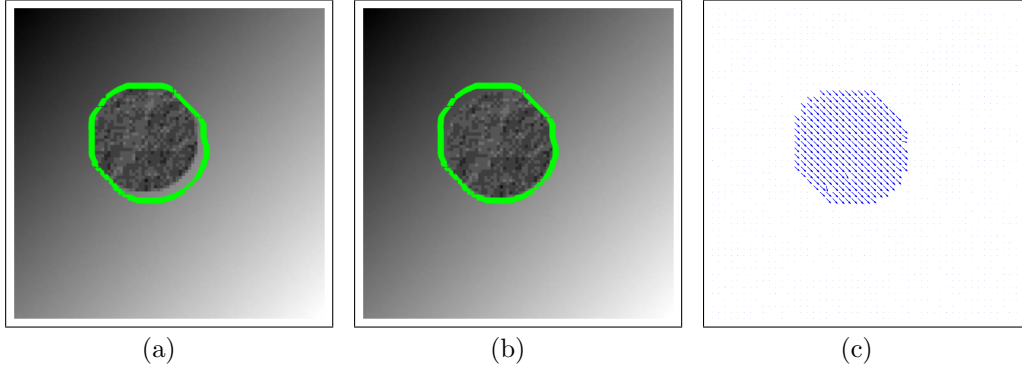


Figure 3.9: The template (a) and the reference (b) images superimposed with the motion segmentation (green curves), and the displacement field \vec{w} (c). The parameter values used for this example are $\gamma_1 = 4$, $\gamma_2 = 4$, $\mu = 0.5$, and $\nu = 0.3$.

We show the qualitative comparison in Fig. 3.13. As clearly seen, the proposed method can achieve more crisp discontinuities in the displacement field compared to the demon algorithm with anisotropic diffusion filtering and the registration algorithm of Brox *et al.* Furthermore, the proposed method managed nicely to separate the motion of the abdominal wall and the one of the organs.

In Fig. 3.14 a quantitative evaluation is shown for 22 different liver image pairs. We chose the parameters for all the methods by optimising them with respect to these image pairs. The parameters of our method were set to $\gamma_1 = 4$, $\gamma_2 = 1$, $\mu = 0.2$ and $\nu = 0.1$ for **VARIANT I** and **VARIANT II**. For the demon algorithm with anisotropic diffusion filtering we could use the suggested parameters, for Brox *et al.*'s method we used $\gamma = 5$, $\alpha = 80$ and $\sigma = 0.9$ and finally for our previous method we used the parameters suggested there, namely $\gamma = 0.4$, $\mu = 0.05$, $\nu = 20$, $\theta = 0.2$ and $\epsilon = 0.00001$.

To quantitatively assess the performance of the methods, we calculated the mean squared error (MSE) and the normalised mutual information (NMI), with the grey values scaled from 0 to 1. For all our examples the proposed method performed better than the demon algorithm with anisotropic diffusion and the registration algorithm of Brox *et al.* We used the Kolmogorov-Smirnov test to check for normality of the results using the R Software package (Version 2.10.1). We considered a significance level of 5% as significant. The t-test showed that the proposed method delivered significantly better results than the demon algorithm with anisotropic diffusion filtering and the method of Brox *et al.* with both $p < 0.05$. The proposed method produced more satisfying results compared to our previous method [49] for the MSE

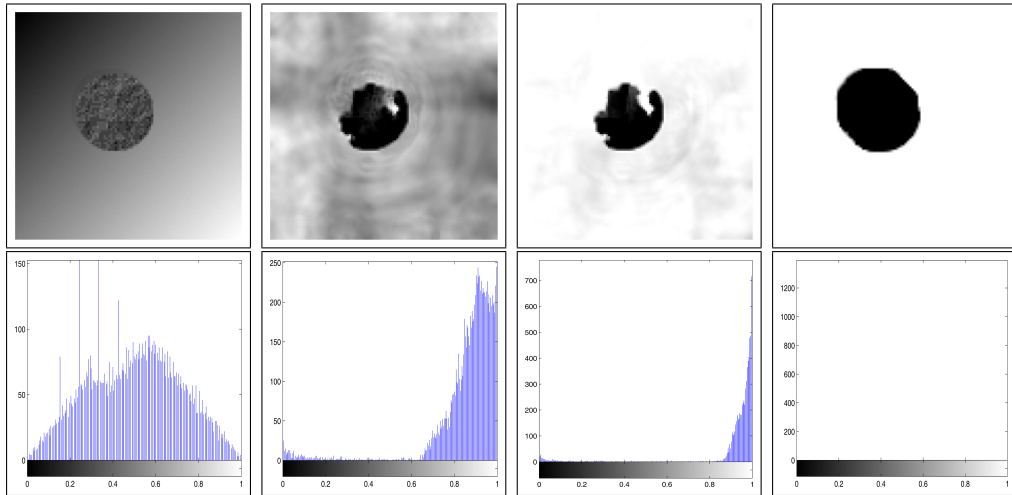


Figure 3.10: *From left to right:* The evolution of the motion segmentation function \tilde{u} (*top row*) with the corresponding histograms (*bottom row*) for the example and parameters in Fig. 3.9. Note that the reference image is used for the initialisation of \tilde{u} .

and NMI.

In a next step we compared the running times of the proposed method (**VARIANT I** and **VARIANT II**) to the ones of our previous work [49] for the 22 liver image pairs. Both methods were implemented in MATLAB and the experiments were performed on a 64-bit Linux system with 1.2 GHz. We used again the parameters $\gamma_1 = 4$, $\gamma_2 = 1$, $\mu = 0.2$ and $\nu = 0.1$ for both of the variants of the proposed method and for our previous work the parameters $\gamma = 0.4$, $\mu = 0.05$, $\nu = 20$, $\theta = 0.2$ and $\epsilon = 0.00001$. In [49] the displacement fields \vec{w}^+ and \vec{w}^- were updated each 10th iteration. To provide a fair comparison, we therefore used the same update frequency for the proposed new method. Furthermore, the maximum number of iterations in the finest level is set to 30000 for both methods. The timing results for the 22 liver image pairs are shown in Table 3.4 together with the mean and standard deviation. The running times of both methods are comparable. By using **VARIANT I**, the proposed new method performed with around 100 s slightly faster than the old method. Here, we want to mention that the old method makes use of some optimized in-built MATLAB routines, whereas for the proposed method there is still a high potential to optimise the code. Despite this, when using **VARIANT II**, the proposed new method got even about three times faster than the old method.

3.7 Conclusion

In this chapter we presented a primal-dual method for discontinuity preserving non-rigid registration, that makes use of the continuous cuts framework. The so gained motion segmentation influences the motion estimation positively by sharpening the discontinuities in the displacement field. The minimisation of the energy functional is implemented in a coarse-to-fine strategy and exploits the rapidity of the primal-dual algorithm studied in [20]. The experimental results demonstrated desirable performance of the proposed method in comparison with those of the demon algorithm with anisotropic diffusion filtering [26] and the registration algorithm of Brox *et al.* [16].

Large displacements of deforming organs can cause misregistrations even when using a coarse-to-fine approach. Brox and Malik proposed in a very recent publication [18] to include point correspondences from descriptor matching into the variational optical flow formulation. In future work we plan on similarly including known corresponding landmarks into the functional as hard constraints. However, we plan on using our *Tracking the Invisible* approach [41] for locating the matching point correspondences.

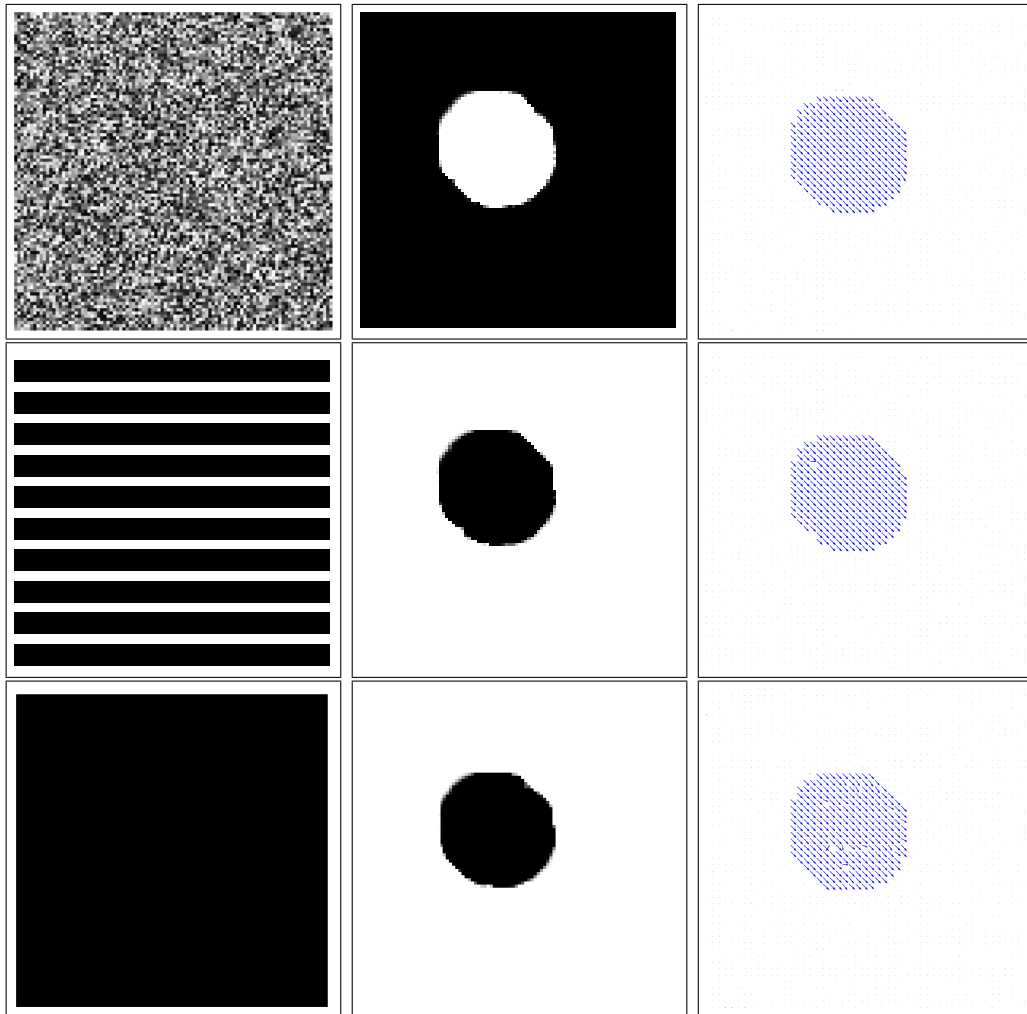


Figure 3.11: The motion segmentation results \tilde{u} (*middle column*) and the corresponding displacement field results \vec{w} (*right column*) obtained when using different initialisations for \tilde{u} (*left column*) for the example and parameters in Fig. 3.9. For the results in Fig. 3.9 itself the reference image was used for initialisation.

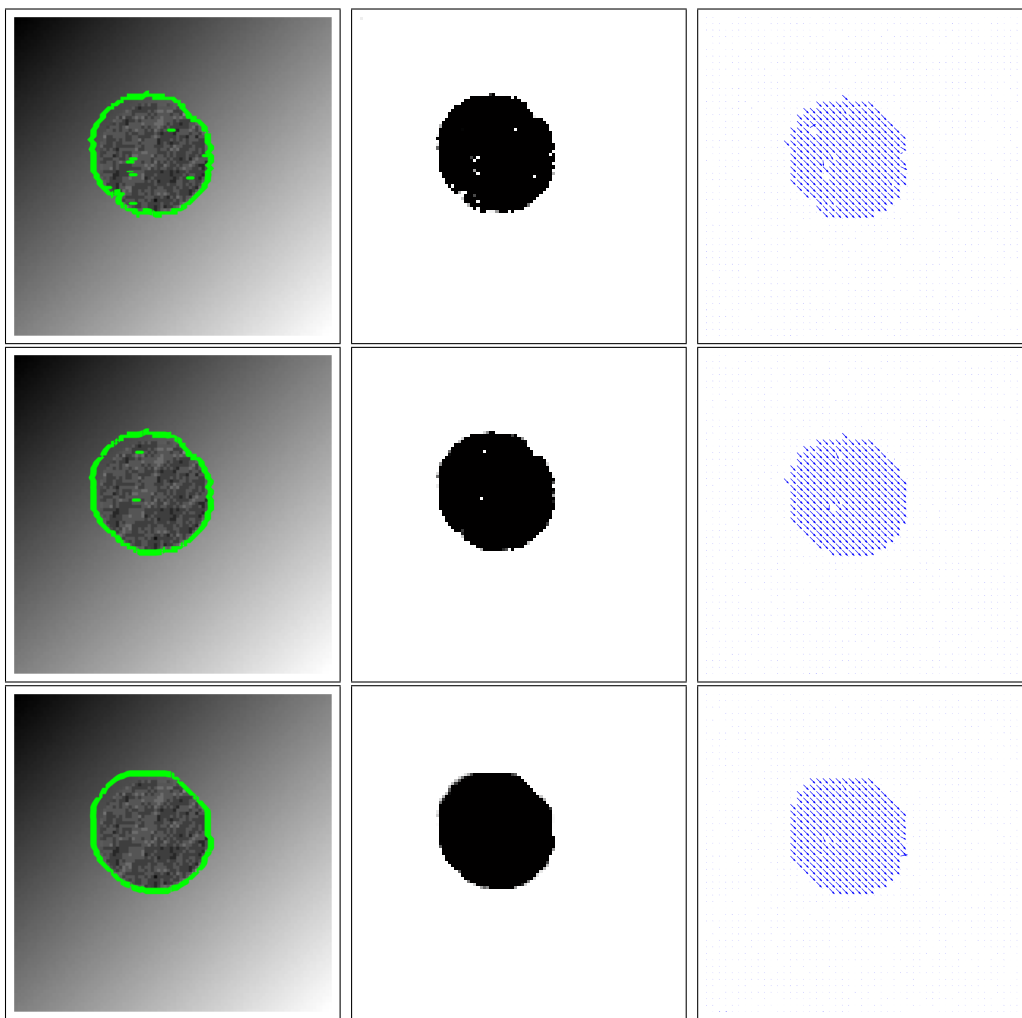


Figure 3.12: *From top to down:* The effect of the smoothness parameter ν when $\nu = 0.01, 0.05, 0.2$. Here we show the reference image superimposed with the contour of thresholded motion segmentation \tilde{u} (*left column*), \tilde{u} (*middle column*) and the corresponding displacement field \vec{w} (*right column*) for the example in Fig. 3.9. The other parameters are again $\gamma_1 = 4$, $\gamma_2 = 4$ and $\mu = 0.5$.

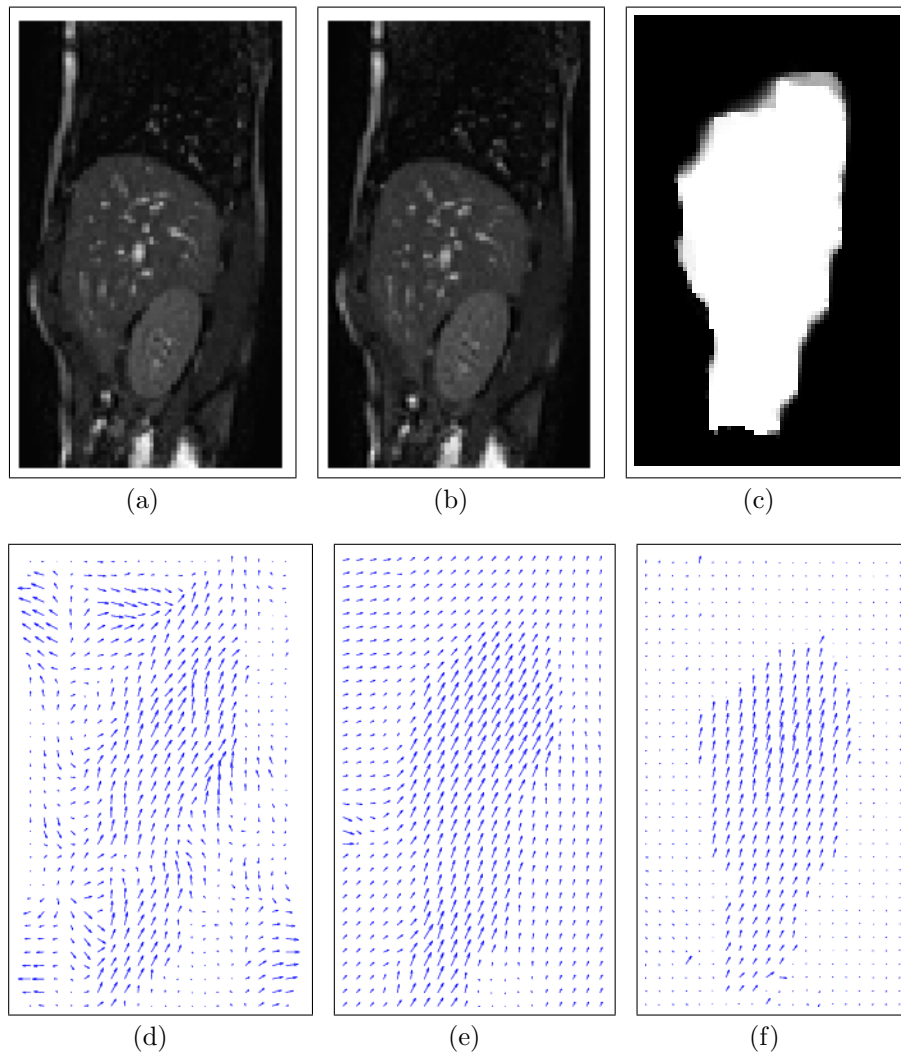
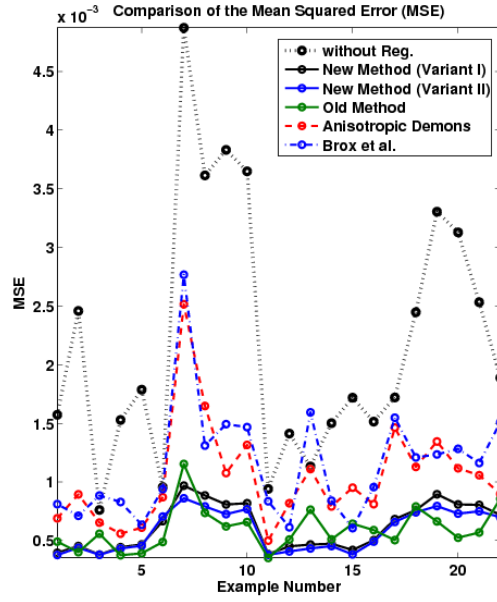
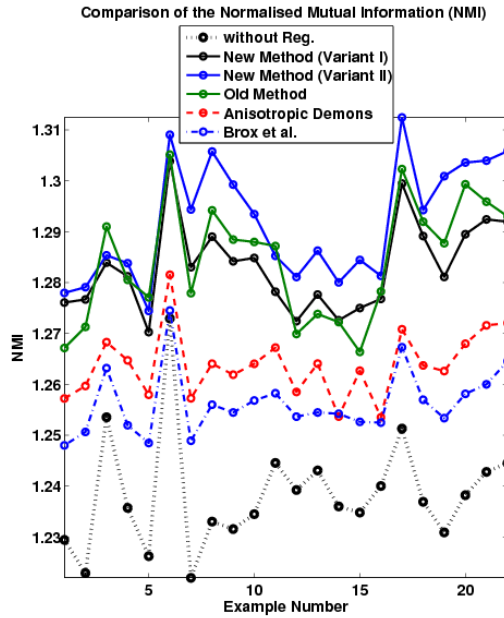


Figure 3.13: The template image (a), the reference image (b) and the motion segmentation result (c). The displacement field for the demon algorithm with anisotropic diffusion filtering is shown in (d), the one for the registration algorithm of Brox *et al.* in (e) and finally the one of our method in (f).



(a)



(b)

Figure 3.14: Quantitative evaluation for 22 pairs of liver images with a discontinuous displacement field. Comparison of the MSE (a) and NMI (b).

Table 3.4: Comparison of the running times of the proposed method (**Variante I** and **Variante II**) to the ones of our previous work [49] for 22 liver image pairs. The times are given in seconds.

Ex. No.	Previous Method [49]	Proposed New Method (Variante I)	Proposed New Method (Variante II)
1	1055.13	959.33	325.69
2	1053.55	951.41	328.68
3	1060.33	948.92	327.09
4	1059.57	996.78	323.51
5	1052.58	951.85	323.14
6	1064.84	955.43	330.34
7	1070.07	990.57	327.49
8	1060.53	944.11	323.82
9	1082.90	949.47	326.78
10	1079.99	949.23	324.44
11	1073.25	954.15	324.34
12	1048.56	961.26	324.29
13	1059.35	956.23	328.40
14	1061.09	949.74	323.45
15	1065.24	952.35	329.92
16	1072.26	949.80	330.28
17	1075.99	980.85	328.35
18	1068.88	951.10	326.22
19	1071.08	985.62	329.86
20	1064.42	949.60	329.71
21	1057.28	946.05	327.17
22	1060.19	979.33	331.26
mean	1064.41	959.69	327.01
std	9.03	15.76	2.62

Chapter 4

A Landmark-Based Primal-Dual Approach for Discontinuity Preserving Registration through Motion Segmentation with Continuous Cuts

The content of this chapter has been published in [51]. It is an extension of the work presented in [50] (see Chapter 3) for **Variant I**. The extension for **Variant II** works similarly.

Discontinuous motion is quite common in the medical field as for example in the case of breathing induced organ motion. Registration methods that are able to preserve discontinuities are therefore of special interest. To achieve this goal we developed in our previous work a framework that combines motion segmentation and registration. To avoid unreliable motion fields the incorporation of landmark correspondences can be a remedy. We therefore describe in this chapter how we integrate the landmarks into our variational approach and how to solve the minimisation problem with a primal-dual algorithm. Qualitative and quantitative results are shown for real MR images of breathing induced liver motion.

4.1 Introduction

Nowadays, image registration is an indispensable tool for many medical applications and a great variety of well established methods have been proposed. Although image registration has been a topic of high interest in the last decades, methods that can handle discontinuous motion fields have only drawn little attention until recently. This despite its importance when for example registering abdominal organs that undergo breathing induced motion.

More attention to discontinuity preserving methods is being paid in the related research field of optical flow. Important theoretical contributions also originate from image segmentation and image denoising methods. Mumford and Shah for example proposed in their pioneering work [60] a functional for image segmentation that avoids spatial smoothing in certain locations of the image, thus preserving discontinuities. Vese and Chan [84] introduced a level set framework based approach to efficiently solve the Mumford and Shah minimisation problem for segmentation. Another influential approach based on the total variation (TV), known to preserve discontinuities, was proposed by Rudin *et al.* [71] for image denoising. The beneficial behaviour of the TV was also exploited in image segmentation, image registration and optical flow methods, as for example in [21], [67] and [16].

A recent registration approach that tries to handle discontinuities in the displacement field of medical images has been proposed by Schmidt-Richberg *et al.* [73], which considers a direction-dependent regularisation method of the displacement field. This method relies on the calculation of the normals at the object boundaries and therefore a rather good manual segmentation has to be provided in advance.

As shown in the work of Amiaz and Kiryati [5], where the optical flow method of Brox *et al.* [16] was embedded into the segmentation framework of Vese and Chan [84], the so achieved motion segmentation can influence the registration process positively. Instead of using the level set formulation, we used in our previous works [49, 50] (see Chapter 2 and 3) the segmentation framework of Chan *et al.* [21] that guarantees a globally optimal motion segmentation result for a fixed motion field. A preliminary short version of the work in [50] can be found in [52]. Following the work of Chambolle and Pock [20] we solved then the registration problem with a primal-dual approach.

To avoid unreliable motion fields, we incorporate in this chapter the information of landmarks into our previous work [50]. There exist many image registration methods which integrate the information of landmark correspondences, as for example [42, 48, 53, 65, 18]. Here, we will make use of the re-

cent work of Brox and Malik [18], which contains the idea on how to include descriptor matchings, respectively landmark correspondences, easily into a variational framework.

4.2 Method

In the following we want to describe the proposed method. First, we shortly recapitulate the registration and motion segmentation framework we used already before in [50] (see Chapter 3) and in a second part we discuss the incorporation of the landmarks into the energy functional.

4.2.1 Registration and Motion Segmentation Framework

We define by $\Omega \subset \mathbb{R}^2$ the domain of the pixel positions $\vec{x} = (x_1, x_2)$ and by the functions $R : \Omega \rightarrow \mathbb{R}$ and $T : \Omega \rightarrow \mathbb{R}$ our reference and template image. The aim of image registration is to find a transformation $\Phi(\vec{x}) := \vec{x} + \vec{w}(\vec{x})$ such that the relation $T \circ \Phi \approx R$ holds and the displacement field $\vec{w} : \Omega \rightarrow \mathbb{R}^2$, where $\vec{w}(\vec{x}) := (u(\vec{x}), v(\vec{x}))$ with $u, v : \Omega \rightarrow \mathbb{R}$, will be the function we focus at. For convenience we will use the abbreviations \vec{w} , u and v for $\vec{w}(\vec{x})$, $u(\vec{x})$ and $v(\vec{x})$.

The proposed registration method integrates the displacement field estimation into the convex segmentation method of Chan *et al.* [21] to preserve the discontinuities in the displacement field. The energy functional for this variational approach is given by

$$\begin{aligned} E(\vec{w}^+, \vec{w}^-, \tilde{u}) &= \int_{\Omega} D(\vec{w}^+) \tilde{u}(\vec{x}) d\vec{x} + \int_{\Omega} D(\vec{w}^-) (1 - \tilde{u}(\vec{x})) d\vec{x} \\ &+ \nu \int_{\Omega} |\nabla \tilde{u}(\vec{x})| d\vec{x}. \end{aligned} \quad (4.1)$$

Here, the function D represents the data term and is of the general form $D(\vec{w}) := f(\vec{w}) + \mu s(\vec{w})$, where f and s are the fidelity term and the smoothness term with $\mu \in \mathbb{R}^+$ being a weighting parameter. We choose a fidelity term f that incorporates the constraints for the grey value constancy and the gradient constancy with their corresponding weights $\gamma_1, \gamma_2 \in \mathbb{R}_0^+$. Therefore we define

$$\begin{aligned} f(\vec{w}) = f(u, v) &:= \gamma_1 |T(\vec{x} + \vec{w}) - R(\vec{x})| \\ &+ \gamma_2 |\partial_{x_1} T(\vec{x} + \vec{w}) - \partial_{x_1} R(\vec{x})| \\ &+ \gamma_2 |\partial_{x_2} T(\vec{x} + \vec{w}) - \partial_{x_2} R(\vec{x})|. \end{aligned} \quad (4.2)$$

The smoothness term s results in the L^1 -norm respectively the vectorial TV of \vec{w} and is given by

$$s(\vec{w}) = s(u, v) := \sqrt{|\nabla u|^2 + |\nabla v|^2} = |\nabla \vec{w}|. \quad (4.3)$$

Furthermore, to incorporate Chan *et al.*'s work [21], a binary function $\tilde{u} : \mathbb{R}^2 \rightarrow \{0, 1\}$, $\tilde{u}(\vec{x}) := \mathbf{1}_\Sigma(\vec{x})$, where $\Sigma \subseteq \Omega \subset \mathbb{R}^2$ with $\Sigma := \{\vec{x} \in \Omega \mid \tilde{u}(\vec{x}) = 1\}$, is used in Eq. (4.1) to differentiate the displacement field \vec{w} into \vec{w}^+ and \vec{w}^- . Finally, the last term in the above energy Eq. (4.1) is a regularisation defined by the TV and weighted by a parameter $\nu \in \mathbb{R}^+$.

The registration problem is solved by minimising energy E in Eq. (4.1) with respect to \vec{w}^+ , \vec{w}^- and \tilde{u} and we finally obtain the aimed displacement field by setting $\vec{w} := \vec{w}^+ \tilde{u} + \vec{w}^- (1 - \tilde{u})$.

As pointed out by Chan *et al.* in [21], Eq. (4.1) is strongly related to the Mumford-Shah functional [60] and one can show that a global minimiser of the set Σ can be found by minimising energy E in Eq. (4.1) with respect to \tilde{u} over a convex set and finally thresholding the so obtained result. (See Theorem 1.4 in Section 1.4.2.)

4.2.2 Incorporation of the Landmarks

To exploit the information of the landmarks in the proposed variational registration method we make use of Brox and Malik's approach [18]. The landmark point correspondences, which are defined by the vectors $\vec{w}_{LM} = (u_{LM}, v_{LM})$, should act as a prior to the displacement field \vec{w} and we therefore seek to additionally minimise an energy of the form

$$E_{LM}(\vec{w}) = \int_{\Omega} \mathbf{1}_S(\vec{x}) |\vec{w}(\vec{x}) - \vec{w}_{LM}(\vec{x})|_2^2 d\vec{x},$$

where S is the set of the landmark positions in the reference image R . More specifically, incorporating energy E_{LM} into our registration and motion segmentation framework defined by the energy functional E in Eq. (4.1) results in a modified fidelity term f in Eq. (4.2), namely

$$\begin{aligned} f(\vec{w}) := & \gamma_1 |T(\vec{x} + \vec{w}) - R(\vec{x})| + \gamma_2 |\partial_{x_1} T(\vec{x} + \vec{w}) - \partial_{x_1} R(\vec{x})| \\ & + \gamma_2 |\partial_{x_2} T(\vec{x} + \vec{w}) - \partial_{x_2} R(\vec{x})| + \frac{1}{2} \lambda \mathbf{1}_S(\vec{x}) |\vec{w}(\vec{x}) - \vec{w}_{LM}(\vec{x})|_2^2, \end{aligned} \quad (4.4)$$

where $\lambda \in \mathbb{R}^+$ is a weighting parameter. Instead of using a dense correspondence field [18], we use the landmarks extracted by the Affine Scale Invariant Feature Transform (A-SIFT) method [91], a recently developed algorithm

that extends the well known SIFT method [56] and allows landmark matching under affine deformations, hence usually finding a lot more matches than the SIFT method. The putative matches found are then filtered by fitting a homography to the matches using RANSAC [31] yielding the set S of landmark positions.

4.3 Minimisation

4.3.1 Iterative Scheme

To facilitate the minimisation procedure we replace the fidelity term f in Eq. (4.4) by its partly linearised version

$$f(\vec{w}) = \gamma_1 |\rho_1(\vec{w})| + \gamma_2 |\rho_2^{(1)}(\vec{w})| + \gamma_2 |\rho_2^{(2)}(\vec{w})| + \frac{1}{2} \lambda \mathbf{1}_S(\vec{x}) |\vec{w}(\vec{x}) - \vec{w}_{LM}(\vec{x})|_2^2, \quad (4.5)$$

where

$$\rho_1(\vec{w}) := T(\vec{x} + \vec{w}_0) + \nabla T(\vec{x} + \vec{w}_0)^T (\vec{w} - \vec{w}_0) - R(\vec{x}), \quad (4.6)$$

$$\rho_2^{(1)}(\vec{w}) := \partial_{x_1} T(\vec{x} + \vec{w}_0) + \begin{pmatrix} \partial_{x_1 x_1} T(\vec{x} + \vec{w}_0) \\ \partial_{x_2 x_1} T(\vec{x} + \vec{w}_0) \end{pmatrix}^T (\vec{w} - \vec{w}_0) - \partial_{x_1} R(\vec{x}), \quad (4.7)$$

and

$$\rho_2^{(2)}(\vec{w}) := \partial_{x_2} T(\vec{x} + \vec{w}_0) + \begin{pmatrix} \partial_{x_1 x_2} T(\vec{x} + \vec{w}_0) \\ \partial_{x_2 x_2} T(\vec{x} + \vec{w}_0) \end{pmatrix}^T (\vec{w} - \vec{w}_0) - \partial_{x_2} R(\vec{x}). \quad (4.8)$$

The minimisation of the energy functional E with respect to \vec{w}^+ , \vec{w}^- and \tilde{u} is then performed by the following iterative scheme:

1. For fixed \vec{w}^+ and \vec{w}^- , solve

$$\min_{\tilde{u} \in [0,1]} \left\{ \int_{\Omega} D(\vec{w}^+) \tilde{u}(\vec{x}) d\vec{x} + \int_{\Omega} D(\vec{w}^-) (1 - \tilde{u}(\vec{x})) d\vec{x} + \nu \int_{\Omega} |\nabla \tilde{u}(\vec{x})| d\vec{x} \right\}. \quad (4.9)$$

2. For fixed \tilde{u} , solve

$$\min_{\vec{w}^+} \left\{ \int_{\Omega} D(\vec{w}^+) \tilde{u}(\vec{x}) d\vec{x} \right\}. \quad (4.10)$$

3. For fixed \tilde{u} , solve

$$\min_{\vec{w}^-} \left\{ \int_{\Omega} D(\vec{w}^-) (1 - \tilde{u}(\vec{x})) d\vec{x} \right\}. \quad (4.11)$$

To solve the subproblems Eq. (4.9), Eq. (4.10) and Eq. (4.11) in a fast and efficient way, we follow a primal-dual approach as described by Chambolle and Pock in [20]. We therefore recapitulate in the next section the basic notations and formulations.

4.3.2 The Primal-Dual Approach of Chambolle and Pock

First, we define by X and Y two finite-dimensional real vector spaces. Their inner products are denoted by $\langle \cdot, \cdot \rangle_X$ respectively $\langle \cdot, \cdot \rangle_Y$ and their induced norms are given by $\|\cdot\|_X = \sqrt{\langle \cdot, \cdot \rangle_X}$ respectively $\|\cdot\|_Y = \sqrt{\langle \cdot, \cdot \rangle_Y}$. The general non-linear primal problem we have is of the form

$$\min_{x \in X} F(Kx) + G(x),$$

where $F : Y \rightarrow [0, +\infty)$ and $G : X \rightarrow [0, +\infty)$ are proper, convex and lower semi-continuous and the map $K : X \rightarrow Y$ is a continuous linear operator. The corresponding primal-dual formulation is the saddle-point problem

$$\min_{x \in X} \max_{y \in Y} \langle Kx, y \rangle_Y + G(x) - F^*(y),$$

with $F^* : Y \rightarrow \mathbb{R} \cup \{+\infty\}$ being the convex conjugate of F . We assume that the problems above have at least one solution $(\hat{x}, \hat{y}) \in X \times Y$ and therefore it holds $K\hat{x} \in \partial F^*(\hat{y})$ and $-(K^*\hat{y}) \in \partial G(\hat{x})$, where $\partial F^*(\hat{y})$ and $\partial G(\hat{x})$ are the subdifferentials of the convex functions F^* at \hat{y} and G at \hat{x} . Furthermore we assume that F and G are “simple”, *i.e.* that the resolvent operators $(I + \sigma \partial F^*)^{-1}$ and $(I + \tau \partial G)^{-1}$, with $\sigma, \tau \in \mathbb{R}^+$ small enough, are easy to compute. For a convex function f the resolvent of the operator $\tau \partial f$ at \tilde{x} can be calculated in our case by

$$x = (I + \tau \partial f)^{-1}(\tilde{x}) = \arg \min_x \left\{ \frac{\|x - \tilde{x}\|^2}{2\tau} + f(x) \right\}. \quad (4.12)$$

We will only make use of Algorithm 1 in [20] with the extrapolation parameter $\theta = 1$. The usage of the other proposed algorithms is left for the moment for later research.

To apply Algorithm 1 in [20] to the minimisation problems Eq. (4.9), Eq. (4.10) and Eq. (4.11), we first need to rewrite them in their discretised version, then identify the functions F and G and finally derive the resolvent operators $(I + \sigma \partial F^*)^{-1}$ and $(I + \tau \partial G)^{-1}$.

For the discrete setting we therefore define by $\vec{x}_{i,j} = (x_{1i,j}, x_{2i,j}) = (ih, jh)$, $i = 1, \dots, M$, $j = 1, \dots, N$, the pixel positions in the image domain with h being the spatial step size. For the calculations of the finite differences, the discrete divergence operator, the discretised inner products and further details we refer the reader to [20] and the references therein.

In the following sections we will discuss the resolvent operators for the three given minimisation problems Eq. (4.9), Eq. (4.10) and Eq. (4.11). The formulation of the resolvent operators does not change much with respect to our previous work in [50]. We nevertheless recapitulate them in the following sections and point out the certain changes which appear.

4.3.3 Resolvent Operators for Problem Eq. (4.9)

Let us consider the continuous problem Eq. (4.9). After its discretisation and some calculations we get

$$p = (I + \sigma \partial F^*)^{-1}(\tilde{p}) \implies p_{i,j} = \nu \frac{\tilde{p}_{i,j}}{\max\{\nu, |\tilde{p}_{i,j}|\}},$$

as a solution of the resolvent operator with respect to F^* . This is the same result we got in [50] and the calculations are performed in the same way as there. The resolvent operator with respect to G is also derived similar as in [50] and is given by

$$\tilde{u} = (I + \tau \partial G)^{-1}(\hat{u}) \implies \tilde{u}_{i,j} = \min\{\max\{\hat{u}_{i,j} - \tau (D(\vec{w}_{i,j}^+) - D(\vec{w}_{i,j}^-)), 0\}, 1\}.$$

Note that the data term D , or more specifically the fidelity term f that appears in D , is not the same as in our previous work. This time it additionally incorporates the information of the landmarks.

4.3.4 Resolvent Operators for Problem Eq. (4.10)

Now we consider the continuous problem Eq. (4.10). The numerical calculations in the implementation get facilitated by having a smooth extension of \vec{w}^+ to the domain $\Omega \setminus \Sigma$. We therefore consider instead the problem

$$\min_{\vec{w}^+} \left\{ \int_{\Omega} f(\vec{w}^+) \tilde{u}(\vec{x}) + \mu s(\vec{w}^+) d\vec{x} \right\}. \quad (4.13)$$

Comparing Eq. (4.10) to Eq. (4.13) the only difference is, that the factor \tilde{u} is not applied to the smoothness term s anymore.

From the resolvent operator with respect to F^* we obtain this time

$$q = (I + \sigma \partial F^*)^{-1}(\tilde{q}) \implies q_{i,j} = \mu \frac{\tilde{q}_{i,j}}{\max\{\mu, |\tilde{q}_{i,j}|\}}. \quad (4.14)$$

This is again the same result as in [50] but more changes appear instead in the solution for resolvent operator with respect to G . This time the function G incorporates the information of the landmarks and is given by

$$G(\vec{w}^+) = \sum_{i,j} \left(\gamma_1 |\rho_1(\vec{w}_{i,j}^+)| + \gamma_2 |\rho_2^{(1)}(\vec{w}_{i,j}^+)| + \gamma_2 |\rho_2^{(2)}(\vec{w}_{i,j}^+)| \right. \\ \left. + \frac{1}{2} \lambda \mathbf{1}_S(\vec{x}_{i,j}) \left((u_{i,j}^+ - u_{LM\ i,j})^2 + (v_{i,j}^+ - v_{LM\ i,j})^2 \right) \right) \tilde{u}_{i,j}. \quad (4.15)$$

The derivation of the resolvent operator with respect to G is again not that straightforward and more effort has to be put in to find a suitable solution. This can be done similar as in [50] and therefore, having a closer look at the definition of G Eq. (4.15) and equation Eq. (4.12), we see that we have to solve

$$\vec{w}^+ = (I + \tau \partial G)^{-1}(\vec{w}_0^+) = \arg \min_{\vec{w}^+ \in X} \left\{ \frac{\|\vec{w}^+ - \vec{w}_0^+\|_X^2}{2\tau} + G(\vec{w}^+) \right\} \\ = \arg \min_{\vec{w}^+ = (u^+, v^+) \in X} \left\{ \frac{1}{2\tau} \sum_{i,j} \left((u_{i,j}^+ - u_{0\ i,j}^+)^2 + (v_{i,j}^+ - v_{0\ i,j}^+)^2 \right) \right. \\ \left. + \sum_{i,j} \left(\gamma_1 |\rho_1(\vec{w}_{i,j}^+)| + \gamma_2 |\rho_2^{(1)}(\vec{w}_{i,j}^+)| + \gamma_2 |\rho_2^{(2)}(\vec{w}_{i,j}^+)| \right) \right. \\ \left. + \frac{1}{2} \lambda \mathbf{1}_S(\vec{x}_{i,j}) \left((u_{i,j}^+ - u_{LM\ i,j})^2 + (v_{i,j}^+ - v_{LM\ i,j})^2 \right) \right\} \tilde{u}_{i,j}. \quad (4.16)$$

Similar to the work in [50] for $\tilde{u}_{i,j} = 0$ we can conclude from Eq. (4.16) that $\vec{w}_{i,j}^+ = \vec{w}_{0\ i,j}^+$. On the other hand, for $\tilde{u}_{i,j} = 1$ we have again to distinguish the cases

$$\rho_1(\vec{w}_{i,j}^+) \begin{pmatrix} \geq \\ \leq \\ = \end{pmatrix} 0, \quad \rho_2^{(1)}(\vec{w}_{i,j}^+) \begin{pmatrix} \geq \\ \leq \\ = \end{pmatrix} 0, \quad \rho_2^{(2)}(\vec{w}_{i,j}^+) \begin{pmatrix} \geq \\ \leq \\ = \end{pmatrix} 0, \quad (4.17)$$

which turn out to be 27 in total. The additional term of the landmarks will cause slight changes in the resolvent operator with respect to G that we used to have before in [50]. Nevertheless, the idea of the derivation of the explicit solutions for $\vec{w}_{i,j}^+$ and the reformulations of the conditions in Eq. (4.17) remains the same.

4.3.5 Resolvent Operators for Problem Eq. (4.11)

This section is very similar to Section 4.3.4 and we mainly have to just replace \vec{w}^+ by \vec{w}^- and \tilde{u} by $1 - \tilde{u}$. To achieve a smooth extension of \vec{w}^- to the domain Σ , we consider now instead of problem Eq. (4.11) the following problem

$$\min_{\vec{w}^-} \left\{ \int_{\Omega} f(\vec{w}^-) (1 - \tilde{u}(\vec{x})) + \mu s(\vec{w}^-) d\vec{x} \right\}. \quad (4.18)$$

The resolvent operator with respect to F^* is identical to Eq. (4.14) and compared to the section before only very slight changes of the resolvent operator with respect to G have to be done.

4.4 Results

The minimisation problems for the displacement fields \vec{w}^+ and \vec{w}^- remain non-convex, although we have a convex minimisation problem with respect to the motion segmentation function \tilde{u} . To facilitate the minimisation procedure of this overall non-convex problem, the fidelity term f was partly linearised in Eq. (4.5). Nevertheless we should remember that we have to update \vec{w}_0^+ and \vec{w}_0^- regularly. To avoid the risk of getting stuck in a local minimum during the optimisation we therefore apply a coarse-to-fine strategy in the same manner as in our previous work [50]. The final displacement field is then achieved by setting $\vec{w}(\vec{x}) = \vec{w}^+(\vec{x})$ if $\vec{x} \in \Sigma$ and $\vec{w}(\vec{x}) = \vec{w}^-(\vec{x})$ if $\vec{x} \in \Omega \setminus \Sigma$. To calculate the images $T(\vec{x} + \vec{w}^\pm)$ during the iterations and to obtain the final registered image $T(\vec{x} + \vec{w})$ bicubic interpolation is used.

For the experiments we used real MR images of the abdomen, which were taken during the breathing cycle and show the sliding motion of the liver. A qualitative example is shown in Fig. 4.1. The inclusion of the landmarks lead to a more reliable motion segmentation result, since the in fact static part of the background is not assigned to the area with bigger motion anymore. In Fig. 4.2 a quantitative evaluation is shown for 22 different liver image pairs. In average, the A-SIFT method [91] delivered around 1173 matches for these image pairs and after applying RANSAC [31] around 1001 were left. Since we are interested in the discontinuities of the displacement field, we compare the proposed method to the methods that preserve discontinuities in the displacement field, in this case, the demon algorithm with anisotropic diffusion filtering [26], the registration algorithm of Brox *et al.* [16] and our previous work [50]. The parameters for all the methods were chosen by optimising them with respect to the 22 image pairs. For our methods they were set to $\gamma_1 = 4$, $\gamma_2 = 1$, $\mu = 0.2$, $\nu = 0.1$ and for the weighting of the

landmark term we used $\lambda = 0.3$. For the demon algorithm with anisotropic diffusion filtering we could use the suggested parameters and for Brox *et al.*'s method we used $\gamma = 5$, $\alpha = 80$ and $\sigma = 0.9$. Both of our methods showed an improvement compared to the demon algorithm with anisotropic diffusion filtering and the registration algorithm of Brox *et al.*

4.5 Conclusion

In this chapter we presented a primal-dual method for discontinuity preserving non-rigid registration, that makes use of the segmentation framework of Chan *et al.* [21] and includes the information of landmarks. The so gained motion segmentation influences the motion estimation positively by sharpening the discontinuities in the displacement field. The minimisation of the energy functional is implemented in a coarse-to-fine strategy and exploits the rapidity of the primal-dual algorithm studied in [20]. The experimental results demonstrated desirable performance of the proposed method in comparison with those of the demon algorithm with anisotropic diffusion filtering [26] and the registration algorithm of Brox *et al.* [16].

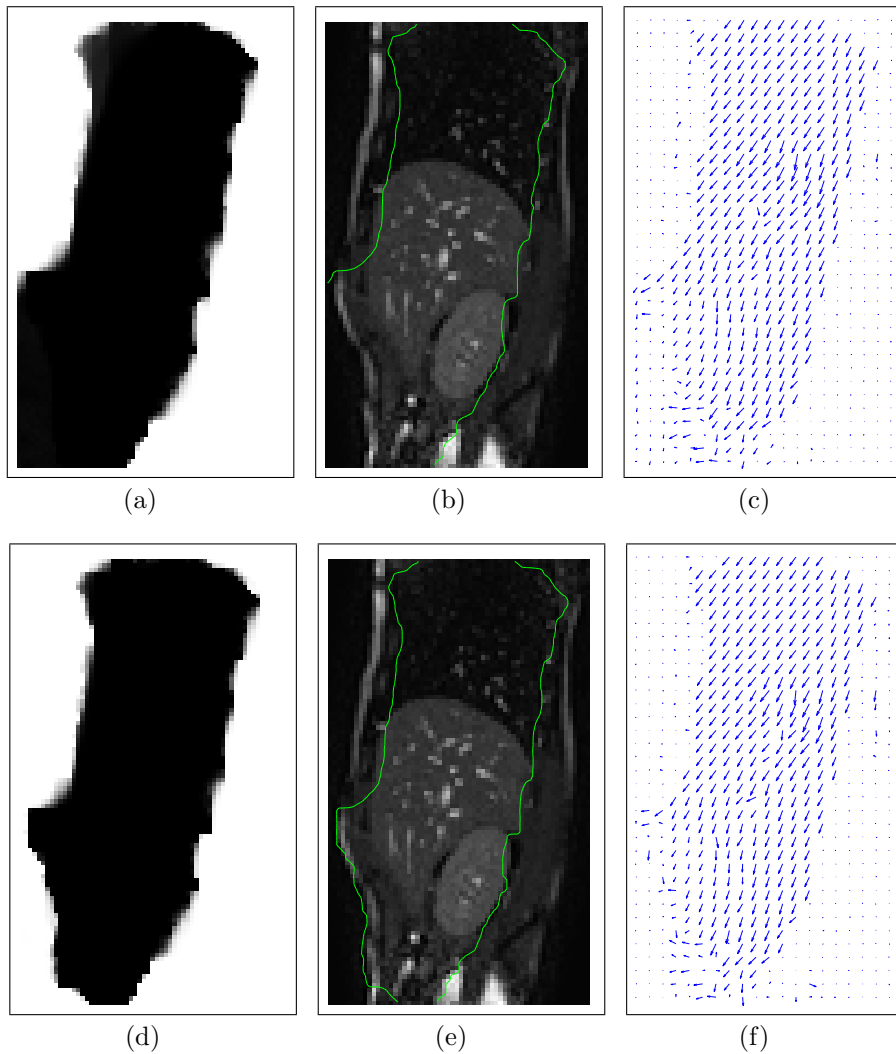


Figure 4.1: Qualitative example for a pair of liver images with a discontinuous displacement field. Motion segmentation \tilde{u} without landmarks (a) and with (d), reference image R overlaid with the motion segmentation without (b) and with landmarks (e) and the displacement field \vec{w} without (c) and with landmarks (f).

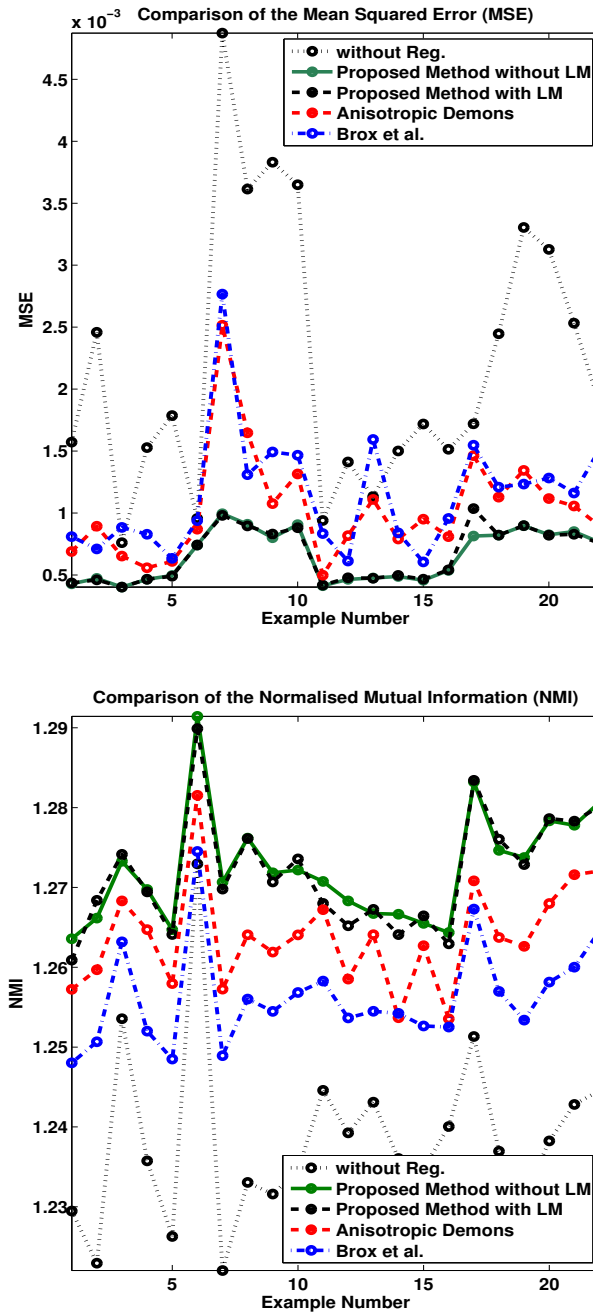


Figure 4.2: Quantitative evaluation for 22 pairs of liver images with a discontinuous displacement field. Comparison of the MSE (*above*) and NMI (*below*).

Chapter 5

Conclusion

In this thesis we proposed three different non-rigid registration methods that are able to preserve discontinuities in the displacement field that appear for example at organ boundaries during the breathing induced sliding organ motion. Our approaches achieved sharp discontinuities in the displacement field by combining motion segmentation with registration in a variational framework. Furthermore, the continuous cuts framework [21] was exploited to guarantee a global minimiser for the motion segmentation function when the displacement field is given. Our overall minimisation problems were however non-convex and we applied a coarse-to-fine strategy to avoid getting stuck in a local minimum during the optimisation procedure. At each level of this coarse-to-fine strategy the minimisation of the energy functional with respect to the motion segmentation function and the displacement field was performed in an alternating scheme by exploiting state-of-the-art methods. Experimental results showed for the MSE and the NMI of the registered images a desirable performance of the proposed methods compared to other discontinuity preserving methods, like the demon algorithm with anisotropic diffusion filtering [26] and the optical flow method of Brox *et al.* [16].

Inspired by the motion segmentation approach of Amiaz and Kiryati [4, 5], our first proposed method in Chapter 2 embedded the optical flow method of Brox *et al.* into the continuous cuts framework of Chan *et al.* [21]. In contrast to the work of Amiaz and Kiryati [4, 5], simple initialisation could be used for the displacement fields and the motion segmentation without the need of any additional methods. To simplify the minimisation of the energy functional an auxiliary variable was introduced similar as in [67, 92]. The minimisation of the energy functional with respect to the motion segmentation function was then performed by making use of the fast algorithm of Chambolle [19], and the one with respect to the displacement field with a fixed point iteration scheme similar as in [16, 4, 5]. For the minimisation of the energy functional

with respect to the auxiliary variable an explicit solution could be derived.

Instead of using an approximation of the L^1 -norm like in Chapter 2, which usually leads to a slow convergence and blurred results [67], in Chapter 3 we used the pure L^1 -norm in the smoothness term and the sum of the absolute values of the constraints in the fidelity term. Furthermore, we partly linearised the fidelity term to facilitate the minimisation procedure. The minimisation of the energy functional was then performed by making use of the fast primal-dual algorithm of Chambolle and Pock [20] for both, the minimisation with respect to the motion segmentation function and the one with respect to the displacement field. For the minimisation of the energy functional with respect to the displacement field we proposed two variants on how to apply the primal-dual algorithm. With this new approach, an improvement in the computational time could be achieved in comparison to the previously proposed method in Chapter 3.

In Chapter 4 we incorporated the information of landmark correspondences into the energy functional that was proposed in Chapter 3 and used the first variant to apply the primal-dual algorithm. Similarly, we could have had also used the second variant to apply the primal-dual algorithm. By providing the prior information of point correspondences to the image registration method, large displacements can be captured and the risk of getting stuck in a local minimum during the optimisation procedure is further dumped [18]. Experimental results showed that with the inclusion of the landmark correspondences more reliable motion segmentation results could be achieved for MR images of breathing induced liver motion.

Although our quantitative evaluation of the proposed methods showed an improvement for the MSE and NMI of the registered images compared to the demon algorithm with anisotropic diffusion filtering and the method of Brox *et al.*, there was no significant difference of the MSE and NMI values among the three proposed methods. It might be that the MSE and NMI are not sufficient measures for a thorough validation and other ways for validation should be considered. For instance, the inclusion of the landmarks as done in Chapter 4 did not lead to a significant improvement of the MSE and NMI compared to the same method without landmarks. An explanation for this occurrence could also be that there were still false matches in the landmark correspondences found by the A-SIFT method [91], that had then a bad influence on the registration method. However, a further careful validation is necessary in future research and in general it would be preferable to use manually selected landmark correspondences by a medical expert. Another interesting point for future research would be a deeper comparison of the two variants of the method proposed in Chapter 3. The comparison of the computational time showed that the second variant performed much faster

than the first variant of the method. It would be, however, interesting to compare the two variants in terms of accuracy by considering here too other validation methods than the comparison of the MSE and NMI. Especially for the clinical use a thorough validation of the registration methods is indispensable and this will be therefore for sure an important point for future research.

There is still a high potential for the improvement of the proposed registration methods. One could for example use multi-label functions for the motion segmentation function in order to capture more complex piecewise smooth displacement fields. Also interesting would be a full convex reformulation of the proposed energy functional, similarly as it was done in the convex relaxation approach of Goldstein *et al.* [39]. Furthermore, to make the proposed approaches capable for multi-modal image registration, for example mutual information could be considered as a similarity measure and embedded into the variational framework by making use of the works [44, 69].

In summary, we proposed in this thesis three non-rigid registration methods that are able to preserve discontinuities in the displacement field and we achieved satisfying results for synthetic images and real MR images of breathing induced liver motion.

Bibliography

- [1] L. Ambrosio, N. Fusco, and D. Pallara. *Functions of Bounded Variation and Free Discontinuity Problems*. Oxford Mathematical Monographs. The Clarendon Press, Oxford University Press, New York, 2000.
- [2] L. Ambrosio and V. M. Tortorelli. Approximation of Functionals Depending on Jumps by Elliptic Functionals via Γ -Convergence. *Communications on Pure and Applied Mathematics*, 43(8):999–1036, 1990.
- [3] L. Ambrosio and V. M. Tortorelli. On the Approximation of Free Discontinuity Problems. *Unione Matematica Italiana. Bollettino. B. Serie VII*, 6(1):105–123, 1992.
- [4] T. Amiaz and N. Kiryati. Dense Discontinuous Optical Flow Via Contour-Based Segmentation. In *IEEE International Conference on Image Processing, 2005. ICIP 2005.*, volume 3, pages III – 1264–1267, 2005.
- [5] T. Amiaz and N. Kiryati. Piecewise-Smooth Dense Optical Flow via Level Sets. *International Journal of Computer Vision*, 68(2):111–124, 2006.
- [6] P. Arnold, F. Preiswerk, B. Fasel, R. Salomir, K. Scheffler, and Ph. C. Cattin. 3D Organ Motion Prediction for MR-Guided High Intensity Focused Ultrasound. In *Medical Image Computing and Computer-Assisted Intervention - MICCAI 2011*, volume 6892 of *LNCS*, pages 623–630. Springer-Verlag, 2011.
- [7] J. Ashburner. A Fast Diffeomorphic Image Registration Algorithm. *NeuroImage*, 38(1):95–113, 2007.
- [8] G. Aubert, R. Deriche, and P. Kornprobst. Computing Optical Flow via Variational Techniques. *SIAM Journal on Applied Mathematics*, 60(1):156–182, 1999.

- [9] J. L. Barron, D. J. Fleet, and S. S. Beauchemin. Performance of Optical Flow Techniques. *International Journal of Computer Vision*, 12(1):43–77, 1994.
- [10] S. S. Beauchemin and J. L. Barron. The Computation of Optical Flow. *ACM Computing Surveys*, 27(3):433–467, 1995.
- [11] M. J. Black and P. Anandan. The Robust Estimation of Multiple Motions: Parametric and Piecewise-Smooth Flow Fields. *Computer Vision and Image Understanding*, 63(1):75–104, 1996.
- [12] Y. Boykov, O. Veksler, and R. Zabih. Fast Approximate Energy Minimization via Graph Cuts. *IEEE Transactions on Pattern Analysis and Machine Intelligence*, 23(11):1222–1239, 2001.
- [13] X. Bresson, S. Esedoğlu, P. Vandergheynst, J.-P. Thiran, and S. Osher. Fast Global Minimization of the Active Contour/Snake Model. *Journal of Mathematical Imaging and Vision*, 28(2):151–167, 2007.
- [14] E. S. Brown, T. F. Chan, and X. Bresson. Completely Convex Formulation of the Chan-Vese Image Segmentation Model. *International Journal of Computer Vision*, 98(1):103–121, 2012.
- [15] L. G. Brown. A Survey of Image Registration Techniques. *ACM Computing Surveys*, 24(4):325–376, 1992.
- [16] T. Brox, A. Bruhn, N. Papenbergh, and J. Weickert. High Accuracy Optical Flow Estimation Based on a Theory for Warping. In *Computer Vision - ECCV 2004. Proceedings, Part IV.*, volume 3024 of *LNCS*, pages 25–36. Springer-Verlag, 2004.
- [17] T. Brox, A. Bruhn, and J. Weickert. Variational Motion Segmentation with Level Sets. In *Computer Vision - ECCV 2006. Proceedings, Part I.*, volume 3951 of *LNCS*, pages 471–483. Springer-Verlag, 2006.
- [18] T. Brox and J. Malik. Large Displacement Optical Flow: Descriptor Matching in Variational Motion Estimation. *IEEE Transactions on Pattern Analysis and Machine Intelligence*, 33(3):500–513, 2011.
- [19] A. Chambolle. An Algorithm for Total Variation Minimization and Applications. *Journal of Mathematical Imaging And Vision*, 20(1-2):89–97, 2004.

- [20] A. Chambolle and T. Pock. A First-Order Primal-Dual Algorithm for Convex Problems with Applications to Imaging. *Journal of Mathematical Imaging and Vision*, 40(1):120–145, 2011.
- [21] T. F. Chan, S. Esedoğlu, and M. Nikolova. Algorithms for Finding Global Minimizers of Image Segmentation and Denoising Models. *SIAM Journal on Applied Mathematics*, 66(5):1632–1648, 2006.
- [22] T. F. Chan and L. A. Vese. Active Contours Without Edges. *IEEE Transactions on Image Processing*, 10(2):266–277, 2001.
- [23] D. Cremers and C. Schnörr. Motion Competition: Variational Integration of Motion Segmentation and Shape Regularization. In *Pattern Recognition. 24th DAGM Symposium.*, volume 2449 of *LNCS*, pages 472–480. Springer-Verlag, 2002.
- [24] D. Cremers and S. Soatto. Motion Competition: A Variational Approach to Piecewise Parametric Motion Segmentation. *International Journal of Computer Vision*, 62(3):249–265, 2005.
- [25] W. R. Crum, T. Hartkens, and D. L. G. Hill. Non-rigid image registration: theory and practice. *The British Journal of Radiology*, 77(Sp. Iss. 2):S140–S153, 2004.
- [26] D. Demirovic, A. Serifovic, and Ph. C. Cattin. An Anisotropic Diffusion Regularized Demons for Improved Registration of Sliding Organs. In *18th International Electrotechnical and Computer Science Conference (ERK)*, 2009.
- [27] E. Esser, X. Zhang, and T. F. Chan. A General Framework for a Class of First Order Primal-Dual Algorithms for Convex Optimization in Imaging Science. *SIAM Journal on Imaging Sciences*, 3(4):1015–1046, 2010.
- [28] L. C. Evans and R. F. Gariepy. *Measure Theory and Fine Properties of Functions*. Studies in Advanced Mathematics. CRC Press, Boca Raton, FL, 1992.
- [29] H. Federer. Curvature Measures. *Transactions of the American Mathematical Society*, 93(3):418–491, 1959.
- [30] H. Federer. *Geometric Measure Theory*. Die Grundlehren der mathematischen Wissenschaften, Band 153. Springer-Verlag, New York, 1969.

- [31] M. A. Fischler and R. C. Bolles. Random Sample Consensus: A Paradigm for Model Fitting with Applications to Image Analysis and Automated Cartography. *Communications of the Association for Computing Machinery*, 24(6):381–395, 1981.
- [32] J. M. Fitzpatrick and J. B. West. The Distribution of Target Registration Error in Rigid-Body Point-Based Registration. *IEEE Transactions on Medical Imaging*, 20(9):917–927, 2001.
- [33] J. M. Fitzpatrick, J. B. West, and C. R. Maurer Jr. Predicting Error in Rigid-Body Point-Based Registration. *IEEE Transactions on Medical Imaging*, 17(5):694–702, 1998.
- [34] D. J. Fleet and Y. Weiss. Optical Flow Estimation. In *Handbook of Mathematical Models in Computer Vision*, pages 237–257. Springer-Verlag, New York, 2006.
- [35] W. H. Fleming and R. Rishel. An Integral Formula for Total Gradient Variation. *Archiv der Mathematik*, 11(1):218–222, 1960.
- [36] P. A. Freeborough, R. P. Woods, and N. C. Fox. Accurate Registration of Serial 3D MR Brain Images and Its Application to Visualizing Change in Neurodegenerative Disorders. *Journal of Computer Assisted Tomography*, 20(6):1012–1022, 1996.
- [37] K. Fundana, A. Heyden, C. Gosch, and C. Schnörr. Continuous Graph Cuts for Prior-Based Object Segmentation. In *19th International Conference on Pattern Recognition, 2008. ICPR 2008.*, pages 1–4. IEEE, 2008.
- [38] E. Giusti. *Minimal Surfaces and Functions of Bounded Variation*, volume 80 of *Monographs in Mathematics*. Birkhäuser Verlag, Basel, 1984.
- [39] T. Goldstein, X. Bresson, and S Osher. Global Minimization of Markov Random Fields with Applications to Optical Flow. Technical report, UCLA, 2009.
- [40] T. Goldstein and S. Osher. The Split Bregman Method for L1-Regularized Problems. *SIAM Journal on Imaging Sciences*, 2(2):323–343, 2009.
- [41] H. Grabner, J. Matas, L. Van Gool, and Ph. Cattin. Tracking the Invisible: Learning Where the Object Might be. In *2010 IEEE Conference on Computer Vision and Pattern Recognition (CVPR)*, pages 1285–1292, 2010.

- [42] E. Haber, S. Heldmann, and J. Modersitzki. A Scale-Space Approach to Landmark Constrained Image Registration. In *Scale Space and Variational Methods in Computer Vision*, volume 5567 of *LNCS*, pages 612–623. Springer-Verlag, 2009.
- [43] F. Heitz and P. Bouthemy. Multimodal Estimation of Discontinuous Optical Flow Using Markov Random Fields. *IEEE Transactions on Pattern Analysis and Machine Intelligence*, 15(12):1217–1232, 1993.
- [44] G. Hermosillo, C. Ched'hotel, and O. Faugeras. Variational Methods for Multimodal Image Matching. *International Journal of Computer Vision*, 50(3):329–343, 2002.
- [45] D. L. G. Hill, P. G. Batchelor, M. Holden, and D. J. Hawkes. Medical image registration. *Physics in Medicine and Biology*, 46(3):R1–R45, 2001.
- [46] M. Holden, D. L. G. Hill, E. R. E. Denton, J. M. Jarosz, T. C. S. Cox, T. Rohlfing, J. Goodey, and D. J. Hawkes. Voxel Similarity Measures for 3-D Serial MR Brain Image Registration. *IEEE Transactions on Medical Imaging*, 19(2):94–102, 2000.
- [47] B. K. P. Horn and B. G. Schunck. Determining Optical Flow. *Artificial Intelligence*, 17(1-3):185–203, 1981.
- [48] H. J. Johnson and G. E. Christensen. Consistent Landmark and Intensity-Based Image Registration. *IEEE Transactions on Medical Imaging*, 21(5):450–461, 2002.
- [49] S. Kiriyanthan, K. Fundana, and Ph. C. Cattin. Discontinuity Preserving Registration of Abdominal MR Images with Apparent Sliding Organ Motion. In *Abdominal Imaging. Computational and Clinical Applications.*, volume 7029 of *LNCS*, pages 231–139. Springer-Verlag, 2012.
- [50] S. Kiriyanthan, K. Fundana, T. Majeed, and Ph. C. Cattin. Discontinuity Preserving Registration through Motion Segmentation: A Primal-Dual Approach. submitted.
- [51] S. Kiriyanthan, K. Fundana, T. Majeed, and Ph. C. Cattin. A Landmark-Based Primal-Dual Approach for Discontinuity Preserving Registration. In *Abdominal Imaging. Computational and Clinical Applications.*, volume 7601 of *LNCS*, pages 137–146. Springer-Verlag, 2012.

- [52] S. Kiriyanthan, K. Fundana, T. Majeed, and Ph. C. Cattin. A Primal-Dual Approach for Discontinuity Preserving Registration. In *2012 9th IEEE International Symposium on Biomedical Imaging (ISBI)*, pages 350–353, 2012.
- [53] J. Kybic and M. Unser. Fast Parametric Elastic Image Registration. *IEEE Transactions on Image Processing*, 12(11):1427–1442, 2003.
- [54] J. Lellmann, J. Kappes, J. Yuan, F. Becker, and C. Schnörr. Convex Multi-class Image Labeling by Simplex-Constrained Total Variation. In *Scale Space and Variational Methods in Computer Vision*, volume 5567 of *LNCS*, pages 150–162. Springer-Verlag, 2009.
- [55] E. H. Lieb and M. Loss. *Analysis*, volume 14 of *Graduate Studies in Mathematics*. American Mathematical Society, Providence, RI, second edition, 2001.
- [56] D. G. Lowe. Distinctive Image Features from Scale-Invariant Keypoints. *International Journal of Computer Vision*, 60(2):91–110, 2004.
- [57] B. D. Lucas and T. Kanade. An Iterative Image Registration Technique with an Application to Stereo Vision. In *Proceedings of the 7th International Joint Conference on Artificial intelligence*, pages 674–679, 1981.
- [58] E. Mémin and P. Pérez. Hierarchical Estimation and Segmentation of Dense Motion Fields. *International Journal of Computer Vision*, 46(2):129–155, 2002.
- [59] J. Modersitzki. *Numerical Methods for Image Registration*. Numerical Mathematics and Scientific Computation. Oxford University Press, New York, 2004. Oxford Science Publications.
- [60] D. Mumford and J. Shah. Optimal Approximations by Piecewise Smooth Functions and Associated Variational Problems. *Communications on Pure and Applied Mathematics*, 42(5):577–685, 1989.
- [61] H.-H. Nagel and W. Enkelmann. An Investigation of Smoothness Constraints for the Estimation of Displacement Vector Fields from Image Sequences. *IEEE Transactions on Pattern Analysis and Machine Intelligence*, 8(5):565–593, 1986.
- [62] P. Nesi. Variational Approach to Optical Flow Estimation Managing Discontinuities. *Image and Vision Computing*, 11(7):419–439, 1993.

- [63] S. Osher and R. Fedkiw. *Level Set Methods and Dynamic Implicit Surfaces*, volume 153 of *Applied Mathematical Sciences*. Springer-Verlag, New York, 2003.
- [64] S. Osher and J. A. Sethian. Fronts Propagating with Curvature-Dependent Speed: Algorithms Based on Hamilton-Jacobi Formulations. *Journal of Computational Physics*, 79(1):12–49, 1988.
- [65] D. Paquin, D. Levy, and L. Xing. Hybrid Multiscale Landmark and Deformable Image Registration. *Mathematical Biosciences and Engineering*, 4(4):711–737, 2007.
- [66] T. Pock, D. Cremers, H. Bischof, and A. Chambolle. An Algorithm for Minimizing the Mumford-Shah Functional. In *2009 IEEE 12th International Conference on Computer Vision*, pages 1133–1140, 2009.
- [67] T. Pock, M. Urschler, C. Zach, R. Beichel, and H. Bischof. A Duality Based Algorithm for TV- L^1 -Optical-Flow Image Registration. In *Medical Image Computing and Computer-Assisted Intervention - MICCAI 2007*, volume 4792 of *LNCS*, pages 511–518. Springer-Verlag, 2007.
- [68] F. Preiswerk, P. Arnold, B. Fasel, and Ph. C. Cattin. A Bayesian Framework for Estimating Respiratory Liver Motion from Sparse Measurements. In *Abdominal Imaging. Computational and Clinical Applications.*, volume 7029 of *LNCS*, pages 207–214. Springer-Verlag, 2012.
- [69] P. Rogelj, S. Kovačič, and J. C. Gee. Point Similarity Measures for Non-Rigid Registration of Multi-Modal Data. *Computer Vision and Image Understanding*, 92(1):112–140, 2003.
- [70] D. Ruan, S. Esedoğlu, and J. A. Fessler. Discriminative Sliding Preserving Regularization in Medical Image Registration. In *IEEE International Symposium on Biomedical Imaging: From Nano to Macro, 2009. ISBI '09.*, pages 430–433, 2009.
- [71] L. I. Rudin, S. Osher, and E. Fatemi. Nonlinear Total Variation Based Noise Removal Algorithms. *Physica D*, 60(1-4):259–268, 1992.
- [72] D. Rueckert, L. I. Sonoda, C. Hayes, D. L. G. Hill, M. O. Leach, and D. J. Hawkes. Nonrigid Registration Using Free-Form Deformations: Application to Breast MR Images. *IEEE Transactions on Medical Imaging*, 18(8):712–721, 1999.

- [73] A. Schmidt-Richberg, J. Ehrhardt, R. Werner, and H. Handels. Slipping Objects in Image Registration: Improved Motion Field Estimation with Direction-Dependent Regularization. In *Medical Image Computing and Computer-Assisted Intervention - MICCAI 2009*, volume 5761 of *LNCS*, pages 755–762. Springer-Verlag, 2009.
- [74] J. A. Schnabel, C. Tanner, A. D. Castellano-Smith, A. Degenhard, M. O. Leach, D. R. Hose, D. L. G. Hill, and D. J. Hawkes. Validation of Non-rigid Image Registration Using Finite-Element Methods: Application to Breast MR Images. *IEEE Transactions on Medical Imaging*, 22(2):238–247, 2003.
- [75] B. G. Schunck. Image Flow Segmentation and Estimation by Constraint Line Clustering. *IEEE Transactions on Pattern Analysis and Machine Intelligence*, 11(10):1010–1027, 1989.
- [76] J. A. Sethian. *Level Set Methods and Fast Marching Methods. Evolving Interfaces in Computational Geometry, Fluid Mechanics, Computer Vision, and Materials Science.*, volume 3 of *Cambridge Monographs on Applied and Computational Mathematics*. Cambridge University Press, Cambridge, second edition, 1999.
- [77] S. Setzer. Operator Splittings, Bregman Methods and Frame Shrinkage in Image Processing. *International Journal of Computer Vision*, 92(3):265–280, 2011.
- [78] G. Strang. L^1 and L^∞ Approximation of Vector Fields in the Plane. In *Nonlinear Partial Differential Equations in Applied Science (Tokyo, 1982)*, volume 81 of *North-Holland Mathematics Studies*, pages 273–288. North-Holland, Amsterdam, 1983.
- [79] G. Strang. Maximal Flow Through a Domain. *Mathematical Programming*, 26(2):123–143, 1983.
- [80] E. Strelakowskiy, B. Goldluecke, and D. Cremers. Tight Convex Relaxations for Vector-Valued Labeling Problems. In *2011 IEEE International Conference on Computer Vision (ICCV)*, pages 2328–2335, 2011.
- [81] C. Studholme, D. L. G. Hill, and D. J. Hawkes. Automated Three-Dimensional Registration of Magnetic Resonance and Positron Emission Tomography Brain Images by Multiresolution Optimization of Voxel Similarity Measures. *Medical Physics*, 24(1):25–35, 1997.

- [82] J.P. Thirion. Image Matching as a Diffusion Process: an Analogy with Maxwell’s Demons. *Medical Image Analysis*, 2(3):243–260, 1998.
- [83] T. Vercauteren, X. Pennec, A. Perchant, and N. Ayache. Diffeomorphic Demons: Efficient Non-Parametric Image Registration. *NeuroImage*, 45(1, 1):S61–S72, 2009.
- [84] L. A. Vese and T. F. Chan. A Multiphase Level Set Framework for Image Segmentation Using the Mumford and Shah Model. *International Journal of Computer Vision*, 50(3):271–293, 2002.
- [85] M. von Siebenthal, G. Székely, U. Gamper, P. Boesiger, A. Lomax, and Ph. Cattin. 4D MR Imaging of Respiratory Organ Motion and its Variability. *Physics in Medicine and Biology*, 52(6):1547–1564, 2007.
- [86] H. Wang, L. Dong, J. O’Daniel, R. Mohan, A. S. Garden, K. K. Ang, D. A. Kuban, M. Bonnen, J. Y. Chang, and R. Cheung. Validation of an Accelerated ‘Demons’ Algorithm for Deformable Image Registration in Radiation Therapy. *Physics in Medicine and Biology*, 50(12):2887–2905, 2005.
- [87] J. Weickert, A. Bruhn, T. Brox, and N. Papenberg. A Survey on Variational Optic Flow Methods for Small Displacements. In *Mathematical Models for Registration and Applications to Medical Imaging*, volume 10 of *Mathematics in Industry*, pages 103–136. Springer-Verlag, Berlin, 2006.
- [88] J. Weickert and C. Schnörr. Variational Optic Flow Computation with a Spatio-Temporal Smoothness Constraint. *Journal of Mathematical Imaging and Vision*, 14(3):245–255, 2001.
- [89] J. West, J. M. Fitzpatrick, M. Y. Wang, B. M. Dawant, C. R. Maurer Jr., R. M. Kessler, R. J. Maciunas, C. Barillot, D. Lemoine, A. Collignon, F. Maes, P. Suetens, D. Vandermeulen, P. A. van den Elsen, S. Napel, T. S. Sumanaweera, B. Harkness, P. F. Hemler, D. L. G. Hill, D. J. Hawkes, C. Studholme, J. B. A. Maintz, M. A. Viergever, G. Malandain, X. Pennec, M. E. Noz, G. Q. Maguire Jr., M. Pollack, C. A. Pelizzari, R. A. Robb, D. Hanson, and R. P. Woods. Comparison and Evaluation of Retrospective Intermodality Brain Image Registration Techniques. *Journal of Computer Assisted Tomography*, 21(4):554–566, 1997.
- [90] R. P. Woods, S. T. Grafton, C. J. Holmes, S. R. Cherry, and J. C. Mazziotta. Automated Image Registration: I. General Methods and

Intrasubject, Intramodality Validation. *Journal of Computer Assisted Tomography*, 22(1):139–152, 1998.

- [91] G. Yu and J.-M. Morel. ASIFT: An Algorithm for Fully Affine Invariant Comparison. *Image Processing On Line*, 2011. DOI: <http://dx.doi.org/10.5201/ipol.2011.my-asift>.
- [92] C. Zach, T. Pock, and H. Bischof. A Duality Based Approach for Realtime TV- L^1 Optical Flow. In *Pattern Recognition*, volume 4713 of *LNCS*, pages 214–223. Springer-Verlag, 2007.
- [93] W. P. Ziemer. *Weakly Differentiable Functions. Sobolev Spaces and Functions of Bounded Variation.*, volume 120 of *Graduate Texts in Mathematics*. Springer-Verlag, New York, 1989.
- [94] B. Zitova and J. Flusser. Image registration methods: a survey. *Elsevier, Image and Vision Computing*, 21(11):977–1000, 2003.

Curriculum Vitae

Personal Information

Name: Silja Kiriyanthan
Date of Birth: 03.10.1984
Place of Birth: Basel-Stadt, Switzerland
Nationality: Swiss

Academic Education

2003 - 2006 Bachelor of Science in Mathematics, University of Basel
2006 - 2008 Master of Science in Mathematics, University of Basel
2008 - 2012 Doctoral Studies, University of Basel

Work Experience

2008 - 2009 Teaching Assistant at the Mathematical Institute,
University of Basel
2008 - 2012 Research Assistant at the Medical Image Analysis Center,
University of Basel

My academic teachers were Prof. A. Abdulle, Prof. N. A'Campo, Prof. S. Arber, Prof. Y.-A. Barde, Prof. B. Binggeli, Dr. V. Bosser, Prof. R. Buser, Prof. Ph. C. Cattin, Prof. A. Dedner, Prof. M. J. Grote, Dr. M. Halic, Prof. M. N. Hall, Prof. H.-P. Hauri, Prof. H.-C. Im Hof, Prof. C. Körner, Prof. H. Kraft, Dr. C. Luchsinger, Prof. A. Lüthi, Prof. D. Masser, Prof. J. Mayer, Prof. C. Rehmman-Sutter, Prof. W. Reichel, Prof. H. Reichert, Prof. V. Roth, Prof. M. Rüegg, Prof. K. Scheffler, Dr. H. Schneider, Prof. B. Schweizer, Prof. D. G. Senn, Prof. M. Tanner, Prof. F.-K. Thielemann, Dr. C. Trefzger, Prof. T. Vetter, Prof. K. Vogt, Dr. P. Weidemaier, Prof. N. Weiss.